Synthesis and Characterisation of Antiperovskite Ionic Conductor Materials for Lithium-ion and Sodium-ion Solid-state Electrolytes



Brigita D. Darminto

The Queen's College

University of Oxford

A thesis presented for the degree of

Doctor of Philosophy

Trinity 2023

Acknowledgements

First and foremost, I would like to thank my supervisor Prof. Mauro Pasta. I am very grateful for his guidance throughout my time as a DPhil student and for the unparalleled lab resources and equipment he provided, without which none of this work would have been possible.

I would like to acknowledge those with whom I have collaborated in performing some of the work reported here:

1. Prof. Hyeon Jeong Lee, for taking me under her wing from the very start of my DPhil and providing helpful advice on how to keep on going despite countless failures in synthesising pure antiperovskites. Prof. Lee also contributed to the experimental work reported in Chapter 5. She synthesised the $Li_2OHCl0.9Br0.1$ sample.

2. Dr. Gregory Rees and Dr. Kenjiro Hashi, who collected NMR data reported in Chapters 3, 4, and 5.

3. Ben Jagger for collecting the XPS data reported in Chapter 2.

4. Emily Milan and Yvonne Chart for collecting the PFIB data in Chapters 3 and 4.

5. Dr. Maria Diaz-Lopez and John Cattermull who used their discretionary beam time to collect the synchrotron XRD data reported in Chapters 4 and 5.

6. Prof. Andrew Goodwin and Dr. Camilla Di Mino for advising me on how to process the synchrotron XRD data.

7. Thomas Orton and Dr. Stephen Turrell, who patiently read my drafts and gave

valuable comments and suggestions.

I am also grateful to my assessors, Prof. Jonathan Yates and Prof. Richard Todd, for their helpful feedback on my early results and progress, and to all members of the Pasta Group for their constant mental and practical support.

My DPhil was fully supported by the Indonesia Endowment for Education (LPDP). I have also benefited from conference travel funding provided by the Electrochemical Society and the Materials Department.

Finally, I would like to thank my family (Ayah, Ibu, Raras, Gagas, and Ninis) and my partner (Tom) for all the years of love, laughter, and prayers. Without every single one of you, this thesis would never have been finished.

Abstract

As the world is racing towards net zero, the demand for rechargeable batteries with higher energy density and improved safety increases and becomes more urgent. Solid-state batteries (SSBs) with metal anodes are believed to be the way forward. Lithium-based SSBs may lead due to lessons learned from widely adopted lithium-ion batteries (LIBs), but Na-based SSBs will follow by offering cheaper and more abundant alternatives. In both cases, solid electrolytes (SEs) are one of the key enablers for reaching SSB potentials.

Having been identified as a promising SE candidate, antiperovskites have attracted increasing research interest in the past decade. Despite this, research on antiperovskites is still in an early stage compared to other SEs, such as NASICON/ LISICON, and many questions remain to be explored experimentally. This includes their electronic conductivity, stability against metal anodes and the origins of their non-Arrhenius ionic conductivity behaviour. In this thesis, three compositions of Na-rich antiperovskite (NaRAP) were synthesised and their properties were investigated. In addition, model NaRAP and Li-rich antiperovskite (LiRAP) were investigated to elucidate the origins of their non-Arrhenius ionic conductivity behaviour at elevated temperatures.

Firstly, Na_3OBr, Na_3OCl, and Na_3OBH_4 were synthesised using two different Na_2O precursors, commercial and 'homemade'. Commercially available Na_2O contains approximately 20% Na_2O_2 impurity while 'homemade' Na_2O is highly pure. Syntheses with both precursors are common in the literature and have been reported to lead to successful NaRAP formation. However, it is not clear whether the difference in precursor quality will affect the final properties of the products. Using a combination of X-ray diffraction

(XRD) and nuclear magnetic resonance (NMR), it became clear that starting with a purer precursor will not only reduce the amount of crystalline impurities but also poorly crystalline ones, which are often overlooked by the research community in the past. With in-situ X-ray photoelectron spectroscopy (XPS), we provide evidence that NaRAPs are stable against Na metal. Additionally, chronoamperometry reveals that their electronic conductivities are lower than those reported for NASICON. Overall, these findings provide experimental evidence to make more informed decisions on whether NaRAPs are suitable solid electrolytes (SEs) for solid-state metal batteries (SSMBs).

Secondly, non-Arrhenius ionic conductivity behaviour has been reported in antiperovskites, including Na_3OBr. Some argued that this could be due to structural instability, which includes phase transitions, order-disorder transitions of the ion sublattice and crystal melting. However, no clear experimental evidence of structural changes has been provided. With a combination of bulk and local characterisation techniques, we excluded crystallographic disorder on the anion sites as the cause of the change in activation energy. We then identified the presence of poorly crystalline impurities, not detectable by XRD, and elucidated their effect on ionic conductivity. These findings improve understanding of the processing-structure-properties relationships pertaining to NaRAPs and highlight the need to re-visit the non-Arrhenius ionic conductivity behaviour seen in a range of other solid electrolyte materials, particularly the LiRAPs, where the behaviour has been reported across different compositions.

Finally, with the techniques developed to uncover the origin of the non-Arrhenius behaviour in Na_3OBr, this thesis investigates the origin of the similar behaviour in $Li_2OHCl_{0.9}Br_{0.1}$. The results show that despite the initial similarities, the origins of this behaviour are dif-

ferent in these two compositions. Non-linear changes in the lattice parameter and thermal parameter of the halide ions are apparent in the $Li_2OHCl_{0.9}Br_{0.1}$, suggesting that the transition involves bulk crystallographical changes.

Some of the results presented in this work are shown in the following publications:

1. Hyeon Jeong Lee, Brigita Darminto, Sudarshan Narayanan, Maria Diaz-Lopez, Albert W. Xiao, Yvonne Chart, Ji Hoon Lee, James A. Dawson, and Mauro Pasta. Li-ion conductivity in $Li_2OHCl_{1-x}Br_x$ solid electrolytes: grains, grain boundaries and interfaces. Journal of Materials Chemistry A, 10(21):11574–11586, 4 2022. ISSN 20507496. doi: 10.1039/d2ta01462a.

2. Brigita Darminto, Gregory J. Rees, John Cattermull, Kenjiro Hashi, Maria Diaz-Lopez, Naoaki Kuwata, Stephen J. Turrell, Emily Milan, Yvonne Chart, Camilla di Mino, Hyeon Jeong Lee, Andrew L. Goodwin, and Mauro Pasta. On the Origin of Non-Arrhenius Na-ion Conductivity in Na_3OBr. Angewandte Chemie International Edition, 62(51): e20231444, 12 2023. ISSN 14337851. doi: 10.1002/anie.202314444.

3. Brigita Darminto, Gregory J. Rees, Ben Jagger, Emily Milan, Hua Guo, Hyeon Jeong Lee, and Mauro Pasta. Synthesis and Comprehensive Characterisation of Sodium Antiperovskites. *In preparation*.

Declaration

I declare that the work presented in this thesis, unless otherwise stated, is the result of my original work and is written entirely by myself.

List of Abbreviations

Abbreviation	Meaning
AC	Alternating Current
AIMD	Ab-initio Molecular Dynamics
ASSB	All Solid-state Battery
CP	Cold Press
CPE	Constant Phase Element
CSA	Chemical Shift Anisotropy
CSE	Composite Solid Electrolyte
DC	Direct Current
DFT	Density Functional Theory
DSC	Differential Scanning Calorimetry
EDS	Energy Dispersive X-ray Spectroscopy
EIS	Electrochemical Impedance Spectroscopy
FIB	Focused Ion Beam
FTIR	Fourier Transform Infrared
GHG	Greenhouse Gas
GOF	Goodness of Fit
HP	Hot Press
ISE	Inorganic Solid Electrolyte
LIB	Lithium-ion Battery
LMB	Lithium Metal Battery

LiRAP	Lithium Rich Antiperovskite
LISICON	Lithium Superionic Conductor
MAS	Magic Angle Spinning
NaRAP	Sodium Rich Antiperovskite
NASICON	Sodium Superionic Conductor
NMR	Nuclear Magnetic Resonance
NQR	Nuclear Quadrupole Resonance
PAN	Polyacrylonitrile
PDF	Pair Distribution Function
PEEK	Polyether Ether Ketone
PEIS	Potentiostatic Electrochemical Spectroscopy
PEO	Polyethylene Oxide
PFIB	Plasma Focused Ion Beam
PLD	Pulsed Laser Deposition
PMMA	Polymethyl Methacrylate
PSE	Polymer Solid Electrolyte
PVDF	Polyvinylidene Fluoride
RF	Radio Frequency
RMC	Reverse Monte Carlo
RT	Room Temperature
SE	Solid Electrolyte
SEI	Solid Electrolyte Interphase
SEM	Scanning Electron Microscopy

SHE	Standard Hydrogen Electrode
SPS	Spark Plasma Sintering
SSB	Solid-state Battery
SSMB	Solid-state Metal Battery
XPS	X-ray Photoelectron Spectroscopy
XRD	X-ray Diffraction

Table of Contents

1 Introduction **1**

1.1 The Need for Batteries 1

1.2 Metallic Anodes 3

1.3 Solid Electrolytes 5

1.3.1 Inorganic Solid-state Electrolytes (ISEs) 7

1.3.2 Polymer Solid Electrolytes (PSEs) 9

1.3.3 Composite Solid Electrolytes (CSEs) 9

1.3.4 The Solid Electrolyte Challenge 10

1.4 Antiperovskites 11

1.4.1 Fundamentals and History 12

1.4.2 The Surge of Interest 16

1.4.3 Ionic Transport and Doping Strategies 17

1.4.4 Quest for Understanding: Antiperovskite Behaviours 22

1.5 Thesis Objectives 26

1.6 Bibliography 28

2 Experimental Techniques **52**

2.1 Synthetic Techniques 52

2.1.1 Solid-state Synthesis 52

2.1.2 Calendering 52

2.1.3 Ball-milling Synthesis 53

2.1.4 Liquid State Synthesis 54
2.2 Structural Characterisation 54
2.2.1 Powder X-ray Diffraction 54
2.2.2 Rietveld Refinement 58
2.2.3 Differential Scanning Calorimetry 59
2.2.4 Scanning Electron Microscopy and Focused Ion Beam Milling . . 60
2.2.5 Density Measurement 62
2.3 Chemical Characterisation 63
2.3.1 X-ray Photoelectron Spectroscopy 63
2.3.2 Solid-state Nuclear Magnetic Resonance Spectroscopy 65
2.4 Electrochemical Characterisation 69
2.4.1 Solid Electrolyte Pellet Preparation 69
2.4.2 Solid-state Cell Assembly 71
2.4.3 Electrochemical Impedance Spectroscopy 72
2.4.4 Chronoamperometry 77
2.5 Bibliography 78

3 Synthesis and Characterisation of Na_3OB (B = Cl, Br, or BH_4) 87

3.1 Introduction 87
3.2 Experimental 88
3.2.1 Na_3OB (B = Cl, Br, or BH_4) Synthesis 88
3.2.2 Pellet Processing 90
3.2.3 Differential Scanning Calorimetry (DSC) 90
3.2.4 Electrochemical Impedance Spectroscopy (EIS) 90

3.2.5 Chronoamperometry 91
3.2.6 Ex-situ Scanning Electron Microscopy (SEM) 91
3.2.7 X-ray Diffraction (XRD) 91
3.2.8 Nuclear Magnetic Resonance (NMR) Spectroscopy 92
3.2.9 In-situ X-ray Photon Spectroscopy (XPS) 92
3.3 Results and discussion 93
3.4 Conclusion 107
3.5 Bibliography 108

4 On the Origin of Non-Arrhenius Ionic Conductivity in Na_3OBr 115

4.1 Introduction 115
4.2 Experimental 116
4.2.1 Synthesis of Na_3OBr 116
4.2.2 Differential Scanning Calorimetry (DSC) 117
4.2.3 Electrochemical Impedance Spectroscopy (EIS) 117
4.2.4 Ex-situ Scanning Electron Microscopy (SEM) 118
4.2.5 X-ray Diffraction (XRD) 118
4.2.6 Nuclear Magnetic Resonance (NMR) Spectroscopy 119
4.3 Results and Discussion 120
4.4 Conclusion 134
4.5 Bibliography 135

5 On the Origin of Non-Arrhenius Ionic Conductivity in $Li_2OHCl_{0.9}Br_{0.1}$ 142

5.1 Introduction 142
5.2 Experimental Methods 143

5.2.1 Synthesis of $Li_2OHCl_{0.9}Br_{0.1}$ 143
5.2.2 Differential Scanning Calorimetry (DSC) 143
5.2.3 Electrochemical Impedance Spectroscopy (EIS) 144
5.2.4 X-ray Diffraction (XRD) 144
5.2.5 Nuclear Magnetic Resonance (NMR) Spectroscopy 145
5.3 Results and Discussion 146
5.4 Conclusion 156
5.5 Bibliography 157

6 Conclusion and Future Work **161**

1 | Introduction

1.1 The Need for Batteries

A battery is an electrochemical cell that stores energy as it is charged and releases that energy for use while it is discharged. It comprises of a positive electrode (cathode), a negative electrode (anode), and an electrolyte usually with a separator to prevent a continuous electronic circuit through the electrolyte. The two electrodes are the main reactive components of the cell where electrical energy is converted into chemical potential energy through reduction-oxidation (redox) reactions. The electrolyte provides an ionically conducting but electronically insulating connection between the electrodes. The battery is charged by simultaneously reducing the anode and oxidising the cathode, while the charge neutrality is maintained by the migration of alkali cations from the cathode to the anode and an electric current passing through the external circuit. The process is reversed during discharge. Chemical potential is the change in the energy of a system if an additional particle were introduced, with the entropy and volume kept constant. Each electrode has a chemical potential which depends on the chemical composition of the electrode material. The difference between the chemical potentials of the positive and negative electrodes determines the equilibrium voltage of the cell, as shown in the Nernst equation below,

$$E = -\frac{\mu^{+ve} - \mu^{-ve}}{zF} = -\frac{\Delta G}{zF} \tag{1.1}$$

where E is the equilibrium cell voltage, μ^{+ve} and μ^{-ve} are the chemical potentials of the

positive and negative electrodes respectively, z is the charge of the carrier ion, F is the Faraday constant, and ΔG is the Gibbs free energy of the system. A more convenient method to define cell voltage is to measure the voltage of the positive and negative electrodes against a suitable reference, like the standard hydrogen electrodes (SHE) or Li^+/Li, and calculate the difference between them. Two important parameters that are often used to represent battery performances are energy density (gravimetric: $\mathrm{W\,h\,kg^{-1}}$, volumetric: $\mathrm{W\,h\,L^{-1}}$) and power density (gravimetric: $\mathrm{W\,kg^{-1}}$, volumetric: $\mathrm{W\,L^{-1}}$). Energy density refers to the amount of energy that can be stored in a battery per unit mass, while power density refers to how quickly a battery can discharge its energy. Both can be improved by increasing the cathode potential and reducing the anode potential. On the anode side, one way to do this is to employ a metal anode like lithium.

Since their commercialisation by Sony in 1991, rechargeable, or secondary, lithium-ion batteries (LIBs) have revolutionised portable electronic devices such as mobile phones, laptops, and tablets. The pursuit of improved energy storage is currently one of the most important scientific challenges. As countries around the globe are racing towards net zero, energy storage will play an integral role in electrifying transport and enabling high penetration of renewable energy sources, which are often intermittent. Transportation and power sectors account for $\approx$ 40 % and 23 %, respectively, of global greenhouse gases (GHG) emissions annually. Despite revolutionising portable electronic devices, current LIBs cannot meet the requirements of next-generation technologies. The gap between current and future energy storage demands cannot be met by incremental improvements in their performance. To achieve the transformational improvements in energy and power densities, safety, cost, and lifetime required for future applications, it is necessary to look

for alternative battery architectures beyond LIBs with the potential for radical enhancements in performance. Solid-state batteries (SSBs) with metal anodes are an example of such an architecture. SSBs not only offer higher energy densities, but also battery safety due to the use of solid electrolytes (SEs) in place of organic solvents, which are often highly flammable. Another important consideration when designing and developing battery materials, including SEs, is the cost and availability of battery materials for mass production. Falling battery prices have been one of the trends that jump-started one of the biggest shifts in the auto industry. In 2010, the LIB pack prices were above $\$1200/\mathrm{kWh}$. By 2021, the price has fallen by 89% to $\$132/\mathrm{kWh}$ [35]. However, this trend has ground to a halt in 2022, with an increase in average pack prices by 7% compared to the previous year [5]. This is mainly due to rising costs for materials including cobalt, nickel and lithium. With the global demand for Li-ion batteries projected to surge from about 700 GWh in 2022 to around 4.7 TWh by 2030 [27], there is a need to search for complementary technologies to help meet the increasing demand for batteries and keep the price affordable for mass adoption. Sodium-based batteries are one approach to this problem []. This thesis will explore both lithium and sodium technologies.

1.2 Metallic Anodes

Lithium metal is the lightest member of the alkali metal group with the smallest atomic radius of all metals. It is regarded as the 'Holy Grail' electrode and received extensive research attention due to its extra-high theoretical capacity ($3860\,\mathrm{mA\,h\,g^{-1}}$) and lowest negative electrochemical potential ($-3.04\,\mathrm{V}$ compared to the standard hydrogen electrode) [88, 129, 10]. Unlike traditional LIBs, which work based on the lithium ion intercalation

mechanism, lithium metal batteries (LMBs) undergo a conversion reaction with a direct Li^+/Li^0 deposition/dissolution process. This can unlock a theoretical specific capacity almost 10 times higher than commercial graphite anode. However, the practical applications of LMBs are faced with numerous challenges. The high reactivity of lithium metal leads to severe spontaneous reactions with almost any organic liquid electrolytes [16]. As a result, an irreversible and continuous formation of solid electrolyte interphase (SEI) occurs on the electrode/electrolyte interface. This includes substantial active materials loss and therefore low Columbic efficiency [60, 16]. In addition, heterogeneous deposition of lithium can result in uncontrolled lithium dendrite formation and growth. This can subsequently trigger the formation of electrically insulated 'dead Li' and intense electrolyte consumption, leading to increased cell polarisation, shorter lifespan of LMBs, and even serious risk of explosion [111, 15, 45].

The commercialisation of rechargeable LMBs was first attempted by Moli Energy in the late 1980s [96]. The intercalated cathodes pioneered by John Goodenough and Stanley Whittingham, like TiS_2, Li_xMO_2 (where M is Co, Ni, or Mn), and MoS_2 were adopted. These batteries demonstrated high energy density of 100 - $200\,\mathrm{W\,h\,kg^{-1}}$ and 200 - $300\,\mathrm{W\,h\,L^{-1}}$ [10]. The AA-size Li/MoS_2 cells for phone and laptop manufacturers started to be shipped to cell phones and manufacturers in Japan in December 1988. However, four months later, numerous fire accidents occurred in those cells, leading to a total recall by Moli Energy [110]. This incident along with the challenges faced by LMBs mentioned above motivated researchers to search for alternative electrolytes for LMBs, including solid-state electrolytes.

While solid-state lithium metal batteries have significant potential to meet the require-

ments for higher energy density applications with improved safety, they face a significant scarcity problem they have to compete for lithium with current LIBs [18, 114]. As a result, sodium metal batteries have also been attracting a lot of attention due to their high abundance (1200 times more common than lithium) and wide distribution of sodium resources [59]. Moreover, sodium does not form alloys with aluminium. This means that an aluminium current collector can be used in place of copper which leads to further reduction in cost and weight of the battery [81, 105]. Benefiting from sodium's high theoretical specific capacity ($1165\,\mathrm{mA\,h\,g^{-1}}$) and low electrochemical potential (-2.714 V vs. standard hydrogen electrode) [105], the use of sodium metal as an anode can boost overall battery capacity, enabling the next generation of low-cost and high-capacity batteries. Like with lithium, combining a sodium metal anode with an organic liquid electrolyte presents very serious leakage and safety risks [104, 61, 94, 47, 117, 8]. The high chemical activity of sodium metal anodes can lead to unavoidable side reactions and uncontrolled dendrite growth, leading to continuous decline in electrochemical performance and potentially internal short circuits, thermal runaway, and even fires [56, 67, 112, 101, 93]. Solid-state sodium metal batteries (SSMBs) have been proposed as alternatives.

1.3 Solid Electrolytes

A key component of all-solid-state batteries (ASSBs) is its solid electrolyte (SE). Ideally, SEs should have excellent ionic conductivity, compressibility, electrochemical stability window, humidity tolerance, and cost-effectiveness [75, 76, 123, 65, 125]. The ionic conductivity is important because it determines the ion transport efficiency and indirectly influences the energy density. An ionic conductivity of $0.1\,\mathrm{mS\,cm^{-1}}$ at room tempera-

ture (RT) would not be enough; instead, ionic conductivities above $1\,\mathrm{mS\,cm^{-1}}$, which are comparable to those of commonly used liquid electrolytes like $LiPF_6$, are desired [116]. Compressibility depends on the mechanical properties, such as Young's modulus, of the SE materials. It determines the quality of the contact between the electrolytes and the electrodes. Higher compressibility would allow the solid-electrolyte to cover a larger area of the active material particles under pressure [38]. The electrochemical stability window refers to gap between the potential of electrolyte reduction at negative potentials, and of the potential of electrolyte oxidation at positive potentials, as seen in Figure 1.1 [80]. In redox reaction, energy is released when an electron loses potential energy as a result of the transfer; this is known as redox energy. To ensure the stability of a cell, the electrochemical stability window of the electrolyte should be wider than the charge/discharge potential during the electrochemical cycle. A wider electrochemical stability window ($\geqslant 4\,\mathrm{V}$) will also ensure the safe employment of high voltage cathodes to further improve the energy density in the ASSBs [116]. For most liquid electrolytes, moisture is avoided at all costs due to salt decomposing into HF gas when it comes into contact with H_2O. This leads to slow transmission of Li^+/Na^+, deterioration of cycle performance, and lower Coulombic efficiency [7, 113, 55]. Similarly, most of the inorganic SEs suffer from an unwanted reaction with air. Moreover, the air-sensitivity greatly increases the manufacturing difficulty and the cost of battery cell assembly. Therefore, SEs with a good humidity tolerance are highly desirable [9, 38]. Last but not least, the target materials cost of solid electrolytes is $\$50\,\mathrm{kg^{-1}}$ [2]. Above this, ASSBs would not be competitive against the current commercial LIBs.

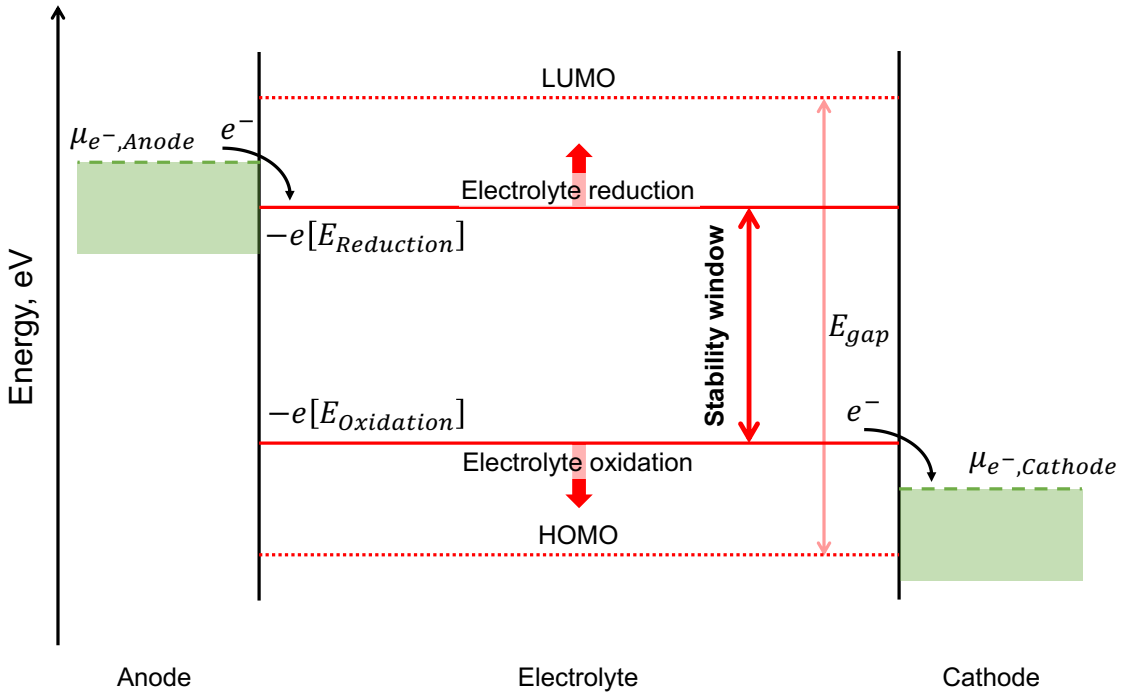

Figure 1.1: Schematic illustrating the negative and positive potential limits for the electrolyte stability, along with the energy levels of highest occupied molecular orbital (HOMO) and lowest unoccupied molecular orbital (LUMO).

At the present, based on the differences in the transport mechanism and chemical composition, SEs can be divided into three major categories: inorganic solid-state electrolytes (ISEs), polymer solid-state electrolytes (PSEs), and composite solid-state electrolytes (CSEs). In this section, we will review lithium and sodium SEs in all three categories.

1.3.1 Inorganic Solid-state Electrolytes (ISEs)

ISEs are mainly categorised into oxide-based, like NASICON, LISICON, perovskite, anti-perovskite, and garnet, and sulfide-based, such as Thio-LISICON and $Li_2S-M_xS_Y$ [56]. Both can exist in a crystalline or glassy state. They can support battery operation at low and high temperatures (for example, -50 to 200 °C or higher) in which a conventional liquid electrolyte would fail to do so [22]. There are 3 types of principal migration

mechanisms of Li^+/Na^+ in the ISEs: a vacancy diffusion mechanism where the mobile charged species migrate or hop from one vacant site to the adjacent vacant site, a direct interstitial mechanism where the interstitial Li^+/Na^+ hop from one interstitial site to the unoccupied neighbouring interstitial site, and finally a correlated interstitial mechanism where migration interstitial Li^+/Na^+ enter the adjacent site by substituting the adjacent lattice ion [56, 22]. Schematic depicting these 3 mechanisms can be found in Figure 1.2. The charge carrier concentration, diffusion type, defect concentration, and migration path hugely affect the thermodynamics and kinetics of Li^+/Na^+ conduction in ISEs. Compared with PSEs, ISEs generally have wider electrochemical stability windows, higher ionic conductivity at room temperature, and higher shear modulus [61, 124]. However, ISEs, especially for sulfide SEs, still suffer from problems such as large interfacial resistance, and poor interface compatibility and stability between electrode and electrolyte. These become the bottleneck for further development of ASSBs [65, 62, 97, 22, 82]. Summary of the ionic conductivities of the different classes of SEs can be found in Table 1.1.

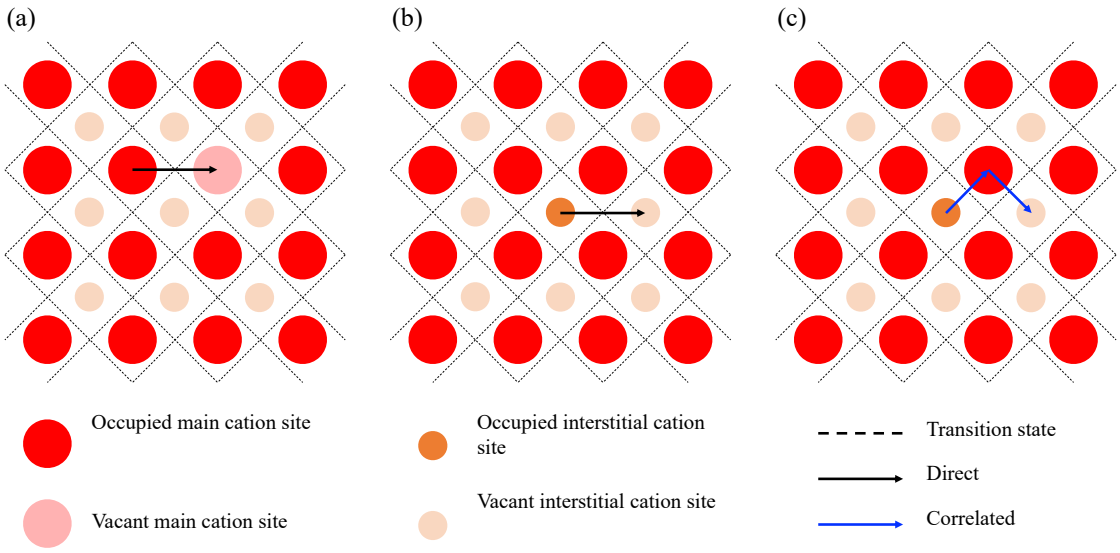

Figure 1.2: Schematic depicting 3 principal migration mechanisms of Li^+/Na^+ in the ISEs: (a) vacancy diffusion, (b) direct interstitial, and (c) correlated interstitial.

1.3.2 Polymer Solid Electrolytes (PSEs)

Unlike ISEs which tend to be brittle, PSEs are highly flexible. Their flexibility improves interfacial contact with electrode materials and enhances the stability of electrode volume changes upon cycling [79]. However, at ambient temperature, most polymer hosts are crystalline and so the motion of their chain segments is very limited. This results in poor ionic conductivity compared to those of ISEs and liquid electrolytes. Various high-molecular weight dielectric polymer hosts like polyvinylidene fluoride (PVDF), polyethylene oxide (PEO), polymethyl methacrylate (PMMA), and polyarylonitrile (PAN) have attracted attention due to their relatively high ionic conductivities compared to those of low-molecular weight dielectric polymer hosts [17, 89, 26]. Among them, PEO is the most studied due to its ability to solvate a wide variety of salts through the interaction of its ether oxygen with cations. PEO has high Li-ion conductivity at temperatures above $60\,^{\circ}\mathrm{C}$ due to its low glass transition temperature and high oxygen density. PEO-based SPEs have not been used in commercial applications due to their low ionic conductivities at RT ($10^{-8} - 10^{-6}\ \mathrm{S\,cm^{-1}}$) and poor electrochemical stability. There is extensive research that focus on addressing these challenges. Strategies that have been explored include crosslinking, copolymerisation, and blending with other polymers [79, 44, 28].

1.3.3 Composite Solid Electrolytes (CSEs)

CSEs are formed by incorporating inorganic fillers (active or passive fillers) into PSEs. This compromise solution was suggested to overcome the interfacial compatibility between ISEs and achieve reasonable ionic conductivities, while maintaining the mechanical strength and stability of the SE [91, 57, 36, 121]. The current ionic conductivities of

CSEs are in the range of $10^{-5} - 10^{-4}\,\mathrm{S\,cm^{-1}}$ at RT [56]. Further increase in the ionic conductivity of solid electrolytes to achieve comparable ionic conductivity with liquid electrolytes ($10^{-3} - 10^{-2}\,\mathrm{S\,cm^{-1}}$) is still a challenge [17, 79]. More importantly, the conduction mechanism in various composite solid electrolytes with different organic polymer matrix and inorganic filler still need to be explored more deeply. A combination of both experimental and theoretical calculations is required to understand the performance of materials and optimise the CSEs' structures and compositions [17].

Category	ISEs	PSEs	CSEs
Reported ionic conductivities ($\mathrm{S\,cm^{-1}}$)	$10^{-10} - 10^{-3}$	$10^{-8} - 10^{-4}$	$10^{-5} - 10^{-4}$

Table 1.1: Summary of the ionic conductivities of the different classes of SEs [79, 56, 58].

1.3.4 The Solid Electrolyte Challenge

At present, both single and composite solid electrolyte (SE) systems have been unable to meet the ever-increasing requirements for practical applications. These requirements include excellent ionic conductivity (comparable to that of liquid electrolyte, $1\,\mathrm{S\,cm^{-1}}$), the formation of a stable solid electrolyte interface (SEI) against a metal anode, a wide electrochemical stability window (> $4.5\,\mathrm{V}$), stability in air, and cost-effectiveness. It is harder to understand what governs the behaviour of a CSE if the behaviour of its constituent materials (ISE and PSE) is not well understood. Thus, in this thesis we chose to focus on antiperovskite, a single ISE system which has been reported to have great stability against metal anodes, low synthesis temperatures (< $500\,^{\circ}\mathrm{C}$), and relatively soft mechanical properties (bulk modulus for Na system $\approx 60\,\mathrm{GPa}$) compared to other solid electrolytes like NASICON [107, 70]. Moreover, the reported room temperature ionic

conductivity of antiperovskites varies widely ($10^{-8} - 10^{-2}$ $\mathrm{S\,cm^{-1}}$) depending on the measurement methods, chemical composition, and pellet processing conditions [12]. The reason for this is still a subject of considerable debate. Overall, antiperovskites are a relatively new family of SE, which have not been widely explored. However, they have the potential to become a suitable solid electrolyte for next generation batteries with metallic anodes such as sodium metal and lithium metal.

1.4 Antiperovskites

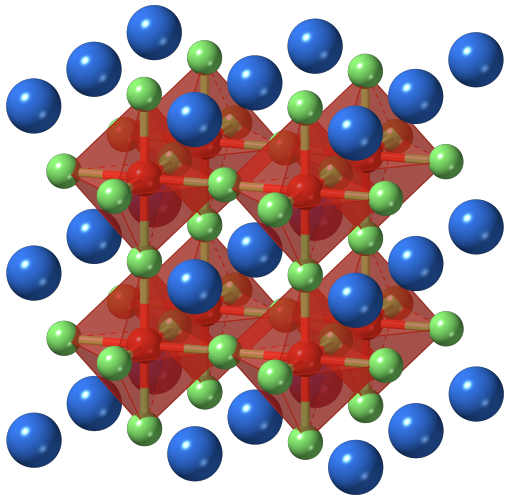

Figure 1.3: Schematic depicting crystal structure of antiperovskite where the blue atoms are divalent anions (A), the green atoms are cations (X), and the red atom is the monovalent anion (B).

Antiperovskites are inorganic compounds with a perovskite structure but with cations replaced by anion and vice versa. Their general formula is X_3AB(X = Li, Na, K, etc.; A = O, S, etc.; B = Cl, Br, I, BH_4, etc.) [12, 128]. The ideal antiperovskite structure is cubic with $Pm\bar{3}m$ space group but can also readily exhibit orthorhombic, tetragonal, rhombohedral and hexagonal phases, depending on pressure, temperature, and the composition of the material [68, 3]. Antiperovskites can behave as semiconductors, insulators and even superconductors, and they can exhibit a range of interesting physical properties, including zero thermal expansion (e.g. Mn_3GaC) [39], non-Arrhenius behaviour (e.g. K_3OI [127], and superconductivity (e.g. Ni_3MgC) [40]. This shows that antiperovskites have the potential to be used in many different applications. In this thesis, we will focus on Li- and Na-rich anti-perovskites for solid-state metal battery applications, which have experienced a remarkable rise in interest in recent years.

1.4.1 Fundamentals and History

The Goldschmidt tolerance factor, *t*, is a dimensionless parameter calculated from the ratio of the ionic radii of the constituent ions in the material. It is often used to predict the stability of an antiperovskite structure [68, 30]. For an antiperovskite with the general formula of X_3AB, it can be written as

$$t = \frac{r_A + r_X}{\sqrt{2}(r_B + r_X)} \tag{1.2}$$

where r_A, r_B and r_X are the radii of the A, B and X ions, respectively. A value of $t = 1$ represents the perfect case for the formation of a cubic structure. It is possible to synthe-

sise antiperovskites with $t = 0.8 - 1$. However, as the *t* value gets lower, the structure becomes more distorted and the symmetry decreases [68, 98]. This results in deviations from the ideal cubic structure. Despite having a tolerance factor which falls above identified range, there has not been a successful synthesis of Li^- or Na^- antiperovskites with S^{2-} on the B site [94, 1, 115]. Larger A-site cations and smaller B-site anions that push the tolerance factor closer to unity do not necessarily lead to synthesisable compositions. Some limitations associated with the tolerance factor might be linked directly to the Shannon radii values used as the input parameters [87]. For example, in the case of halides containing antiperovskites, the Shannon radii values reported may not be an accurate representation of the 12-coordinate sites they occupy [87]. Moreover, the Li and Na in antiperovskites are bonded to both O and halide, leading to asymmetric bond lengths [1]. In the case of antiperovskites containing cluster anions (e.g. BH_4^- and BF_4^-), there is no straightforward method to approximate an equivalent spherical radius for a non-spherical molecular anion [12]. Therefore, it is possible that the Shannon radii used to calculate the Goldschmidt tolerance factor do not fully capture the environment of the ions inside antiperovskites, thus contributing to inaccuracies. A practical solution that has been proposed is to utilise thermochemical radii, where the atomic and cluster species radii can be derived self-consistently [84, 43]. It is derived from thermodynamic calculations of the lattice energy of crystals and is agnostic to the crystal structure, shape and orientation of cluster ions. All ions are treated as spherical, deriving an equivalent spherical radius [12]. Despite the challenges associated with predicting the stability of antiperovskites, experimentally the challenge with synthesising most of the Li- and Na- antiperovskites is related to their hygroscopic nature. It is important to keep the H_2O and O_2 content inside

the glovebox below 0.1 ppm.

The first structural and conductivity analyses of Li-rich anti-perovskites (LiRAPs) Li_2OHBr and Li_2OHCl were reported by Hartwig et al. in 1981 [33, 34]. In these materials, two-thirds of the X sites are occupied by Li ions while the rest are vacant. The A and B sites are fully occupied by hydroxyl and halide groups, respectively. Despite the high lithium vacancy concentration, the ionic conductivity of Li_2OHBr and Li_2OHCl at 473 K was 5×10^{-5} and $3 \times 10^{-5}\ \mathrm{S\,cm^{-1}}$, respectively [33, 34]. The dehydrated form of Li_2OHBr, Li_3OBr, was first reported by Wortmann et al. in 1989 [108]. This material shares the same cubic structure as Li_2OHBr but all the lithium sites are fully occupied. In 2012, Zhao and Daemen reported superionic conductivity in Li_3OCl of $> 10^{-3}\ \mathrm{S\,cm^{-1}}$ at room temperature with low activation energies ($0.2 - 0.3\ \mathrm{eV}$) [126]. They reported that Li_3OCl was synthesised via solid-state methods, but very limited synthetic details were provided. The technique used to confirm the structure and composition of both Li_2OHCl and Li_3OCl in these studies was limited to X-ray diffraction, which is not sensitive to lighter elements like hydrogen and lithium. In addition, only raw diffraction patterns were presented, with no corresponding Rietveld analysis performed. Hence, the differentiation between a dry and hydrated state is not possible. Due to the favourable hydration of Li_3OCl, it makes it very difficult to prepare H-free Li_3OCl samples. Moreover, Li_2OHCl is thermodynamically stable while Li_3OCl is not thermodynamically stable at room temperature [21, 72, 109, 48]. Thus, it has been suggested that the as-prepared samples presented by Zhao and Daemen were in fact the hydrated composition. Yet, the ionic conductivity values of their sample and the one reported by Hartwig et al. earlier are very different [126, 34].

Most of the syntheses of Na-rich antiperovskites (NaRAPs) reported were via the solid-state route [74, 95, 130, 1, 99, 106]. Similar to the synthesis of LiRAP, trace amounts of the sodium halides for compositions containing halide ions are often observed as impurities in NaRAP [74, 106]. The first report of NaRAPs was Na_3NO_3 by Zintl and Morawietz in 1938 [131]. 50 years later, the first synthesis of Na_3OCl and Na_3OBr was reported by Sabrowsky et al. [85]. It was not until the early 1990s the ionic conductivity of Na_3NO_3 and Na_3OBr was studied by Jansen et al. [73, 41]. They reported a non-Arrhenius sodium-ion conductivity behaviour at elevated temperatures for each of these materials. In Na_3OCN, the Na-ion conductivity increased by around three orders of magnitude at 500 K [41]. In the case of Na_3NO_3 and Na_3OCN, this behaviour was attributed to either melting of the sodium sublattice or the rotational disorder of the NO_2^- and CN^- anions. The coupling between cation transport and the rotational motion of anions is known as the 'paddlewheel' mechanism [23, 90, 42, 122]. According to this mechanism, the dynamic rotational disorder of anions surrounding the cations could facilitate cation diffusional jumps. This occurs when the frequency of the anions' rotation matches the translation frequency of the cations [99]. Schematic depecting this mechanism can be found in Figure 1.4. Unlike the LiRAP system, there are currently no reports on Na_2OHA (A = Cl, Br, etc.) [12]. It is speculated this composition cannot be synthesised even though the radii of O^{2-} and OH^- are practically identical. This reversed trend between Li- and NaRAP systems cannot be easily explained through ionic radii arguments. There is likely a more fundamental consideration, such as formation energy, that needs to be taken into account [12].

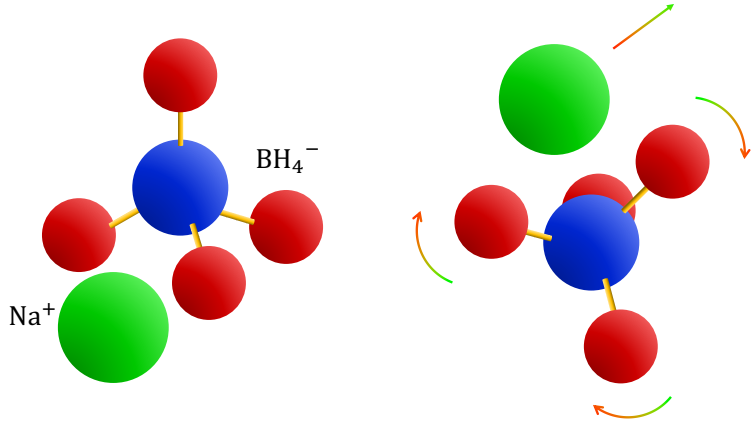

Figure 1.4: Schematic depicting 'paddlewheel' mechanism where the green atom is Na, the blue atom is B, and the red atoms are H.

1.4.2 The Surge of Interest

Recently, the surge of interest in antiperovskite materials is due to reports of their exceptional ionic conductivities. In 2012, Zhao and Daemen synthesised $Li_3OCl_{0.5}Br_{0.5}$ with a room temperature (RT) conductivity of $1.94 \times 10^{-3}\,\mathrm{S\,cm^{-1}}$ [126]. In 2014, Braga et al. developed glassy $Li_{(3-2x)}Ba_{(x)}OCl$ (x = 0.005) with an RT conductivity of 1.94 x $10^{-3}\,\mathrm{S\,cm^{-1}}$ [4]. In 2019, Sun et al. synthesised Na_3OBH_4 that reached $4.24 \times 10^{-3}\,\mathrm{S\,cm^{-1}}$ at RT after being hot-pressed at $100\,^{\circ}\mathrm{C}$, the highest among other Na_3OB (B = Cl, Br, BH_4) reported ionic conductivities [94]. Even though attempts to reproduce these results have had mixed success, these results give hope to the battery research community of finding a suitable solid electrolyte for solid-state batteries [1]. In addition, LiRAPs have been reported to have stable SEI against metal anodes, relatively soft mechanical properties (bulk modulus of NaRAPs $\approx 60\,\mathrm{GPa}$), and low synthesis and process temperatures ($< 500\,^{\circ}\mathrm{C}$), which can lead to easy processing and intimate contacts with electrodes [52, 74, 95, 130, 99, 106, 22, 13, 86].

On top of bulk synthesis routes, films of Li_3OCl were also reportedly fabricated via pulsed

laser deposition (PLD), using both a 'Li_3OCl' target and a composite of a Li_2O + LiCl target, and via radio frequency (RF) magnetron sputtering, using the same composite target [100, 63]. It is suggested that a composite target has greater stability than the pre-formed 'Li_3OCl' target and that it leads to a product with higher ionic conductivity at room temperature. An ionic conductivity of $2.0 \times 10^{-4}\ \mathrm{S\,cm^{-1}}$ was reported for the PLD with composite target, while that for the PLD with pre-formed Li_3OCl was $8.9 \times 10^{-6}\ \mathrm{S/cm}$ [63, 64]. The ionic conductivity was also reported for the sample synthesised using an RF magnetron sputterer. It is on the order of $10^{-8}\ \mathrm{S\,cm^{-1}}$ [100]. Characterisation by Fourier transform infrared spectroscopy (FTIR) confirmed the absence of O-H bonding in the films, providing evidence that the antiperovskite phase contained in this film was indeed Li_3OCl rather than Li_2OHCl. This low ionic conductivity was due to the low phase purity of the film. Based on the reports on Li_3OCl, the formation of this phase is experimentally challenging. This is actually supported by various computational studies which predict that Li_3OCl has a strong exothermic hydration enthalpy and a positive formation energy relative to a two-phase mixture of LiCl and Li_2O, which are often used as the precursors for syntheses of Li_3OCl via solid-state route [11, 20, 50]. Therefore, it is recommended that all studies on Li_3OCl be treated with a degree of caution.

1.4.3 Ionic Transport and Doping Strategies

Some doping strategies that have been suggested to improve the ionic conductivities of antiperovskites include halogen mixing, cationic doping, and a combination of the two. Lee et al. reported that among the $Li_2OHCl_{1-x}Br_x$ series, $Li_2OHCl_{0.9}Br_{0.1}$ has the highest ionic conductivity at room temperature of $2.52 \times 10^{-6}\ \mathrm{S\,cm^{-1}}$, while that of Li_2OHCl and

Li_2OHBr are $1.93 \times 10^{-6}\,\mathrm{S\,cm^{-1}}$ and $1.29 \times 10^{-6}\,\mathrm{S\,cm^{-1}}$ respectively [52]. Effat et al. reported significant improvement in ionic conductivity of Li_2OHCl with partial fluorination. Their reported ionic conductivities of Li_2OHCl, $Li_2(OH)_{0.9}F_{0.1}Cl$, and $Li_2OHF_{0.1}Cl_{0.9}$ at 373 K are $0.16 \times 10^{-3}\,\mathrm{S\,cm^{-1}}$, $0.94 \times 10^{-3}\,\mathrm{S\,cm^{-1}}$, and $4.78 \times 10^{-3}\,\mathrm{S\,cm^{-1}}$ [20]. Other doping strategies have been reported, including those by Braga et al. ($Li_{3-2x}M_xOA$ where M = Mg, Ca or Ba and A = Cl^- or I^-) [4], Zhang et al. ($Li_{3-x}Ca_{x/2}OCl$) [118], Dawson et al. (Li3-xOH_xCl) [11], and Li et al. ($Li_2(OH)_{1-x}F_xCl$) [54]. The degree of success for each strategy depends on the dopant species including their atomic size, the vacancy concentration, and the crystal structure of the antiperovskites after the doping. In the NaRAPs family, a different strategy has been explored to increase ionic conductivity. The main strategy involves replacing the halide anion(s) with cluster anion(s). Cluster anions are defined as anions composed of multiple atoms bound by covalent bonds such as hydroxide OH^- [52, 11], thiophosphate PS_4^{3-} [23, 32], borohydride BH_4^- [95, 1], and nitrate NO_2^- [42, 29]. The increase in ionic conductivity is due to an effect known as 'paddlewheel', where correlated rotations of cluster anions allow for cation translation with lower migration energy barriers, resulting in higher cation mobility. Sun et al. reported that ionic conductivity of Na_3OBH_4 reaches $4.24 \times 10^{-3}\,\mathrm{S\,cm^{-1}}$ at RT after being hot-pressed at $100\,^{\circ}\mathrm{C}$, the highest among other Na_3OB (B = Cl, Br, BH_4) [95]. However, attempts to reproduce these results have had mixed success, with the lowest reported value of $10^{-7}\,\mathrm{S\,cm^{-1}}$ at $100\,^{\circ}\mathrm{C}$ [1]. Another NaRAP that has been reported to have ionic conductivity nearly identical to that of Li_2OHCl is $Na_2(NH_2)(BH_4)$, ranging from 10^{-5} to $10^{-2}\,\mathrm{S\,cm^{-1}}$ over the temperature range $50 - 200\,^{\circ}\mathrm{C}$ [99]. Due to the relevant temporal (picoseconds) and spatial (angstroms) scales, it was challenging to physically characterise

the paddle-wheel mechanism. Recently, through a combination of neutron diffraction, nuclear magnetic resonance (NMR) spin lattice relaxation measurements, quasi-elastic neutron scattering, ab-initio molecular dynamic simulations, and other techniques, Tsai et al. revealed that the cation mobility in $Na_{3-x}O_{1-x}(NH_2)_x(BH_4)$ is influenced by the rotation of both amide anions (NH_2^-) and borohydride anions (BH_4^-) [99]. While the latter rotates faster than the earlier, only the rotation of the amide anions is closely synchronised with the translation of sodium ions during migration events. Selective freezing simulations showed a symmetric relationship between the amide and sodium ions but an asymmetric relationship between the borohydride and sodium ions. The paddle wheel effect in solid-ion conductors is said to exist when the rotational dynamics of a complex anion directly facilitate the mobility of a cation. Therefore, Tsai et al. came up with the concept of 'indirect paddlewheel effect', as an explanation for the observed simulation results described above [99].

Given the crucial role ion transport plays in the performance, design, and utilisation of solid electrolytes for solid-state batteries, it is important to understand the underlying mechanistic features of ion transport, how to increase the ionic conductivity, and how to lower the activation energy. Experimentally, ionic conductivities are routinely reported. A combination of techniques like impedance spectroscopy, variable-temperature solid-state NMR spectroscopy, X-ray powder diffraction, and microscopy have been used to try and probe ion dynamics within antiperovskites. For the cubic phase of Li_2OHCl, Dawson et al. confirm Li-ion diffusion and OH^- rotation via PFG NMR experiments and variable ^2H MAS NMR [11]. Determining whether alkali vacancies or interstitials are the dominant charge carriers has been the subject of much debate, with arguments for both being

presented for a variety of different compositions [21, 72, 71, 66]. Experimentally, there are many factors that can influence the ion conduction capabilities of a system, including (dis)ordering, thermal/physical/electrochemical history of the sample, composition, pressure, and pellet texture. One of the biggest challenges in materials science is the ability to accurately determine the relationship between structure and dynamic properties [12]. It is now widely accepted that in order to gain a comprehensive structural understanding of a system, an experimental approach must be paired with a computational one [12]. Numerous computational studies currently exist for antiperovskite solid electrolytes [21, 72, 71, 66]. In contrast, there are relatively few experimental studies in which ion transport mechanisms have been identified and/or confirmed [99, 11]. To verify how an ion moves within a particular system, in-situ measurements are needed. At present, many of the characterisation methods are limited in their ability to perform such in-situ measurements, owing to factors such as hardware limitations or an inability to host systems that require specialist environments, such as air tightness. For example, in NMR spectroscopy, the temperature range over which ion mobility can be probed is often limited by conventional hardware [12]. Therefore, in this thesis, we focus on experimental studies to probe the origin of non-Arrhenius Na and Li ionic conductivity behaviour of antiperovksites.

Besides doping, post-synthesis processing like sintering has been reported to increase the ionic conductivity of antiperovskites [74, 95]. Sintering is a process where a solid is compacted and densified without melting to the point of liquefaction [46]. Traditionally, sintering is done by applying heat but it can also be accomplished by pressure, also known as cold-pressing, or a combination of heat and pressure, also known as hot-pressing, to

achieve the desired result. Modern theories on the mechanism of sintering argue that sintering occurs due to diffusion driven by the removal of surface free energy from pores [14]. There are 2 competing processes that can lead to equilibrium: densification and grain growth (coarsening). In the case of densification, atoms diffuse through the grain boundary into the pores. On the other hand, in the case of grain growth, the atoms diffuse from one grain into another grain with a bigger size. If GBs migrate faster than the pores, pores will get separated from the grain boundaries and trapped inside the grain, making it harder to densify. To realise full densification, trapped pores must be avoided. This requires GBs to remain stable or migrate at a low speed. The competition between densification and grain growth is hard to be completely avoided at a normal pressure level up to 100 MPa [31]. Therefore, in this thesis, a pressure of $370\,\mathrm{MPa}$ was used for both cold pressing and hot pressing. Sintering at an elevated temperature can significantly lower the pressure required for densification, although this might be accompanied by limited grain growth. In solid-state sintering, particle size and shape play an important role in controlling the final density of the sintered ceramics [83]. A high concentration of elongated particles can result in irregularly shaped pores, which are significantly harder to densify. Thus, finer spherical particles are usually preferred due to the increased contact surface area between particles relative to volume. Another factor to take into account is the heating rate of specimens. It was theorized that a faster heating rate promotes mass transfer, preferring densification over coarsening. There is an inverse relationship between the heating rate and the grain size of the sintered ceramics [92]. However, there might be a thermal gradient throughout the bulk of the specimen itself when the heating rate is too fast. In this thesis, a medium heating rate ($5\,^{\circ}\mathrm{C\,min^{-1}}$) was used to prevent cracking due

to a steep thermal gradient throughout the bulk of the specimen and due to instrument limitation.

1.4.4 Quest for Understanding: Antiperovskite Behaviours

Since the reported room temperature ionic conductivities of antiperovskites are generally quite low, it becomes important to understand how the ionic conductivities would behave at elevated temperatures. Most ionically-conducting solid materials with promising applications in batteries exhibit Arrhenius behavior [77, 78, 6]. The Arrhenius equation (Eq. (1.3)) provides a mathematical description for thermally activated processes, predicting that a small increase in temperature will result in a significant increase in ionic conductivity. According to this equation, a straight line is expected when plotting the natural logarithm of the ionic conductivity ($\ln \sigma$) against 1/temperature ($1/T$), as illustrated in Figure 1.5.

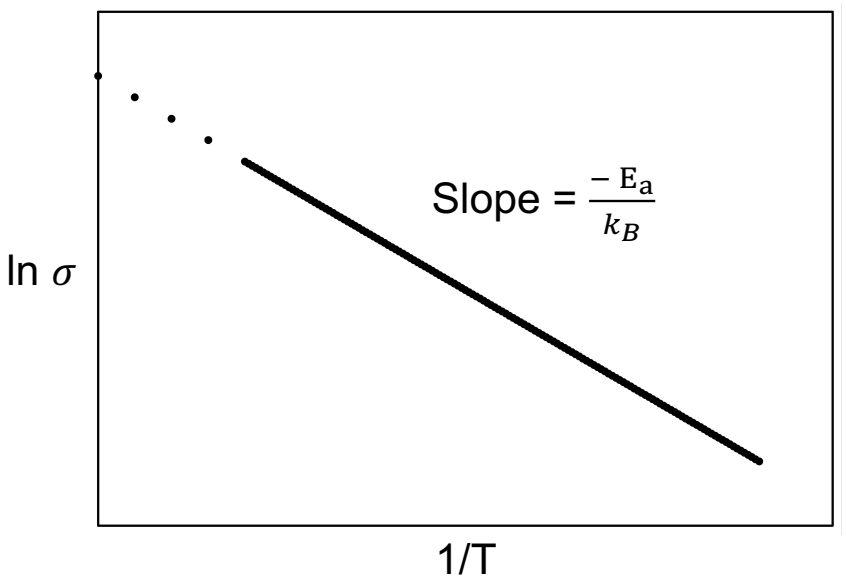

Figure 1.5: Schematic depicting a typical Arrhenius plot.

$$\sigma = \sigma_0 e^{\frac{-E_a}{k_B T}} \tag{1.3}$$

σ is the ionic conductivity, σ_0 is the pre-exponential factor, E_a is the activation energy for the thermally activated process, k_B is the Boltzmann constant, and T is the temperature. Interestingly, non-Arrhenius behavior, leading to a reduction in activation energy for ion conduction above $250\,^{\circ}\mathrm{C}$, has been observed across various antiperovskite compositions (Li, K, and Na) [127, 99, 29, 53, 41, 69, 25, 102]. In this context, non-Arrhenius behavior is defined as a deviation from a single straight line, including a step increase or decrease in the slope of the natural logarithm of the ionic conductivity ($\ln \sigma$) against 1/temperature ($1/T$) plot. The origin of this behaviour is not yet well understood. For antiperovskite compositions with cluster anions like $Na_3O(NO_2)$ and $Na_2(NH_2)(BH_4)$, the deviation from Arrhenius behaviour is often assigned to correlated motion between cluster anion rotations and the translating cation, as previously reported [29, 99]. However, for the compositions with single halide anions, such behaviour is usually attributed to structural instability, which includes order-disorder transitions of the ion sublattice, crystal melting, and phase transitions. Zheng et al. argued that the non-Arrhenius behaviour observed in K_3OI could be related to the effect of K vacancies on the ion kinetics of the system. K_3OI stays crystalline up to $350\,^{\circ}\mathrm{C}$ - well above the transition temperature of $240\,^{\circ}\mathrm{C}$ [127]. Through ab-initio molecular dynamics (AIMD) simulations, the authors demonstrated that local anion disordering is activated at elevated temperatures, and K-ions migrate not only via the K vacancies, but also through the relatively large vacancies around the disordered I-O sites, thus enhancing K-ion transport. Zhang et al. reported similar behaviour as the main driver for enhanced Li ionic mobility in Li_3OBr, and referred to the phenomenon as

'sublattice melting' [119, 120]. Additionally, similar behaviour is observed in Li_2OHCl and the origin is suggested to be different from that reported for K_3OI and Li_3OBr. Wang et al. argued that the defects on the Li site and the movement of H around the O atom give rise to a change in the ionic conductive pathway as temperature increases [103]. Despite the initial similarities across several antiperovskite families, the underlying causes of their non-Arrhenius behaviours are not the same. A comprehensive understanding of ion transport mechanisms, especially at elevated temperature for antiperovskites since the conductivity is significantly higher in this region, can provide design principles to improve the ionic conductivity of antiperovskite SEs.

As well as the bulk scale performance, like ionic conductivity, the suitability of an SE for practical applications also depends on its interfaces. These interfaces can be heterogeneous (e.g. electrode - electrolyte) or microstructural (e.g. grain boundaries) [19]. Both have the potential to be bottlenecks in the performance of solid-state batteries. In this thesis, we focus on the heterogeneous interfaces. There are a number of studies for antiperovskite SEs that focus on their interfacial stability and their microstructural characteristics. One prominent example of electrode-electrolyte interface work on antiperovskites is the work of Hood et al, where the interface between Li_2OHCl and Li metal was explicitly investigated [37]. The authors found that Li_2OHCl could form an extremely stable interface with the metallic Li anode. Even when symmetric cells with lithium electrodes were cycled at high temperatures ($\approx 200\,^{\circ}\mathrm{C}$), stability between the solid electrolyte and molten Li anode were maintained upon solid electrolyte interphase (SEI) formation, with minimal interfacial resistance. Energy dispersive X-ray (EDS) mapping of the SEI revealed that it is rich in oxygen, suggesting that the formation of a lithium oxide layer stabilises

the interface without significantly compromising the ionic conductivity. However, this also implies the reduction of the hydrogen proton and the evolution of hydrogen gas, which might be problematic in a practical setting. Regarding Na-based antiperovskites, Fan et al. designed an SSB with a doped monoclinic Na_3SO_4F antiperovskite solid electrolyte, Prussian blue cathode, and Na metal anode [24]. The first discharge capacity for this solid-state cell was $83.3\,\mathrm{mA\,h\,g^{-1}}$. However, after ten cycles, this capacity dropped to $34.5\,\mathrm{mA\,h\,g^{-1}}$ because of the poor interfacial stability or wettability of the Na metal used. When the Na metal anode was replaced with a Na-Sn alloy, a higher discharge capacity of $91.0\,\mathrm{mA\,h\,g^{-1}}$ was enabled for the first cycle and it was reasonably well maintained at $77.0\,\mathrm{mA\,h\,g^{-1}}$ after 20 cycles.

Due to the difficulties of explicitly modelling electrode-electrolyte interfaces, computational studies of electrode-antiperovskite electrolyte interfaces are scarce. An attempt was made by Kim and Siegel to probe the Li_3OCl-Li metal anode interface at the atomic scale using density functional theory (DFT) [49]. The authors found that the oxygen-terminated interface is the most thermodynamically stable, with the potential for low interfacial resistance. However, this strong interfacial interaction significantly reduced the electrochemical stability window of Li_3OCl, implying a trade-off between the two. The interfacial stability of Li_3OCl, Na_3OBr, and Na_4OI_2 has also been studied using a combination of DFT and thermodynamic calculations. Richards et al. predicted that oxidation is to occur from 3.00 V (relative to Li metal), with LiCl, $LiClO_3$, and ClO_3 as the products [82]. These decomposition products are electronically insulating. As a result, a passivated interphase can be formed at high voltages, which may prevent further oxidation of Li_3OCl. Lacivita et al. studied Na-based solid electrolytes and predicted an oxidation limit of 1.79

V (relative to metallic Na) for Na_3OBr, with Na_2O_2 and NaBr as decomposition products [51]. A similar value of 1.66 V (relative to Na metal) was obtained for Na_4OI_2, with NaI and $NaIO_3$ as decomposition products. These two limits are close to that of Na_2O (1.67 V, relative to metallic Na), consistent with the presence of fully reduced anions in those structures.

1.5 Thesis Objectives

SSBs with metal anodes are believed to be the way forward in the development of batteries with higher energy density and improved safety. Suitable SEs would be key to realise the potential of SSBs. Having been identified as promising SE family candidates, research on antiperovskite SEs is still in an early stage compared to other SEs like NASICON/ LISICON. This thesis provides significant practical value to researchers attempting to optimise the synthesis of NaRAPS, make more informed decisions on the suitability of NaRAPS as SEs for SSMBs, and understand the origins of the non-Arrhenius ionic conductivity behaviour in NaRAPs and LiRAPs. The thesis is organised as follows.

In Chapter 3, Na_3OBr, Na_3OCl, and Na_3OBH_4 were synthesised using two different Na_2O precursors, commercial and 'homemade'. Commercially available Na_2O contains approximately 20% Na_2O_2 impurity while 'homemade' Na_2O is highly pure. Syntheses with both precursors are common in the literature and have been reported to lead to successful NaRAP formation. In this chapter, a combination of X-ray diffraction (XRD) and nuclear magnetic resonance (NMR) was used to reveal that starting with a purer precursor reduces not only the amount of crystalline impurities but also poorly crystalline ones. The latter have often been overlooked by the research community in the past. The ef-

fects of the poorly crystalline impurities on the electrochemical performances of the final product will be elucidated in Chapter 4. With in-situ X-ray photoelectron spectroscopy (XPS), we provide evidence that NaRAPs are stable against Na metal. Additionally, using chronoamperometry, the electronic conductivities of all three compositions were found to be lower than those reported for NASICON. Overall, these findings provide experimental evidence which will accelerate the development of high-performance SEs.

In Chapter 4, we studied the non-Arrhenius ionic conductivity behaviour of Na_3OBr. Similar behaviour has been reported in other antiperovskite compositions and some have argued that this could be due to structural instability, which includes phase transitions, order-disorder transitions of the ion sublattice, and crystal melting. However, no clear experimental evidence has been provided to support these arguments. In this chapter, we systematically excluded crystallographic disorder on the anion sites as the cause of the change in activation energy. We then identified the presence of crystalline impurities, not detectable by XRD, and elucidated their effect on ionic conductivity. These findings improve understanding of the processing-structure-properties relationships pertaining to NaRAPs and highlight the need to determine these relationships in other materials systems, particularly the LiRAPs where the behaviour has been reported across different compositions.

In Chapter 5, with the techniques developed to uncover the origin of the non-Arrhenius behaviour in Na_3OBr, we investigated the origin of the similar behaviour in $Li_2OHCl_{0.9}Br_{0.1}$. The results reveal that despite the initial similarities, the origins of this behaviour in Na_3OBr and $Li_2OHCl_{0.9}Br_{0.1}$ are different. Non-linear changes in lattice parameter and thermal parameter of the halide ions are apparent in the $Li_2OHCl_0 \cdot 9\,Br_0 \cdot 1$, suggesting

that the transition involves bulk crystallographical changes.

1.6 Bibliography

[1] Ernest Ahiavi, James A. Dawson, Ulas Kudu, Matthieu Courty, M. Saiful Islam, Oliver Clemens, Christian Masquelier, and Theodosios Famprikis. Mechanochemical synthesis and ion transport properties of Na3OX (X = Cl, Br, I and BH4) antiperovskite solid electrolytes. *J. Power Sources*, 471:228489, 2020. ISSN 03787753. doi: 10.1016/j.jpowsour.2020.228489. URL `https://doi.org/10.1016/j.jpowsour.2020.228489`.

[2] Moran Balaish, Juan Carlos Gonzalez-Rosillo, Kun Joong Kim, Yuntong Zhu, Zachary D. Hood, and Jennifer L.M. Rupp. Processing thin but robust electrolytes for solid-state batteries. *Nature Energy*, 6(3):227–239, 3 2021. ISSN 20587546. doi: 10.1038/s41560-020-00759-5.

[3] A. S. Bhalla, Ruyan Guo, and Rustum Roy. The perovskite structure - A review of its role in ceramic science and technology. *Materials Research Innovations*, 4(1): 3–26, 2000. ISSN 14328917. doi: 10.1007/s100190000062.

[4] M. H. Braga, J. A. Ferreira, V. Stockhausen, J. E. Oliveira, and A. El-Azab. Novel Li3ClO based glasses with superionic properties for lithium batteries. *Journal of Materials Chemistry A*, 2(15):5470–5480, 4 2014. ISSN 20507496. doi: 10.1039/c3ta15087a.

[5] Nathaniel Bullard. Even High Battery Prices Can't Chill the Hot Energy Storage Sector, 1 2023. URL `https:`

//www.bloomberg.com/news/articles/2023-01-12/
even-high-battery-prices-can-t-chill-the-hot-energy-storage-sector
leadSource=uverify%20wall.

[6] R. J. Charles. Polarization and diffusion in a silicate glass. *Journal of Applied Physics*, 32(6):1115–1126, 1961. ISSN 00218979. doi: 10.1063/1.1736169.

[7] Ji Chen, Xiulin Fan, Qin Li, Hongbin Yang, M. Reza Khoshi, Yaobin Xu, Sooyeon Hwang, Long Chen, Xiao Ji, Chongyin Yang, Huixin He, Chongmin Wang, Eric Garfunkel, Dong Su, Oleg Borodin, and Chunsheng Wang. Electrolyte design for LiF-rich solid–electrolyte interfaces to enable high-performance microsized alloy anodes for batteries. *Nature Energy*, 5(5):386–397, 5 2020. ISSN 20587546. doi: 10.1038/s41560-020-0601-1.

[8] Xiang Chen, Xin Shen, Bo Li, Hong-Jie Peng, Xin-Bing Cheng, Bo-Quan Li, Xue-Qiang Zhang, Jia-Qi Huang, and Qiang Zhang. Ion–Solvent Complexes Promote Gas Evolution from Electrolytes on a Sodium Metal Anode. *Angewandte Chemie*, 130(3):742–745, 1 2018. ISSN 0044-8249. doi: 10.1002/ange.201711552.

[9] Xuanfeng Chen, Zengqiang Guan, Fulu Chu, Zhichen Xue, Feixiang Wu, and Yan Yu. Air-stable inorganic solid-state electrolytes for high energy density lithium batteries: Challenges, strategies, and prospects. *InfoMat*, 4(1), 1 2022. ISSN 25673165. doi: 10.1002/inf2.12248.

[10] Xin Bing Cheng, Rui Zhang, Chen Zi Zhao, and Qiang Zhang. Toward Safe Lithium Metal Anode in Rechargeable Batteries: A Review. *Chemical Reviews*,

117(15):10403–10473, 8 2017. ISSN 15206890. doi: 10.1021/acs.chemrev.7b00115.

[11] James A. Dawson, Tavleen S. Attari, Hungru Chen, Steffen P. Emge, Karen E. Johnston, and M. Saiful Islam. Elucidating lithium-ion and proton dynamics in anti-perovskite solid electrolytes. *Energy and Environmental Science*, 11(10): 2993–3002, 10 2018. ISSN 17545706. doi: 10.1039/c8ee00779a.

[12] James A. Dawson, Theodosios Famprikis, and Karen E. Johnston. Anti-perovskites for solid-state batteries: recent developments, current challenges and future prospects. *J. Mater. Chem. A*, 9(35):18746–18772, 2021. ISSN 20507496. doi: 10.1039/d1ta03680g.

[13] Zhi Deng, Zhenbin Wang, Iek-Heng Chu, Jian Luo, and Shyue Ping Ong. Elastic Properties of Alkali Superionic Conductor Electrolytes from First Principles Calculations. *Journal of The Electrochemical Society*, 163(2):A67–A74, 2016. ISSN 0013-4651. doi: 10.1149/2.0061602jes.

[14] Peter M Derlet. Sintering theory, 2017.

[15] Jun Fan Ding, Rui Xu, Chong Yan, Bo Quan Li, Hong Yuan, and Jia Qi Huang. A review on the failure and regulation of solid electrolyte interphase in lithium batteries. *Journal of Energy Chemistry*, 59:306–319, 8 2021. ISSN 20954956. doi: 10.1016/j.jechem.2020.11.016.

[16] Jun Fan Ding, Yu Tong Zhang, Rui Xu, Rui Zhang, Ye Xiao, Shuo Zhang, Chen Xi Bi, Cheng Tang, Rong Xiang, Ho Seok Park, Qiang Zhang, and Jia Qi Huang. Review on lithium metal anodes towards high energy density batteries. *Green*

Energy and Environment, (xxxx), 2022. ISSN 24680257. doi: 10.1016/j.gee.2022.08.002. URL https://doi.org/10.1016/j.gee.2022.08.002.

[17] Mahmut Dirican, Chaoyi Yan, Pei Zhu, and Xiangwu Zhang. Composite solid electrolytes for all-solid-state lithium batteries. *Materials Science and Engineering R: Reports*, 136:27–46, 4 2019. ISSN 0927796X. doi: 10.1016/j.mser.2018.10.004.

[18] Bruce Dunn, Haresh Kamath, and Jean-Marie Tarascon. Electrical Energy Storage for the Grid: A Battery of Choices System power ratings, module size. *Science*, 334(6058):928–935, 2011. URL https://www.science.org.

[19] Ana C. C. Dutra and James A. Dawson. Computational Design of Antiperovskite Solid Electrolytes. *The Journal of Physical Chemistry C*, 9 2023. ISSN 1932-7447. doi: 10.1021/acs.jpcc.3c04953.

[20] Mohammed B. Effat, Jiapeng Liu, Ziheng Lu, Ting Hei Wan, Antonino Curcio, and Francesco Ciucci. Stability, Elastic Properties, and the Li Transport Mechanism of the Protonated and Fluorinated Antiperovskite Lithium Conductors. *ACS Applied Materials and Interfaces*, 12(49):55011–55022, 12 2020. ISSN 19448252. doi: 10.1021/acsami.0c17975.

[21] Alexandra Emly, Emmanouil Kioupakis, and Anton Van Der Ven. Phase stability and transport mechanisms in antiperovskite Li 3OCl and Li3OBr superionic conductors. *Chemistry of Materials*, 25(23):4663–4670, 12 2013. ISSN 08974756. doi: 10.1021/cm4016222.

[22] Theodosios Famprikis, Pieremanuele Canepa, James A. Dawson, M. Saiful Islam, and Christian Masquelier. Fundamentals of inorganic solid-state electrolytes for batteries. *Nature Materials*, 18(12):1278–1291, 12 2019. ISSN 14764660. doi: 10.1038/s41563-019-0431-3.

[23] Theodosios Famprikis, James A. Dawson, François Fauth, Oliver Clemens, Emmanuelle Suard, Benoit Fleutot, Matthieu Courty, Jean Noël Chotard, M. Saiful Islam, and Christian Masquelier. A New Superionic Plastic Polymorph of the Na+Conductor Na3PS4. *ACS Materials Letters*, 1(6):641–646, 12 2019. ISSN 26394979. doi: 10.1021/acsmaterialslett.9b00322.

[24] Shengsheng Fan, Meng Lei, Han Wu, Jiulin Hu, Congling Yin, Tongxiang Liang, and Chilin Li. A Na-rich fluorinated sulfate anti-perovskite with dual doping as solid electrolyte for Na metal solid state batteries. *Energy Storage Materials*, 31: 87–94, 10 2020. ISSN 24058297. doi: 10.1016/j.ensm.2020.05.030.

[25] Wuliang Feng, Lei Zhu, Xiaoli Dong, Yonggang Wang, Yongyao Xia, and Fei Wang. Enhanced Moisture Stability of Lithium-Rich Antiperovskites for Sustainable All-Solid-State Lithium Batteries. *Adv. Mater.*, 35(12):2210365, 3 2023. ISSN 15214095. doi: 10.1002/adma.202210365.

[26] Jeffrey W. Fergus. Ceramic and polymeric solid electrolytes for lithium-ion batteries. *Journal of Power Sources*, 195(15):4554–4569, 8 2010. ISSN 03787753. doi: 10.1016/j.jpowsour.2010.01.076.

[27] Jakob Fleischmann, Patrick Schaufuss, Martin Linder, Mikael Hanicke, Evan Horetsky, Dina Ibrahim, Soren Jautelat, Lukas Torscht,

and Alexandre van de Rijt. Battery 2030: Resilient, sustainable, and circular, 1 2023. URL https://www.mckinsey.com/industries/automotive-and-assembly/our-insights/battery-2030-resilient-sustainable-and-circular.

[28] Maria Forsyth, Luca Porcarelli, Xiaoen Wang, Nicolas Goujon, and David Mecerreyes. Innovative Electrolytes Based on Ionic Liquids and Polymers for Next-Generation Solid-State Batteries. *Accounts of Chemical Research*, 52(3):686–694, 3 2019. ISSN 15204898. doi: 10.1021/acs.accounts.8b00566.

[29] Lei Gao, Hao Zhang, Yuechao Wang, Shuai Li, Ruo Zhao, Yonggang Wang, Song Gao, Lunhua He, Hai Feng Song, Ruqiang Zou, and Yusheng Zhao. Mechanism of enhanced ionic conductivity by rotational nitrite group in antiperovskite Na3ONO2. *J. Mater. Chem. A*, 8(40):21265–21272, 10 2020. ISSN 20507496. doi: 10.1039/d0ta07110b.

[30] V. M. Goldschmidt. Die Gesetze der Krystallochemie. *Naturwissenschaften*, 14: 477–485, 1926.

[31] Junfeng Gu, Ji Zou, Jianghao Liu, Hao Wang, Jinyong Zhang, Weimin Wang, and Zhengyi Fu. Sintering highly dense ultra-high temperature ceramics with suppressed grain growth. *Journal of the European Ceramic Society*, 40(4):1086–1092, 4 2020. ISSN 1873619X. doi: 10.1016/j.jeurceramsoc.2019.11.056.

[32] Isabel Hanghofer, Bernhard Gadermaier, and H. Martin R. Wilkening. Fast Rotational Dynamics in Argyrodite-Type Li6PS5X (X: Cl, Br, I) as Seen by 31P Nuclear Magnetic Relaxation - On Cation-Anion Coupled Transport in Thiophos-

phates. *Chemistry of Materials*, 31(12):4591–4597, 6 2019. ISSN 15205002. doi: 10.1021/acs.chemmater.9b01435.

[33] P. Hartwig and W. Weppner. Ionic Conductivies of Lithium-Halide-Based Quaternary Compounds. *Solid State Ionics*, 3(4):249–254, 1981.

[34] P Hartwig, A Rabenau, and W Weppner. Lithium Hydroxide Halides: Phase Equilibria and Ionic Conductivies. *Journal of the Less-Common Metals*, 78:227–233, 1981.

[35] Veronika Henze. Battery Pack Prices Fall to an Average of $132/kWh, But Rising Commodity Prices Start to Bite, 11 2021. URL https://about.bnef.com/blog/battery-pack-prices-fall-to-an-average-of-132-kwh-but-rising-commo

[36] Koji Hiraoka, Masaki Kato, Takeshi Kobayashi, and Shiro Seki. Polyether/Na3Zr2Si2PO12Composite Solid Electrolytes for All-Solid-State Sodium Batteries. *Journal of Physical Chemistry C*, 124(40):21948–21956, 10 2020. ISSN 19327455. doi: 10.1021/acs.jpcc.0c05334.

[37] Zachary D. Hood, Hui Wang, Amaresh Samuthira Pandian, Jong Kahk Keum, and Chengdu Liang. Li2OHCl Crystalline Electrolyte for Stable Metallic Lithium Anodes. *Journal of the American Chemical Society*, 138(6):1768–1771, 2 2016. ISSN 15205126. doi: 10.1021/jacs.5b11851.

[38] Lv Hu, Jinzhu Wang, Kai Wang, Zhenqi Gu, Zhiwei Xi, Hui Li, Fang Chen, Youxi Wang, Zhenyu Li, and Cheng Ma. A cost-effective, ionically conductive and

compressible oxychloride solid-state electrolyte for stable all-solid-state lithium-based batteries. *Nature Communications*, 14(1), 12 2023. ISSN 20411723. doi: 10.1038/s41467-023-39522-1.

[39] Rongjin Huang, Laifeng Li, Fangshuo Cai, Xiangdong Xu, and Lihe Qian. Low-temperature negative thermal expansion of the antiperovskite manganese nitride Mn3 CuN codoped with Ge and Si. *Applied Physics Letters*, 93(8), 2008. ISSN 00036951. doi: 10.1063/1.2970998.

[40] T. He Huang, A. P. Ramirez, Y. Wang, K. A. Regan, N. Rogado, M. A. Hayward, M. K. Haas, J. S. Slusky, K. Inumara, H. W. Zandbergen, N. P. Ong, and R. J. Cava. Superconductivity in the non-oxide perovskite MgCNi3. *Letters to Nature*, 411:54–56, 2001.

[41] M. Jansen, C. Feldmann, and W. Müller. Über die quasi-binären Systeme NaNO2/Na2O und NaCN/Na2O. Phasendiagramme und Natrium-Ionenleitung in Na3O(NO2) und Na3O(CN). *Z. Anorg. Allg. Chem.*, 611(5):7–10, 1992. ISSN 15213749. doi: 10.1002/zaac.19926110502.

[42] Martin Jansen. Volume Effect or Paddle-Wheel Mechanism—Fast Alkali-Metal Ionic Conduction in Solids with Rotationally Disordered Complex Anions. *Angewandte Chemie International Edition in English*, 30(12):1547–1558, 1991. ISSN 15213773. doi: 10.1002/anie.199115471.

[43] H D B Jenkins and K P Thakur. Reappraisal of Thermochemical Radii for Complex Ions. *Journal of Chemical Education*, 56(9):576–577, 1979. URL `https://pubs.acs.org/sharingguidelines`.

[44] Kihun Jeong, Sodam Park, and Sang Young Lee. Revisiting polymeric single lithium-ion conductors as an organic route for all-solid-state lithium ion and metal batteries. *Journal of Materials Chemistry A*, 7(5):1917–1935, 2019. ISSN 20507496. doi: 10.1039/c8ta09056d.

[45] Feng-Ni Jiang, Shi-Jie Yang, He Liu, Xin-Bing Cheng, Lei Liu, Rong Xiang, Qiang Zhang, Stefan Kaskel, and Jia-Qi Huang. Mechanism understanding for stripping electrochemistry of Li metal anode. *SusMat*, 1(4):506–536, 12 2021. ISSN 2692-4552. doi: 10.1002/sus2.37.

[46] Suk-Joong L. Kang. Sintering Processes. In *Sintering*, pages 3–8. 2005.

[47] Jae Kwang Kim, Young Jun Lim, Hyojin Kim, Gyu Bong Cho, and Youngsik Kim. A hybrid solid electrolyte for flexible solid-state sodium batteries. *Energy and Environmental Science*, 8(12):3589–3596, 12 2015. ISSN 17545706. doi: 10.1039/c5ee01941a.

[48] Kwangnam Kim and Donald J. Siegel. Correlating lattice distortions, ion migration barriers, and stability in solid electrolytes. *Journal of Materials Chemistry A*, 7(7):3216–3227, 2019. ISSN 20507496. doi: 10.1039/C8TA10989C.

[49] Kwangnam Kim and Donald J. Siegel. Predicting Wettability and the Electrochemical Window of Lithium-Metal/Solid Electrolyte Interfaces. *ACS Applied Materials and Interfaces*, 11(43):39940–39950, 10 2019. ISSN 19448252. doi: 10.1021/acsami.9b13311.

[50] Kwangnam Kim, Yiliang Li, Ping Chun Tsai, Fei Wang, Seoung Bum Son, Yet Ming Chiang, and Donald J. Siegel. Exploring the Synthesis of Alkali

Metal Anti-perovskites. *Chemistry of Materials*, 34(3):947–958, 2 2022. ISSN 15205002. doi: 10.1021/acs.chemmater.1c02150.

[51] Valentina Lacivita, Yan Wang, Shou Hang Bo, and Gerbrand Ceder. Ab initio investigation of the stability of electrolyte/electrode interfaces in all-solid-state Na batteries. *Journal of Materials Chemistry A*, 7(14):8144–8155, 2019. ISSN 20507496. doi: 10.1039/c8ta10498k.

[52] Hyeon Jeong Lee, Brigita Darminto, Sudarshan Narayanan, Maria Diaz-Lopez, Albert W. Xiao, Yvonne Chart, Ji Hoon Lee, James A. Dawson, and Mauro Pasta. Li-ion conductivity in Li2OHCl1-xBrx solid electrolytes: grains, grain boundaries and interfaces. *J. Mater. Chem. A*, 10(21):11574–11586, 4 2022. ISSN 20507496. doi: 10.1039/d2ta01462a.

[53] Yiliang Li, Ping-Chun Tsai, Fei Wang, Sunil Mair, Duhan Zhang, Liang Yin, Saul Lapidus, and Yet-Ming Chiang. Non-Arrhenius Ionic Conductivity Transitions in Sodium Antiperovskite Ionic Conductors. *ECS Meeting Abstracts*, MA2021-02(1): 43, 10 2021. doi: 10.1149/MA2021-02143mtgabs. URL `https://dx.doi.org/10.1149/MA2021-02143mtgabs`.

[54] Yutao Li, Weidong Zhou, Sen Xin, Shuai Li, Jinlong Zhu, Lü Xujie, Zhiming Cui, Quanxi Jia, Jianshi Zhou, Yusheng Zhao, and John B. Goodenough. Fluorine-Doped Antiperovskite Electrolyte for All-Solid-State Lithium-Ion Batteries. *Angewandte Chemie - International Edition*, 55(34):9965–9968, 2016. ISSN 15213773. doi: 10.1002/anie.201604554.

[55] Yutao Li, Henghui Xu, Po-Hsiu Chien, Nan Wu, Sen Xin, Leigang Xue, Kyusung

Park, Yan-Yan Hu, and John B. Goodenough. A Perovskite Electrolyte That Is Stable in Moist Air for Lithium-Ion Batteries. *Angewandte Chemie*, 130(28):8723–8727, 7 2018. ISSN 0044-8249. doi: 10.1002/ange.201804114.

[56] Zhaopeng Li, Pei Liu, Kunjie Zhu, Zhaoyuan Zhang, Yuchang Si, Yijing Wang, and Lifang Jiao. Solid-State Electrolytes for Sodium Metal Batteries. *Energy Fuels*, 35 (11):9063–9079, 2021. ISSN 15205029. doi: 10.1021/acs.energyfuels.1c00347.

[57] Zhuo Li, Wu Xin Sha, and Xin Guo. Three-Dimensional Garnet Framework-Reinforced Solid Composite Electrolytes with High Lithium-Ion Conductivity and Excellent Stability. *ACS Applied Materials and Interfaces*, 11(30):26920–26927, 7 2019. ISSN 19448252. doi: 10.1021/acsami.9b07830.

[58] Zhuo Li, Jialong Fu, Xiaoyan Zhou, Siwei Gui, Lu Wei, Hui Yang, Hong Li, and Xin Guo. Ionic Conduction in Polymer-Based Solid Electrolytes. *Advanced Science*, 10(10), 4 2023. ISSN 21983844. doi: 10.1002/advs.202201718.

[59] Scott Lilley. Sodium-ion Batteries: Inexpensive and Sustainable Energy Storage. *Faraday Insights*, 5 2021.

[60] Bin Liu, Ji Guang Zhang, and Wu Xu. Advancing Lithium Metal Batteries. *Joule*, 2(5):833–845, 5 2018. ISSN 25424351. doi: 10.1016/j.joule.2018.03.008.

[61] Lilu Liu, Xingguo Qi, Shijun Yin, Qiangqiang Zhang, Xiaozhi Liu, Liumin Suo, Hong Li, Liquan Chen, and Yong Sheng Hu. In Situ Formation of a Stable Interface in Solid-State Batteries. *ACS Energy Letters*, 4(7):1650–1657, 2019. ISSN 23808195. doi: 10.1021/acsenergylett.9b00857.

[62] Shuaifeng Lou, Fang Zhang, Chuankai Fu, Ming Chen, Yulin Ma, Geping Yin, and Jiajun Wang. Interface Issues and Challenges in All-Solid-State Batteries: Lithium, Sodium, and Beyond. *Advanced Materials*, 33(6), 2 2021. ISSN 15214095. doi: 10.1002/adma.202000721.

[63] Xujie Lü, Gang Wu, John W. Howard, Aiping Chen, Yusheng Zhao, Luke L. Daemen, and Quanxi Jia. Li-rich anti-perovskite Li3OCl films with enhanced ionic conductivity. *Chem. Commun.*, 50(78):11520–11522, 9 2014. ISSN 1364548X. doi: 10.1039/c4cc05372a.

[64] Xujie Lü, John W. Howard, Aiping Chen, Jinlong Zhu, Shuai Li, Gang Wu, Paul Dowden, Hongwu Xu, Yusheng Zhao, and Quanxi Jia. Antiperovskite Li3 OCl superionic conductor films for solid-state li-ion batteries. *Adv. Sci.*, 3(3):1500359, 3 2016. ISSN 21983844. doi: 10.1002/advs.201500359.

[65] Yong Lu, Lin Li, Qiu Zhang, Zhiqiang Niu, and Jun Chen. Electrolyte and Interface Engineering for Solid-State Sodium Batteries. *Joule*, 2(9):1747–1770, 9 2018. ISSN 25424351. doi: 10.1016/j.joule.2018.07.028.

[66] Ziheng Lu, Chi Chen, Zarah Medina Baiyee, Xin Chen, Chunming Niu, and Francesco Ciucci. Defect chemistry and lithium transport in Li3OCl anti-perovskite superionic conductors. *Physical Chemistry Chemical Physics*, 17(48): 32547–32555, 10 2015. ISSN 14639076. doi: 10.1039/c5cp05722a.

[67] Wei Luo, Chuan Fu Lin, Oliver Zhao, Malachi Noked, Ying Zhang, Gary W. Rubloff, and Liangbing Hu. Ultrathin Surface Coating Enables the Stable Sodium

Metal Anode. *Advanced Energy Materials*, 7(2), 1 2017. ISSN 16146840. doi: 10.1002/aenm.201601526.

[68] Helen D Megaw. Crystal Structure of Double Oxides of the Perovskite Ty[e. *The Proceedings of the Physical Society*, 58(326):133–152, 1946.

[69] Zerina Mehmedović, Vanessa Wei, Andrew Grieder, Patrick Shea, Brandon C. Wood, and Nicole Adelstein. Impacts of vacancy-induced polarization and distortion on diffusion in solid electrolyte Li3OCl. *Philos. Trans. R. Soc. A*, 379(2211): 20190459, 11 2021. ISSN 1364503X. doi: 10.1098/rsta.2019.0459.

[70] Kyoungmin Min. High-Throughput Ab Initio Investigation of the Elastic Properties of Inorganic Electrolytes for All-Solid-State Na-Ion Batteries. *Journal of The Electrochemical Society*, 168(3):030541, 3 2021. ISSN 0013-4651. doi: 10.1149/1945-7111/abf015.

[71] R. Mouta, E. M. Diniz, and C. W.A. Paschoal. Li+ interstitials as the charge carriers in superionic lithium-rich anti-perovskites. *Journal of Materials Chemistry A*, 4(5): 1586–1590, 2 2016. ISSN 20507496. doi: 10.1039/c5ta07450a.

[72] Rodolpho Mouta, Maria Aguida B Melo, Eduardo M Diniz, and Carlos William A Paschoal. Concentration of Charge Carriers, Migration, and Stability in Li3OCl Solid Electrolytes. *Chemistry of Materials*, 26(24):7137–7144, 12 2014. ISSN 0897-4756. doi: 10.1021/cm503717e. URL `https://doi.org/10.1021/cm503717e`.

[73] Winfried Müller and Martin Jansen. (CN)ONa3, Kristallstruktur und Natriumio-

nenleitfähigkeit. *ZAAC - Journal of Inorganic and General Chemistry*, 591(1): 41–46, 1990. ISSN 15213749. doi: 10.1002/zaac.19905910105.

[74] Han Nguyen, Sunny Hy, Erik Wu, Zhi Deng, Mojtaba Samiee, Thomas Yersak, Jian Luo, Shyue Ping Ong, and Ying Shirley Meng. Experimental and Computational Evaluation of a Sodium-Rich Anti-Perovskite for Solid State Electrolytes. *J. Electrochem. Soc.*, 163(10):A2165–A2171, 2016. ISSN 0013-4651. doi: 10.1149/2.0091610jes.

[75] Jin An Sam Oh, Linchun He, Anna Plewa, Masato Morita, Yue Zhao, Tetsuo Sakamoto, Xu Song, Wei Zhai, Kaiyang Zeng, and Li Lu. Composite NASICON (Na3Zr2Si2PO12) Solid-State Electrolyte with Enhanced Na+ Ionic Conductivity: Effect of Liquid Phase Sintering. *ACS Applied Materials and Interfaces*, 11(43): 40125–40133, 10 2019. ISSN 19448252. doi: 10.1021/acsami.9b14986.

[76] Jin An Sam Oh, Linchun He, Bengwah Chua, Kaiyang Zeng, and Li Lu. Inorganic sodium solid-state electrolyte and interface with sodium metal for room-temperature metal solid-state batteries. *Energy Storage Materials*, 34:28–44, 1 2021. ISSN 24058297. doi: 10.1016/j.ensm.2020.08.037.

[77] Yohei Okada, Masahiro Ikeda, and Masaru Aniya. Non-Arrhenius ionic conductivity in solid electrolytes: A theoretical model and its relation with the bonding nature. *Solid State Ionics*, 281:43–48, 11 2015. ISSN 01672738. doi: 10.1016/j.ssi.2015.08.020.

[78] Myounggu Park, Xiangchun Zhang, Myoungdo Chung, Gregory B. Less, and Ann Marie Sastry. A review of conduction phenomena in Li-ion batteries.

Journal of Power Sources, 195(24):7904–7929, 2010. ISSN 03787753. doi: 10.1016/j.jpowsour.2010.06.060.

[79] Mauro Pasta, David Armstrong, Zachary L. Brown, Junfu Bu, Martin R. Castell, Peiyu Chen, Alan Cocks, Serena A. Corr, Edmund J. Cussen, Ed Darnbrough, Vikram Deshpande, Christopher Doerrer, Matthew S. Dyer, Hany El-Shinawi, Norman Fleck, Patrick Grant, Georgina L. Gregory, Chris Grovenor, Laurence J. Hardwick, John T.S. Irvine, Hyeon Jeong Lee, Guanchen Li, Emanuela Liberti, Innes McClelland, Charles Monroe, Peter D. Nellist, Paul R. Shearing, Elvis Shoko, Weixin Song, Dominic Spencer Jolly, Christopher I. Thomas, Stephen J. Turrell, Mihkel Vestli, Charlotte K. Williams, Yundong Zhou, and Peter G. Bruce. 2020 roadmap on solid-state batteries. *JPhys Energy*, 2(3), 7 2020. ISSN 25157655. doi: 10.1088/2515-7655/ab95f4.

[80] Pekka Peljo and Hubert H. Girault. Electrochemical potential window of battery electrolytes: The HOMO-LUMO misconception. *Energy and Environmental Science*, 11(9):2306–2309, 9 2018. ISSN 17545706. doi: 10.1039/c8ee01286e.

[81] E. Quartarone, T. Eisenmann, M. Kuenzel, C. Tealdi, A. G. Marrani, S. Brutti, D. Callegari, and S. Passerini. Towards Advanced Sodium-Ion Batteries: Green, Low-Cost and High-Capacity Anode Compartment Encompassing Phosphorus/Carbon Nanocomposite as the Active Material and Aluminum as the Current Collector. *Journal of The Electrochemical Society*, 167(8):080509, 4 2020. ISSN 19457111. doi: 10.1149/1945-7111/ab856e.

[82] William D. Richards, Lincoln J. Miara, Yan Wang, Jae Chul Kim, and Gerbrand

Ceder. Interface Stability in Solid-State Batteries. *Chemistry of Materials*, 28(1): 266–273, 1 2016. ISSN 15205002. doi: 10.1021/acs.chemmater.5b04082.

[83] David W. Richerson. *Modern Ceramic Engineering*. CRC Press, Boca Raton, 3rd edition, 2006.

[84] Helen K Roobottom, H. Donald B. Jenkins, Jack Passmore, and Leslie Glasser. Thermochemical Radii of Complex Ions. *Journal of Chemical Education* •, 76(11): 1570–1573, 1999. URL `https://pubs.acs.org/sharingguidelines`.

[85] Horst Sabrowsky, Karin Paszkowski, Dagmar Reddig, and Petra Vogt. Na3OCl and Na3OBr, the First Alkali Metal Chalcogenide Halides. *Z. Naturforsch*, 43: 238–239, 1988.

[86] Tammo K. Schwietert, Violetta A. Arszelewska, Chao Wang, Chuang Yu, Alexandros Vasileiadis, Niek J.J. de Klerk, Jart Hageman, Thomas Hupfer, Ingo Kerkamm, Yaolin Xu, Eveline van der Maas, Erik M. Kelder, Swapna Ganapathy, and Marnix Wagemaker. Clarifying the relationship between redox activity and electrochemical stability in solid electrolytes. *Nature Materials*, 19(4):428–435, 4 2020. ISSN 14764660. doi: 10.1038/s41563-019-0576-0.

[87] R D Shannon. Revised Effective Ionic Radii and Systematic Studies of Interatomie Distances in Halides and Chaleogenides. Technical report, 1976.

[88] Yusuke Shimoda, Yukiko Matsui, Takeshi Tonoya, and Masashi Ishikawa. Potassium Bis(fluorosulfonyl)imide Is an Effective Additive for Improving Anode Cyclability in Sulfolane-Based Electrolytes for Li-S Batteries. *ACS Applied Energy Materials*, 2023. ISSN 25740962. doi: 10.1021/acsaem.3c01513.

[89] Derrick M. Smith, Bin Dong, Russell W. Marron, Michael J. Birnkrant, Yossef A. Elabd, Lalgudi V. Natarajan, Vincent P. Tondiglia, Timothy J. Bunning, and Christopher Y. Li. Tuning ion conducting pathways using holographic polymerization. *Nano Letters*, 12(1):310–314, 1 2012. ISSN 15306984. doi: 10.1021/nl203599y.

[90] Jeffrey G. Smith and Donald J. Siegel. Low-temperature paddlewheel effect in glassy solid electrolytes. *Nature Communications*, 11(1), 12 2020. ISSN 20411723. doi: 10.1038/s41467-020-15245-5.

[91] Shufeng Song, Yongmin Wu, Weiping Tang, Fan Deng, Jianyao Yao, Zongwen Liu, Rongjie Hu, Alamusi, Zhaoyin Wen, Li Lu, and Ning Hu. Composite Solid Polymer Electrolyte with Garnet Nanosheets in Poly(ethylene oxide). *ACS Sustainable Chemistry and Engineering*, 7(7):7163–7170, 4 2019. ISSN 21680485. doi: 10.1021/acssuschemeng.9b00143.

[92] L A Stanciu, V Y Kodash, and J R Groza. Effects of Heating Rate on Densification and Grain Growth during Field-Assisted Sintering of Alpha-Al2O3 and MoSi2 Powders. *Metallurgical and Materials Transaction A*, 32A:2633–2638, 2001.

[93] Bing Sun, Peng Li, Jinqiang Zhang, Dan Wang, Paul Munroe, Chengyin Wang, Peter H L Notten, and Guoxiu Wang. Dendrite-Free Sodium-Metal Anodes for High-Energy Sodium-Metal Batteries. *Adv. Mater.*, 30(29):1801334, 5 2018. ISSN 1521-4095 (Electronic). doi: 10.1002/adma.201801334.

[94] Hao Sun, Guanzhou Zhu, Xintong Xu, Meng Liao, Yuan Yao Li, Michael Angell, Meng Gu, Yuanmin Zhu, Wei Hsuan Hung, Jiachen Li, Yun Kuang, Yongtao Meng,

Meng Chang Lin, Huisheng Peng, and Hongjie Dai. A safe and non-flammable sodium metal battery based on an ionic liquid electrolyte. *Nature Communications*, 10(1), 12 2019. ISSN 20411723. doi: 10.1038/s41467-019-11102-2.

[95] Yulong Sun, Yuechao Wang, Xinmiao Liang, Yuanhua Xia, Linfeng Peng, Huanhuan Jia, Hanxiao Li, Liangfei Bai, Jiwen Feng, Hong Jiang, and Jia Xie. Rotational Cluster Anion Enabling Superionic Conductivity in Sodium-Rich Antiperovskite Na3OBH4. *J. Am. Chem. Soc.*, 141(14):5640–5644, 2019. ISSN 15205126. doi: 10.1021/jacs.9b01746.

[96] J.-M Tarascon and M Armand. Issues and challenges facing rechargeable lithium batteries. *Nature*, 414:359–367, 2001. URL `www.nature.com`.

[97] Yaosen Tian, Tan Shi, William D. Richards, Juchuan Li, Jae Chul Kim, Shou Hang Bo, and Gerbrand Ceder. Compatibility issues between electrodes and electrolytes in solid-state batteries. *Energy and Environmental Science*, 10(5):1150–1166, 2017. ISSN 17545706. doi: 10.1039/c7ee00534b.

[98] W. Travis, E. N.K. Glover, H. Bronstein, D. O. Scanlon, and R. G. Palgrave. On the application of the tolerance factor to inorganic and hybrid halide perovskites: A revised system. *Chemical Science*, 7(7):4548–4556, 2016. ISSN 20416539. doi: 10.1039/c5sc04845a.

[99] Ping Chun Tsai, Sunil Mair, Jeffrey Smith, David M. Halat, Po Hsiu Chien, Kwangnam Kim, Duhan Zhang, Yiliang Li, Liang Yin, Jue Liu, Saul H. Lapidus, Jeffrey A. Reimer, Nitash P. Balsara, Donald J. Siegel, and Yet Ming Chiang. Double Paddle-Wheel Enhanced Sodium Ion Conduction in an Antiperovskite Solid

Electrolyte. *Adv. Energy Mater.*, 13(7):2203284, 2 2023. ISSN 16146840. doi: 10.1002/aenm.202203284.

[100] Stephen J. Turrell, Hyeon Jeong Lee, Marco Siniscalchi, Sudarshan Narayanan, Mauro Pasta, Susannah C. Speller, and Chris R.M. Grovenor. Fabrication of thin solid electrolytes containing a small volume of an Li3OCl-type antiperovskite phase by RF magnetron sputtering. *Materials Advances*, 3(24):8995–9008, 10 2022. ISSN 26335409. doi: 10.1039/d2ma00971d.

[101] Chuanlong Wang, Huan Wang, Edward Matios, Xiaofei Hu, and Weiyang Li. A Chemically Engineered Porous Copper Matrix with Cylindrical Core–Shell Skeleton as a Stable Host for Metallic Sodium Anodes. *Adv. Funct. Mater.*, 28(30): 1802282, 2018. ISSN 16163028. doi: 10.1002/adfm.201802282.

[102] Fei Wang, Ping-chun Tsai, Yiliang Li, Stephanie L Eiler, Seoung-Bum Son, and Yet-Ming Chiang. (Invited) Synthesis, Characterization, and Investigation of Non-Arrhenius Behavior in Anti-Perovskite Ion Conductors. *ECS Meeting Abstracts*, MA2019-02(2):70, 9 2019. doi: 10.1149/MA2019-02/2/70. URL `https://dx.doi.org/10.1149/MA2019-02/2/70`.

[103] Fei Wang, Yiliang Li, Ping-Chun Tsai, Liang Yin, Hayden Evens, Kwangnam Kim, Saul H Lapidus, Donald J Siegel, and Yet-Ming Chiang. Understanding the Structural Disorder Related to Ionic Conductivity Enhancement in Anti-Perovskite Ion Conductors. *ECS Meeting Abstracts*, MA2020-02(5):967, 11 2020. doi: 10.1149/MA2020-025967mtgabs. URL `https://dx.doi.org/10.1149/MA2020-025967mtgabs`.

[104] Jianhui Wang, Yuki Yamada, Keitaro Sodeyama, Eriko Watanabe, Koji Takada, Yoshitaka Tateyama, and Atsuo Yamada. Fire-extinguishing organic electrolytes for safe batteries. *Nature Energy*, 3(1):22–29, 1 2018. ISSN 20587546. doi: 10.1038/s41560-017-0033-8.

[105] S Wang, B Peng, J Lu, Y Jie, X Li, Y Pan, Y Han, R Cao, D Xu, and S Jiao. Recent Progress in Rechargeable Sodium Metal Batteries: A Review. *Chem. Eur. J.*, 29 (3):e2022023, 1 2023.

[106] Yonggang Wang, Qingfei Wang, Zhenpu Liu, Zhengyang Zhou, Shuai Li, Jinlong Zhu, Ruqiang Zou, Yingxia Wang, Jianhua Lin, and Yusheng Zhao. Structural manipulation approaches towards enhanced sodium ionic conductivity in Na-rich antiperovskites. *J. Power Sources*, 293:735–740, 2015. ISSN 03787753. doi: 10.1016/j.jpowsour.2015.06.002. URL `http://dx.doi.org/10.1016/j.jpowsour.2015.06.002`.

[107] Yonggang Wang, Ting Wen, Changyong Park, Curtis Kenney-Benson, Michael Pravica, Wenge Yang, and Yusheng Zhao. Robust high pressure stability and negative thermal expansion in sodium-rich antiperovskites Na3OBr and Na4OI2. *Journal of Applied Physics*, 119(2), 1 2016. ISSN 10897550. doi: 10.1063/1.4940020.

[108] Regina Wortmann, Stephan Sitta, and Horst Sabrowsky. Li7O2Br3 - A Further Structure Variant of the New Alkali Metal Chalcogenide Halide Perovskites. *Z. Naturforsch*, 44b:1348–1350, 1989.

[109] Musheng Wu, Bo Xu, Xueling Lei, Kelvin Huang, and Chuying Ouyang. Bulk properties and transport mechanisms of a solid state antiperovskite Li-ion con-

ductor Li3OCl: Insights from first principles calculations. *Journal of Materials Chemistry A*, 6(3):1150–1160, 2018. ISSN 20507496. doi: 10.1039/c7ta08780b.

[110] Kang Xu. A Long Journey of Lithium: From the Big Bang to Our Smartphones. *Energy and Environmental Materials*, 2(4):229–233, 12 2019. ISSN 25750356. doi: 10.1002/eem2.12057.

[111] Wu Xu, Jiulin Wang, Fei Ding, Xilin Chen, Eduard Nasybulin, Yaohui Zhang, and Ji Guang Zhang. Lithium metal anodes for rechargeable batteries. *Energy and Environmental Science*, 7(2):513–537, 2014. ISSN 17545706. doi: 10.1039/c3ee40795k.

[112] Chao Yang, Sen Xin, Liqiang Mai, and Ya You. Materials Design for High-Safety Sodium-Ion Battery. *Adv. Energy Mater.*, 11(2):2000974, 2021. ISSN 16146840. doi: 10.1002/aenm.202000974.

[113] L. Yang, M. M. Furczon, A. Xiao, B. L. Lucht, Z. Zhang, and D. P. Abraham. Effect of impurities and moisture on lithium bisoxalatoborate (LiBOB) electrolyte performance in lithium-ion cells. *Journal of Power Sources*, 195(6):1698–1705, 3 2010. ISSN 03787753. doi: 10.1016/j.jpowsour.2009.09.056.

[114] Zhenguo Yang, Jianlu Zhang, Michael C.W. Kintner-Meyer, Xiaochuan Lu, Daiwon Choi, John P. Lemmon, and Jun Liu. Electrochemical energy storage for green grid. *Chemical Reviews*, 111(5):3577–3613, 5 2011. ISSN 00092665. doi: 10.1021/cr100290v.

[115] Liang Yin, Megan Murphy, Kwangnam Kim, Linhua Hu, Jordi Cabana, Donald J. Siegel, and Saul H. Lapidus. Synthesis of Antiperovskite Solid Electrolytes: Com-

paring Li3SI, Na3SI, and Ag3SI. *Inorganic Chemistry*, 59(16):11244–11247, 8 2020. ISSN 1520510X. doi: 10.1021/acs.inorgchem.0c01705.

[116] Tianwei Yu, Xiaofei Yang, Rong Yang, Xiangtao Bai, Guofeng Xu, Shangqian Zhao, Yi Duan, Yanlong Wu, and Jiantao Wang. Progress and perspectives on typical inorganic solid-state electrolytes. *Journal of Alloys and Compounds*, 885, 12 2021. ISSN 09258388. doi: 10.1016/j.jallcom.2021.161013.

[117] Xingwen Yu, Leigang Xue, John B. Goodenough, and Arumugam Manthiram. Ambient-Temperature All-Solid-State Sodium Batteries with a Laminated Composite Electrolyte. *Advanced Functional Materials*, 31(2), 2021. ISSN 16163028. doi: 10.1002/adfm.202002144.

[118] Jianzhong Zhang, Jiantao Han, Jinlong Zhu, Zhijun Lin, Maria H. Braga, Luke L. Daemen, Liping Wang, and Yusheng Zhao. High pressure-high temperature synthesis of lithium-rich Li3O(Cl, Br) and Li3 - XCax/2OCl anti-perovskite halides. *Inorganic Chemistry Communications*, 48:140–143, 2014. ISSN 13877003. doi: 10.1016/j.inoche.2014.08.036.

[119] Jianzhong Zhang, Liping Wang, Jinlong Zhu, and Yusheng Zhao. Structural disorder, sublattice melting, and thermo-elastic properties of anti-perovskite Li3OBr under high pressure and temperature. *Appl. Phys. Lett.*, 117(8):081904, 8 2020. ISSN 00036951. doi: 10.1063/5.0018714.

[120] Yi Zhang, Yusheng Zhao, and Changfeng Chen. Ab initio study of the stabilities of and mechanism of superionic transport in lithium-rich antiperovskites. *Phys. Rev. B*, 87(13):134303, 4 2013. ISSN 10980121. doi: 10.1103/PhysRevB.87.134303.

[121] Zhizhen Zhang, Qiangqiang Zhang, Cheng Ren, Fei Luo, Qiang Ma, Yong Sheng Hu, Zhibin Zhou, Hong Li, Xuejie Huang, and Liquan Chen. A ceramic/polymer composite solid electrolyte for sodium batteries. *Journal of Materials Chemistry A*, 4(41):15823–15828, 2016. ISSN 20507496. doi: 10.1039/c6ta07590h.

[122] Zhizhen Zhang, Hui Li, Kavish Kaup, Laidong Zhou, Pierre Nicholas Roy, and Linda F. Nazar. Targeting Superionic Conductivity by Turning on Anion Rotation at Room Temperature in Fast Ion Conductors. *Matter*, 2(6):1667–1684, 6 2020. ISSN 25902385. doi: 10.1016/j.matt.2020.04.027.

[123] Chenglong Zhao, Lilu Liu, Xingguo Qi, Yaxiang Lu, Feixiang Wu, Junmei Zhao, Yan Yu, Yong Sheng Hu, and Liquan Chen. Solid-State Sodium Batteries. *Advanced Energy Materials*, 8(17), 6 2018. ISSN 16146840. doi: 10.1002/aenm.201703012.

[124] Qing Zhao, Sanjuna Stalin, Chen Zi Zhao, and Lynden A. Archer. Designing solid-state electrolytes for safe, energy-dense batteries. *Nature Reviews Materials*, 5(3):229–252, 3 2020. ISSN 20588437. doi: 10.1038/s41578-019-0165-5.

[125] Yanzhang Zhao, Zhanying Liu, Jiaxin Xu, Tengfei Zhang, Fang Zhang, and Xiaogang Zhang. Synthesis and characterization of a new perovskite-type solid-state electrolyte of Na1/3La1/3Sr1/3ZrO3 for all-solid-state sodium-ion batteries. *Journal of Alloys and Compounds*, 783:219–225, 4 2019. ISSN 09258388. doi: 10.1016/j.jallcom.2018.12.289.

[126] Yusheng Zhao and Luke L. Daemen. Superionic conductivity in lithium-rich anti-

perovskites. *Journal of the American Chemical Society*, 134(36):15042–15047, 9 2012. ISSN 00027863. doi: 10.1021/ja305709z.

[127] Jingfeng Zheng, Hong Fang, Longlong Fan, Yang Ren, Puru Jena, and Yiying Wu. Antiperovskite K3OI for K-Ion Solid State Electrolyte. *J. Phys. Chem. Lett.*, 12 (30):7120–7126, 2021. ISSN 19487185. doi: 10.1021/acs.jpclett.1c01807.

[128] Jingfeng Zheng, Brian Perry, and Yiying Wu. Antiperovskite Superionic Conductors: A Critical Review. *ACS Mater. Au*, 1(2):92–106, 2021. ISSN 26942461. doi: 10.1021/acsmaterialsau.1c00026.

[129] Pan Zhou, Wenhui Hou, Yingchun Xia, Yu Ou, Hang Yu Zhou, Weili Zhang, Yang Lu, Xuan Song, Fengxiang Liu, Qingbin Cao, Hao Liu, Shuaishuai Yan, and Kai Liu. Tuning and Balancing the Donor Number of Lithium Salts and Solvents for High-Performance Li Metal Anode. *ACS nano*, 17(17):17169–17179, 9 2023. ISSN 1936086X. doi: 10.1021/acsnano.3c05016.

[130] Jinlong Zhu, Shuai Li, Yi Zhang, John W Howard, Xujie Lü, Yutao Li, Yonggang Wang, Ravhi S Kumar, Liping Wang, and Yusheng Zhao. Enhanced ionic conductivity with Li7O2Br3 phase in Li3OBr anti-perovskite solid electrolyte. *Appl. Phys. Lett.*, 109(10):101904, 9 2016. ISSN 0003-6951. doi: 10.1063/1.4962437. URL `https://doi.org/10.1063/1.4962437`.

[131] E. Zintl and W. Morawietz. Orthosalze von Sauerstoffsäuren. *Zeitschrift für anorganische und allgemeine Chemie*, 236(1):372–410, 1938. ISSN 15213749. doi: 10.1002/zaac.19382360134.

2 | Experimental Techniques

2.1 Synthetic Techniques

Due to the air sensitivity of the precursors and products involved in this thesis, all experiments were done in Argon-filled gloveboxes (MBraun, $H_2O < 0.1$ ppm, $O_2 < 0.1$ ppm).

2.1.1 Solid-state Synthesis

The most common synthesis method employed to make Na_3OB (B = Cl, Br, or BH_4) is the solid-state route. Solid precursor materials (typically oxides, halides, etc.) are mixed together and then heated at high temperature; this process is often called *shake-and-bake* [13]. Due to the slow reaction kinetics between solids, the precursor materials are intimately mixed by ball-milling to reduce the length scales over which the atoms need to diffuse to react together.

The mixture is then loaded into an alumina boat and heated in a muffle furnace to a relatively low temperature, below $500\,^{\circ}\mathrm{C}$, for a prolonged time period (5 - 25 hours) to form pure, crystalline phases. This is necessary to decompose the precursor compounds and drive the reaction to completion. The samples were left inside the well-insulated furnace to cool down to room temperature (RT) naturally.

2.1.2 Calendering

Sodium oxide is one of the precursors for Na_3OB (B = Cl, Br, or BH_4) syntheses. All commercially available Na_2O reagents contain a significant amount of impurities, mainly

sodium peroxide Na_2O_2 [7, 44, 32]. One way to synthesise highly pure Na_2O is via a solid-state reaction of Na metal with NaOH [6, 54]. This reaction is very slow and energy-consuming, as it requires prolonged heating and an active vacuum. Increasing the Na metal's available surface area for reaction can help to speed up and ensure a complete reaction between the two precursors. Na metal was washed with hexane and inserted into a pouch cell, to protect it from impurities during calendering. Then it was passed between two metal rollers, the space between which was reduced over time until the final thickness of the Na metal became $\approx 250\,\mu\mathrm{m}$. The thin Na metal sheet was then cut into smaller pieces and mixed with NaOH powder using mortar and pestle. To produce pure Na_2O, the mixture was plcaed in an alumina boat and heated to $300\,^{\circ}\mathrm{C}$ in a glass vacuum oven (Buchi) for 14 hours. Following this, the mixture was thoroughly mixed with a mortar and pestle and subjected to the same heating regime. This procedure was repeated five times until all the reactants had undergone complete reaction.

2.1.3 Ball-milling Synthesis

Ball-milling is a mechanical technique that is commonly used to reduce particle size or thoroughly mix dry powders. The ball milling process involves a jar made of ZrO_2 along with balls of different sizes made from the same material. Solid precursors are added and sealed in the jar and then rotated at a high speed by a milling machine. During mixing, the balls collide with the walls of the jar and with each other with high kinetic energy, generating a large amount of highly localised heat that increases the temperature of the particles. Additionally, collisions with the particles generate large mechanical stresses which cause abrasion, shearing, and intimate mixing of the precursors. Ball-milling solid

precursors at sufficiently high speeds can lead to the formation of metastable phases, which would otherwise require very high temperature and/or high-pressure equipment to make [43, 8]. This technique is often called 'mechanochemical synthesis' and it has been attracting interest due to its low cost and capability to achieve highly pure final products [6, 51].

2.1.4 Liquid State Synthesis

Different from Na_3OB, $Li_2OHCl_{0.9}Br_{0.1}$ are mostly synthesised by mixing stoichiometric amounts of precursors followed by a melting and solidification process. This is due to the use of a hydroxide precursor instead of oxide. The ratio of the precursors is as follows:

$$\mathrm{LiOH} + 0.9\,\mathrm{LiCl} + 0.1\,\mathrm{LiBr} \longrightarrow \mathrm{Li_2OHCl_{0.9}Br_{0.1}} \tag{2.1}$$

Since melting is involved, ball milling is not necessary for the synthesis. At the synthesis temperature of $350\,^{\circ}\mathrm{C}$, the mixture was completely molten. Mixing was done with mortar and pestle for $\approx$ 10 minutes.

2.2 Structural Characterisation

2.2.1 Powder X-ray Diffraction

Powder X-ray diffraction is a powerful technique that can be used for phase or polymorph identification, cell parameter determination, quantitative analysis, or even full crystal structure analysis using the Rietveld refinement method [16]. When electromagnetic radi-

ation with a wavelength comparable to interatomic separations is incident on a crystalline sample, each atom acts as a source of scattered radiation and the destructive/constructive interference between the scattered waves leads to diffraction, as seen in Figure 2.1. A crystalline sample has a highly ordered array of atoms and so the angle at which the scattering reflects off of planes of atoms in the structure is identical to the angle of incidence. Each of these planes can be described by 3 values *h*, *k*, and *l*, known as the Miller indices. The constructive interference is described by Bragg's law [10]:

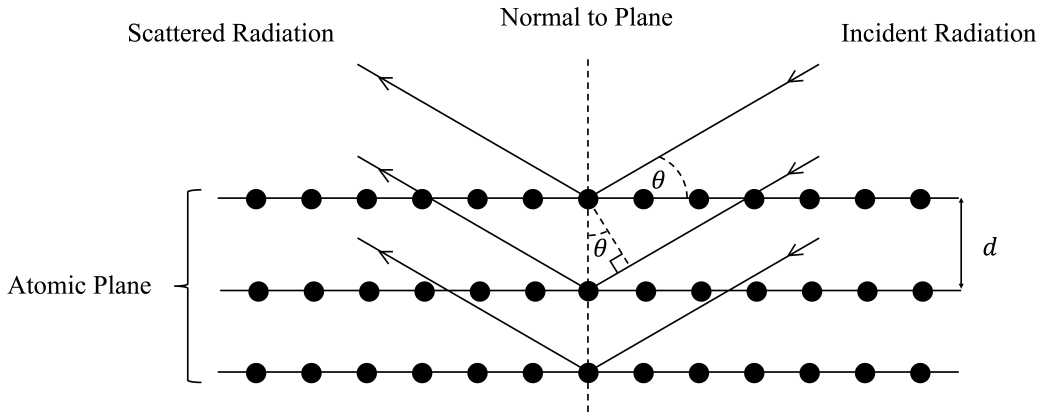

Figure 2.1: Schematic showing how Bragg's Law relates the d spacing between atomic planes to the wavelength of the radiation and the diffraction angle.

$$n\lambda = 2d_{hkl}sin(\theta) \tag{2.2}$$

where n is an integer, λ is the wavelength of radiation, d_{hkl} is the perpendicular distance between atom planes of defined Miller indices hkl, and θ is the angle between the incident beam and the hkl plane. The number and position of peaks in the diffraction pattern are determined by the space group and unit cell parameters of the crystal, which sets the interplanar spacing, d_{hkl}, of the planes [42]. The absolute intensity of each of hkl reflection, I_{hkl}, is determined by the identity and positions of the atoms inside the unit cell via the

structure factor F_{hkl} [20].

$$I_{hkl} \propto |F_{hkl}|^2 \tag{2.3}$$

The structure factor is defined as:

$$F_{hkl} = \sum_{j=1}^{N} f_j e^{[2\pi i(hx_j + ky_j + lz_j)]} \tag{2.4}$$

where x_j, y_j, and z_j are the coordinates of the jth atom in the unit cell and f_j is the scattering factor or form factor of the jth atom. This factor is determined by the scattering amplitude of an atom. It increases with the electron density around the atom [20].

Four different X-ray diffractometers were used in this work: two laboratory instruments (Rigaku MiniFlex and Rigaku SmartLab SE - 3kW) and two synchrotron beamlines (I15-1 and I11 at Diamond Light Source). For laboratory instruments, X-rays are generated by accelerating electrons at a metal target, in this case, Cu. This triggers the emission of X-rays at a number of wavelengths characteristic of the metal. The X-ray light must then be monochromated to select the most intense wavelength of radiation, Cu $K_{\alpha 1}$ (1.5406 Å). A nickel monochromator can be used to selectively absorb Cu K_{β} radiation and a germanium monochromator can be added to remove the Cu $K_{\alpha 2}$ radiation [30]. The source, sample holder and X-ray detector are precisely positioned in a circular geometry. The source and detector are on the circumference and the sample is at the centre of the diffractometer axis.

Most powder diffractometers use Bragg-Brentano parafocusing geometry, which demands

precise alignment and carefully prepared samples . In this configuration, the incident angle (ω) between the X-ray source and the sample is always half of the detector angle (2θ). Two possible scan modes exist with this geometry [3]. Firstly, θ-θ, where the X-ray tube remains fixed, the sample rotates at a rate of $\theta\mathrm{min}^{-1}$, and the detector operates at $2\theta\mathrm{min}^{-1}$. Secondly, θ-2θ, where the sample remains stationary, and the tube and detector rotate at the same rate at $\theta\mathrm{min}^{-1}$ [45]. Another geometry is the parallel-beam, which has no restrictions on XRD configuration like in the Bragg-Brentano case. This allows for a broader range of sample shapes and sizes. In this thesis, the former geometry was employed. Data were collected with a step size of 0.02°. To ensure correct sample alignment, the powder sample surface was leveled with the top of the sample holder using a glass slide.

Synchrotron radiation offers better peak resolution due to the use of a highly collimated beam of X-rays with tunable wavelength. This reduces instrumental peak broadening and enhances signal-to-noise ratio. The synchrotron consists of a ring-shaped vacuum-filled pipe surrounded by a complex array of magnets. Electrons are injected into the ring at high speed. The magnets induce an oscillating motion to the high-energy beam of electrons which triggers the electrons to emit X-ray radiation as they change direction. Synchrotron X-rays are produced over a wide variety of energies. Therefore, the beam that comes directly off the synchrotron is often called *white light*. At each beamline, the X-rays are monochromated with optics to the desired wavelength. Wavelengths of $0.161\,669$ Å (Diamond Light Source I11 beamline) and $0.825\,318(3)$ Å (Diamond Light Source I15-1 beamline) were used in this thesis. In contrast to lab instruments, measurements are usually carried out in transmission mode (Debye-Scherrer) where the beam is

stationary and the detector is scanned in 2θ. Sample preparation for synchrotron experiments was completely different from that for the in-house measurements. Powders were ground with mortar and pestle for 10 minutes to reduce the crystallite's size and ensure that a statistically large number of them were exposed to the beam. Each powder sample was then inserted into a $5\,\mathrm{mm}$ diameter borosilicate capillary and sealed with plasticine and super glue. To make sure that the powders were closely packed, the capillary was sonicated inside the glovebox with the help of a sonic toothbrush.

2.2.2 Rietveld Refinement

Rietveld refinement is a structural refinement methodology using the whole pattern developed to extract structural information from powder diffraction data, including a phase transition [39]. A starting model structure is essential for Rietveld refinement in order to produce a reasonable initial calculated powder diffraction pattern. There are various methods available for rapidly testing computer-generated guessed structures against experimental data to find a reasonable starting model. Otherwise, an approximate structural model derived from a related compound can be used. In this thesis, the latter was used. Common parameters refined when fitting the data include structural parameters (the sample unit-cell parameters, atomic site occupancies, atomic displacement parameters, and fractional atomic coordinates), parameters describing the peak shape, parameters describing the instrument calibration (e.g. zero-point offset), and parameters describing the background between the Bragg peaks. The refinement parameters are then systematically varied to improve the fit until the match is satisfactory. In this thesis, all Rietveld refinements were carried out using the TOPAS-Academic software.[12].

There are a number of ways of determining the quality of the refinement or the goodness of fit (GOF or χ) between the model and the data. The weighted profile factor, R_{wp}, is calculated from the square of the difference between the observed and computed peak intensities summed and weighted by peak intensity. This value should tend to be a low value. The expected R factor, R_{exp}, is the best possible value for R_{wp} given the degrees of freedom allowed in the refinement. Finally, χ is the ratio between R_{wp} and R_{exp} [16].

$$R_{wp} = \left(\frac{\sum_{i=1}^{N} w_i (y_{obs,i} - y_{calc,i})^2}{\sum_{i=1}^{N} w_i y_{obs,i}^2}\right)^{1/2} \tag{2.5}$$

$$R_{exp} = \left(\frac{N - P}{\sum_{i=1}^{N} w_i y_{obs,i}^2}\right)^{1/2} \tag{2.6}$$

$$\chi = \frac{R_{wp}}{R_{exp}} \tag{2.7}$$

where y_i is the peak intensity, w_i is the weighting, N is the number of data points, and P is the number of varied parameters.

2.2.3 Differential Scanning Calorimetry

Differential scanning calorimetry is a thermal analysis technique in which the heat flow into or out of a sample with known mass is measured as a function of temperature or time. This allows the detection of transitions such as phase changes, melts, and glass transitions. DSC measurements in this thesis were done using two instruments: Netzsch TGA-MS and TA Instruments DSC25. The first one was used to study the thermal properties of the

synthesis precursors and that of the $Li_2OHCl_{0.9}Br_{0.1}$. A small amount of sample (5 - 15 mg) was placed on an alumina boat with a lid and placed into the sample stage. The lid was used to minimise the exposure of the sample to air. Argon shower was also turned on during the sample loading for the same reason. A second crucible without a sample was used as a reference. A hermetically sealed aluminium boat could not be used with the first instrument as they are not compatible. Moreover, in the literature it has been argued that highly corrosive $Li_2OHCl_{0.9}Br_{0.1}$ melt may react with aluminium and accidentally dope it with Al^{3+} cations [53]. The second instrument was used to study the thermal properties of the Na-antiperovskite samples (Na_3OBr, Na_3OCl, and Na_3OBH_4). Both this instrument and Na-antiperovskites are compatible with aluminium pans, thus a hermetically sealed aluminium pan was used to ensure air tightness.

2.2.4 Scanning Electron Microscopy and Focused Ion Beam Milling

Scanning electron microscopy (SEM) is one of the common methods for imaging the microstructure and morphology of the materials. In this work, SEM was used to study the particle size and the surface and cross-sectional morphology of antiperovskite pellets. SEM was chosen instead of optical microscopy because the resolution of optical microscopes is limited by the wavelength of light used due to the diffraction limit [50]. Therefore, in order to resolve sub-micron features, which we are interested in, SEM is necessary. Additionally, SEM offers a higher depth of field. This allows clearer imaging of surface topography and a range of detectors that can be used to access different information about the sample including chemical composition.

SEM overcomes the diffraction limit through the use of high energy beam electrons which

have significantly shorter wavelengths than that of visible light [15]. An electron beam is generated by a thermionic or field emission source. This work only uses SEM with field emission sources because these sources are much brighter and give fewer distortions, leading to better image resolution. The electron beam is focused and scanned across the sample using electromagnetic lenses and coils. The beam penetrates the sample and interacts with its atoms both elastically and inelastically, generating a variety of signals that give valuable information about the samples. Two common signals used for imaging are the secondary electron signal and backscattered electron signal [1]. Low-energy secondary electrons are emitted from inelastic collisions between the incident beam and sample electrons. These electrons originate from the surface of the sample (first few nanometers), thus the image contrast is determined primarily by the surface topography. On the other hand, backscattered electrons originate from the elastic scattering of incident beam electrons. The backscattered electrons travel from a much deeper sampling region. Therefore, they provide little information about the sample surface. In this thesis, SEM images were collected using the secondary electron signal only. On top of the images, energy dispersive X-ray analysis (EDX) was performed for elemental analysis. X-rays are generated when incident beam electrons eject electrons from the inner shells of the sample atoms. The subsequent replacement of these electrons by outer shell electrons releases energy in the form of X-rays. EDX is mostly used for qualitative and semi-quantitative analysis [45]. It is possible to perform quantification but the accuracy of these measurements depends on a number of instrumental and sample-related factors [45]. For example, a Li-antiperovskite sample contains light elements which produce low-intensity, low-energy X-ray signals. Lithium is difficult to detect using this technique since its characteristic X-rays are mostly

absorbed by instrument components, like the window, before they reach the detector. The detection of heavier elements can also be compromised when studying battery materials at low accelerating voltages, which are often employed to minimise charging.

Very clean cross-sections with minimal damage were required to study the effect of different processing routes on the microstructure of the pellets. A plasma focused ion beam (PFIB) was used to produce the cross-sections. The PFIB instrument used in this thesis was Thermo-Fisher Helios G4-CXe. It has both an SEM column with a field emission source and a focused ion column with a xenon ion (Xe^+) source in the same chamber. Each sample was mounted on conductive adhesive carbon tape (0.15 mm thickness, EM Sciences) and placed on dedicated SEM stubs. The stubs were then mounted on a transportable SEM stage inside the glovebox and sealed within an airtight Gatan iLoad sample transfer vessel. The stage was then transferred from the vessel into the SEM chamber via a load-lock setup.

2.2.5 Density Measurement

The relative density of the cold-pressed sample was determined by Archimedes' principle following the ISO18754 standard with Toluene as the immersing fluid [4]. This method allows us to account for the closed pores. It is appropriate for our pellets because the average pore size in our pellets is less than $600\,\mu\mathrm{m}$.

To get the relative density the mass was measured three times: dry in argon atmosphere (m_1), when fully immersed in toluene (m_2), and finally in air while still soaked in toluene (m_3). Full immersion in toluene was ensured via a vacuum method. Each pellet was placed in a pouch cell, evacuated to a pressure of less than $2.5\,\mathrm{kPa}$, and maintained for

$30\,\mathrm{min}$ to remove all the air from the open pores. The pellet was then introduced to the immersion liquid by cutting the pouch cells open inside the immersing liquid, where it was kept for an additional $30\,\mathrm{min}$. The relative density (ρ_R) was calculated with Eq. (2.8). Here, ρ_P is the pellet density, ρ_T is the theoretical density, and ρ_L is the density of toluene.

$$\rho_R = \frac{\rho_\mathrm{P}}{\rho_\mathrm{T}} = \frac{\frac{m_1}{(m_3 - m_2) \times \rho_\mathrm{L}}}{\rho_\mathrm{T}} \tag{2.8}$$

2.3 Chemical Characterisation

2.3.1 X-ray Photoelectron Spectroscopy

X-ray Photoelectron Spectroscopy (XPS) is a surface-sensitive analytical technique that measures the elemental composition of the surface of a material (1 - 10 nm) and determines the binding states of the elements [33]. XPS works based on the photoelectric effect that refers to the bombardment of the sample surface with soft X-rays (energies lower than $\approx$ 6 keV). As electrons in the sample absorb enough energy, they get ejected from the shell of the atoms and their kinetic energy and number are simultaneously measured by detectors. The difference between the photon energy and the sum of the electron kinetic energy and work function determines the core-level binding energy, as seen in the equation below:

$$E_{binding} = E_{photon} - (E_{kinetic} + \phi) \tag{2.9}$$

where ϕ is the work function which depends on both the spectrometer and the material

[17]. Therefore, it is often treated as an adjustable instrumental correction factor. The XPS used in this thesis was a Phi XPS VersaProbe III with an Al Kα X-ray source.

To study the stability of Na_3OB (B = Cl, Br, or BH_4) against sodium metal at RT, the solid electrolyte interphase (SEI) evolution was monitored by conducting in-situ Na deposition and simultaneously capturing photoemission spectra. Sodium metal foil (Sigma Aldrich) was calendered to $\approx 250\,\mu\mathrm{m}$ and mechanically cleaned by scraping. It was then fixed to an L-shaped target holder, as seen in Figure 2.2 by using double-sided adhesive tape. Na3OB (B = Cl, Br, or BH_4) pellets were cold-pressed and a copper mesh was pressed on top of them for calibration purposes. The samples were then mounted onto the holder with a conductive adhesive carbon tape and transferred into the XPS machine using an airtight transfer system.

The deposition rate was calibrated by sputtering Na metal onto the thin Cu mesh, which was pressed onto the antiperovskite pellets earlier. The rate was calculated using an adaptation of the Strohmeier equation for determining coating layer thicknesses using XPS peak intensities and Beer Lambert's law for correlating intensity attenuation of an electromagnetic wave to the thickness of the layer of propagation [31, 49].

$$t_{\mathrm{Na}} = -\lambda_{\mathrm{Cu}}^{\mathrm{Na}} \ln\left(\frac{I_{\mathrm{Cu}}^{\mathrm{Na}}}{I_{\mathrm{Cu}}}\right) \tag{2.10}$$

t_{Na} is the thickness of deposited Na film, $\lambda_{Cu}^{\mathrm{Na}}$ is the inelastic mean free path of Na at the kinetic energy for core-level photoemission from Cu, I_{Cu}^{Na} is the intensity of core-level spectra for Cu with a Na layer and I_{Cu} is the intensity of core-level spectra for an uncoated Cu substrate.

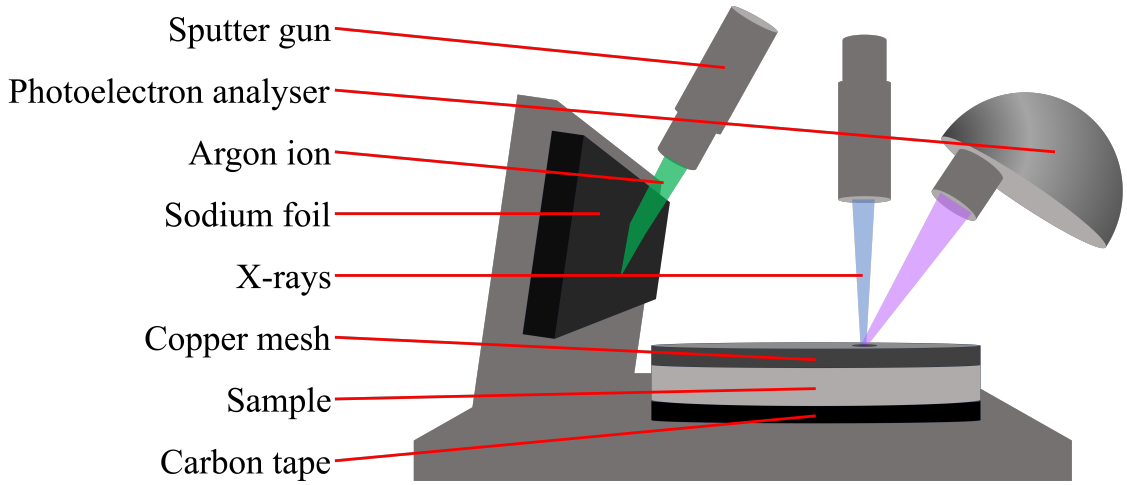

Figure 2.2: Schematic depicting the XPS in-situ Na metal deposition experiment setup. An argon ion beam is used to sputter sodium on the sample surface. After deposition, the reaction products at the interface are investigated using photoelectron spectroscopy.

2.3.2 Solid-state Nuclear Magnetic Resonance Spectroscopy

Solid-state nuclear magnetic resonance (NMR) is a spectroscopic technique that can be used to determine the chemical structure, 3D structure and dynamics of solids [38]. Transitions between nuclear spin energy levels give rise to the phenomenon in NMR. Today's NMR spectroscopy typically uses magnetic fields of 5 - 28 T, thus the transition frequencies lie in the radiofrequency regime of the electromagnetic spectrum [38].

The existence of nuclear spin was first introduced by Pauli in 1924 [22]. Nuclei of different elements differ in spin angular momentum. The proton ^{1}H has a spin quantum number, I, of $\frac{1}{2}$, as does the neutron. For nuclei other than ^{1}H, the spin angular momenta of the individual nucleons couple to make up the observed total. This is characterised by a quantum number, I, which can be a zero, a half-integral, or an integral. Nuclei with an odd mass number have half-integral spin. Nuclei with an even mass number and an even charge number, like ^{12}C, have zero spin. Finally, nuclei with an even mass number but

an odd charge have an integral spin [2]. Since NMR depends on the existence of nuclear spin, nuclei with zero spin are invisible in NMR. The transition between nuclear spin energy levels is governed by the Planck equation [37].

$$\Delta U = U_1 - U_2 = \hbar v \tag{2.11}$$

Where h is the Planck constant (6.62×10^{-34}) J s and v is the frequency. All NMR active nuclei are known to possess two intrinsic properties: charge and spin (I). A nuclear magnetic resonance relies on non-zero spin (i.e. angular momentum) being present. The spin originates from a nucleus having an inequality of neutrons and protons at its nucleus. It can be quantified by:

$$\mu = \gamma I \tag{2.12}$$

γ is the gyromagnetic (measured in $rads^{-1}T^{-1}$) ratio between the magnetic moment, μ. In a quantum state, angular momentum is present as h. This means nuclei with the given spin I can have $2I + 1$ different orientations, with the smallest possible $I = \frac{1}{2}$ as the difference between the spin up and down states is proportional to $\hbar$. In the absence of a magnetic field, the spin-up and spin-down states are degenerate [37]. When a nucleus is placed in a magnetic field, the ground state will split into different energy levels proportional to the strength of the magnetic field, also known as Zeeman splitting. The energy of this interaction is defined as the Zeeman Hamiltonian:

$$\hat{\mathcal{H}}_Z = -\gamma B_0 I_Z \tag{2.13}$$

where B_0 is the strength of the magnetic field (expressed in Tesla (T)). The strength of this interaction is defined by the precession frequency of the nucleus in the static magnetic field B_0:

$$\omega_0 = -\gamma B_0 \tag{2.14}$$

where ω_0 is the Larmor frequency given in terms of $rads^{-1}$. The magnetic field is necessary to break the degeneracy by a difference of ω_0. Each NMR active isotope's nucleus has a different Larmor frequency since each of their magnetic moments differ, allowing the NMR experiment to identify different isotopes [37].

The NMR transition frequencies are sensitive to the distribution of electrons around the nucleus that shields it from the applied magnetic field, as they produce local magnetic fields. The chemical shielding tensor, σ, is unique for different nuclei of a given isotope in a molecule. It depends on the orientation of the molecule with respect to the magnetic field and gives rise to slightly different frequencies, thus revealing the chemical structure of the sample [38, 40]. This thesis will use the chemical shift, δ_i, rather than the shielding tensor, σ. The chemical shift is the fractional difference between the frequency of a particular nucleus and a standard compound σ_{ref}. However, only the shielding can be measured quantum mechanically and calculated directly. Therefore, all calculations of shifts are taken by converting the shielding to the shift via a known standard, as seen in

the equation below [37].

$$\delta_i = \frac{(\sigma_{\mathrm{ref}} - \sigma_i)}{(1 - \sigma_{\mathrm{ref}})} \tag{2.15}$$

The shielding of the nucleus is anisotropic. It is orientation-dependent. In solids, chemical shift anisotropy (CSA) is very important. It affects every nucleus we studied in this thesis. In a single crystal, all molecules have the same orientation with respect to B_0. In single crystals with different orientations, different chemical shifts will be present. Chemically inequivalent positions in the same crystal will also exhibit different chemical shifts. Powder samples, like the ones we have in this thesis, are composed of millions of single crystallites, all with different orientations with respect to B_0. This generates shifts from all possible orientations and produces characteristic broad powder-pattern lineshapes [19].

Over two-thirds of the nuclei present in the periodic table, including ^{23}Na, have $I > \frac{1}{2}$, meaning they contain a non-spherical nucleus which produces electric quadrupole moments. When a quadrupole nucleus is placed in a magnetic field, two energy terms need to be considered: Zeeman and quadrupolar [37]. Whether the resulting form of spectroscopy is essentially NMR or nuclear quadrupole resonance (NQR) depends on the relative magnitude of these terms. In this thesis, high-field magnets were used for the measurements and therefore the Zeeman term predominates. This means that the magnetic field rather than the electric field determines the direction of the quantization. A quadrupole can be thought of as two dipoles. The NMR absorption lines of nuclei with $I > \frac{1}{2}$ are generally broad.

Magic angle spinning (MAS) is often used to eliminate the orientational dependence of

the NMR anisotropic interactions in solid samples. In MAS, the sample is rotated rapidly around an axis of 54.74° with respect to the static magnetic field [36, 19]. This results in averaging of the anisotropy of nuclear interaction, whose frequency depends on the orientation according to the second-order Legendre polynomial. To remove the broadening, in a powdered sample all the crystallites must assume this orientation simultaneously. Thus, the MAS frequency must be sufficiently rapid. If these conditions are met then the isotropic component is retained while anisotropic interactions are averaged to zero. At 'slow' MAS frequencies the sideband intensities mirror the static powder pattern. As the MAS frequency increases, only the isotropic centreband remains unchanged. Finally, at fast MAS frequencies, only the isotropic centreband is observed. The MAS frequencies are relative because they depend on the strength of the interaction.

2.4 Electrochemical Characterisation

2.4.1 Solid Electrolyte Pellet Preparation

Cold pressing (CP) is a method of compacting powdered materials into a solid homogeneous mass. It is often done before machining or pressureless sintering [24]. In this thesis, cold-pressing was done with a 5mm diameter evacuable pellet die from Specac, which is made out of hardened 440C stainless steel. This material was chosen as it is able to withstand the high pressure (370 MPa) applied in our experiments. In addition, the pressing surface was mirror-polished to produce the highest possible quality of the pressed sample.

Hot pressing (HP), often also referred to as pressure sintering, is a sintering technique

in which both heat and external pressure are applied simultaneously. The applied pressure accelerates densification by breaking agglomerates and rearranging particles at low temperatures, allowing for increased packing and smaller pore sizes [18]. In addition, external pressure does not promote the kinetics of grain growth [11]. For simple ceramics, HP is usually done by putting a green body or powder inside a mold, to which uniaxial pressure is then applied. An important consideration for an HP setup is the selection of material used for the die set. In this thesis, the pressure applied for cold pressing and hot pressing were the same, 370 MPa, while the temperature applied was $180\,^{\circ}\mathrm{C}$. Therefore, the material chosen for the die set was hardened stainless steel. HP is reported to be able to achieve near 100% density, with reduced need for sintering aid [28]. This is beneficial for antiperovskite pellet processing, as the absence of sintering aid, even those that can decompose after sintering, means that there is less risk for impurities that can alter the electrochemical property of the antiperovskites. In the case of sodium antiperovskites, a pressure of 370 MPa was applied during heating but released during cooling to prevent cracking. A gentle heating rate of $5\,^{\circ}\mathrm{C}/\mathrm{min}$ was applied to minimise the thermal gradient between the areas closer to the heating elements and the rest of the bulk due to instrument limitation.

Spark Plasma Sintering (SPS) is a sintering technique similar to hot pressing, in which pressure and temperature are applied simultaneously to the specimen during densification. What differentiates the two is the way heat is applied. In the SPS, heat is applied using low voltage direct currrent (DC) to promote Joule heating in conductive materials, or in conductive parts of the press. In addition, SPS benefits from the higher heating rate allowed by the Joule heating from the applied electric current. Zhang et al. success-

fully densified Al-doped garnet-type LLZO to 99.8%, denser than conventionally sintered LLZO, via SPS at $1150\,^{\circ}\mathrm{C}$ [52].

A commonly cited problem with SPS is the uneven thermal gradient. Areas closer to the electrode tend to heat up faster than the rest of the bulk, which might introduce thermal stress and cracks in the specimen. Due to the low temperature required for processing, this problem is worse for antiperovskites, leading to massive cracks. Even though SPS offers a much shorter processing time, we decided not to pursue it due to massive cracks, the large quantity of powders required per pellet, and the long polishing regime required to completely remove the graphite layer after sintering.

2.4.2 Solid-state Cell Assembly

The ionic conductivities of lithium and sodium solid electrolytes were measured using a solid-state cell. This cell was designed so that the pellet could be pressed directly into the cell and kept there for electrochemical impedance spectroscopy. During the measurements, a uniaxial stack pressure of 70 MPa was applied. The pressure was adjusted by setting the top screw using a torque wrench and the torque was calibrated using a load cell from Omega Engineering. The load cell converts into measurable electrical output.

The body of the cell is made of polyether ether ketone (PEEK), as it is electronically insulating, mechanically strong, and chemically resistant. The casing is made of aluminium and the plunger rods are made of standard stainless steel. Stainless steel was chosen as it is electronically conductive, mechanically strong, and chemically resistant. The cell set-up can be seen in the Figure 2.3.

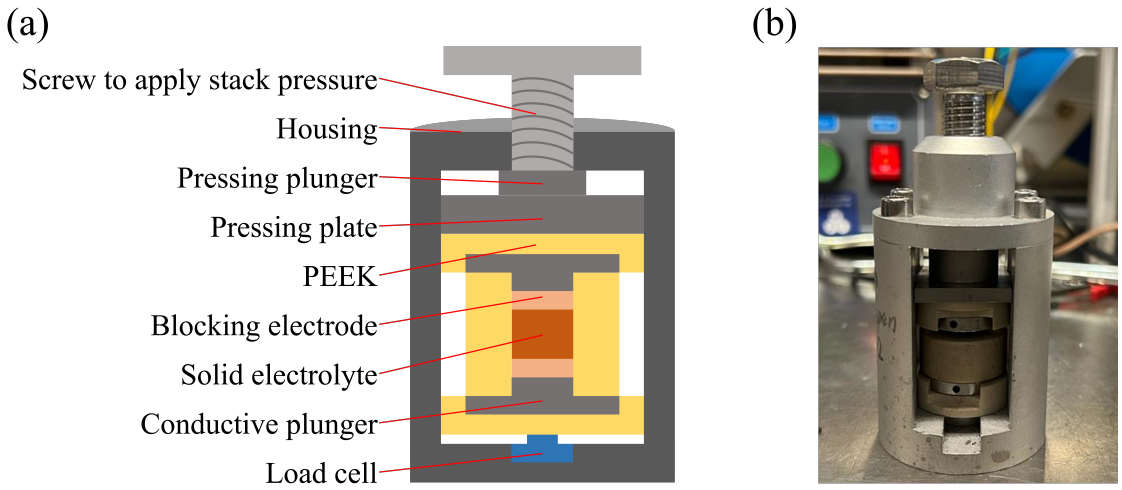

Figure 2.3: (a). Schematic depicting a cross-section of the solid-state cell setup for electrochemical testing. (b). Photograph of an assembled cell.

After the pellets were cold-pressed or hot-pressed, gold powder (Alfa Aesar, 0.8 - 1.5 µm) 'blocking' electrodes were pressed on both sides of the pellets. 'Blocking' electrodes can conduct electrons but not lithium or sodium ions.

2.4.3 Electrochemical Impedance Spectroscopy

Electrochemical impedance spectroscopy (EIS) is a technique commonly used for determining the impedance, and hence ionic conductivity, of solid electrolytes. It works based on the perturbation of an electrochemical system in equilibrium or in the steady state [27]. In EIS, the physical system is viewed in terms of analogous alternating current (AC) circuit components, principally resistors and capacitors. When an alternating voltage, E, is applied to the system as a function of time, t, an alternating current, I, response will be generated at the same frequency but a different phase [5]. When the amplitude of the applied voltage is low, it is assumed that the system behaves linearly. Therefore, the impedance, Z, is given by an expression that is analogous to Ohm's law for resistance in

DC circuits.

$$E(t) = E_0 \exp j\omega t \tag{2.16}$$

$$I(t) = I_0 \exp j[\omega t - \varphi] \tag{2.17}$$

$$Z(\varphi) = \frac{E(t)}{I(t)} = Z_0 \exp(j\varphi) = Z_0(cos\varphi + jsin\varphi) \tag{2.18}$$

Where E_0, I_0, and Z_0 are the amplitudes of the voltage, current, and impedance, respectively, ω is the angular frequency, j is the imaginary number $\sqrt{-1}$, and φ is the phase shift. Due to the phase difference between input and output signals, it is convenient to write the expressions for voltage, current, and impedance in complex form. Conventionally, -Im(Z) is plotted against Re(Z), and the diagram is known as the Nyquist plot. The change in the impedance of the system with frequency is the one that enables the properties of its elements to be determined. Different types of elements have different frequency responses. The frequency range of an EIS measurement is dictated by the available instrument limitations, the wiring of the electrochemical system with the instrument, and the stability of the electrochemical system over time. In this thesis, measurements were done between 3.5 MHz and 0.1 Hz.

EIS measurements should be designed to conform to the Kramers-Kronig relations, which are derived under the assumptions that the system under investigation is linear, stable and causal [9, 41]. The perturbation amplitude required to achieve a linear response with

an appropriate signal-to-noise ratio is generally determined experimentally for each system under study. In the case of an electrochemical system, the main difficulty is that the system must remain in a stationary state throughout the measurement. In this thesis, measurements were done at multiple temperatures. The total time required for each measurement is $7.5\,\mathrm{min}$. To fulfil the stationarity requirement, the samples were kept at target temperatures for 1 hour before each measurement. During this time, the heat is expected to have spread equally throughout the bulk of the samples.

An electrochemical system can be modelled using a combination of the fundamental AC circuit components, either in a series or a parallel configuration, also called an equivalent circuit. The relationships between the impedances of the fundamental equivalent circuit components: a resistor (R) and a capacitor (C) - and angular frequency (ω) are given by Eq. (2.19) and Eq. (2.20), respectively [5, 45, 21]. Another equivalent circuit component which is used to model the non-ideal (leaky) nature of capacitive elements often seen in real systems is a constant phase element (CPE). Eq. (2.21) provides the impedance of the CPE.

$$Z_R = R = \frac{V_0}{I_0} \tag{2.19}$$

$$Z_C = \frac{-j}{\omega C} \tag{2.20}$$

$$Z_{CPE} = \frac{1}{T(j\omega)^P} \tag{2.21}$$

The impedance of a resistor is equal to its direct current (DC) resistance, R, because it does not depend on frequency. When a sinusoidal potential is applied to a capacitor with capacitance, C, the output signal will have a 90° phase shift. Hence, the impedance is purely imaginary and multiplied by j. In a CPE, the impedance is analogous to that of a capacitor. However, two additional parameters T and P are included in the equation to describe the non-ideal capacitive behaviour of the CPE. The origin of CPE has been widely attributed to the surface roughness of solid electrodes [26]. This is due to surface roughness causing an uneven distribution of various properties, such as interfacial capacitance, across the electrode surface. Studies between electrodes with different roughness have shown that the CPE behaviour is closer to the ideal case as the electrode roughness increases [25]. Other theories, supported by experimental data, are related to the mixture of fast ionic diffusion and slow kinetic-controlled adsorption [23, 35, 34]. This explanation also supports the earlier surface roughness theory. At a higher surface roughness, the coverage due to the adsorbed ions is smaller [29]. For both capacitors and CPEs, their impedance decreases with increasing angular frequency.

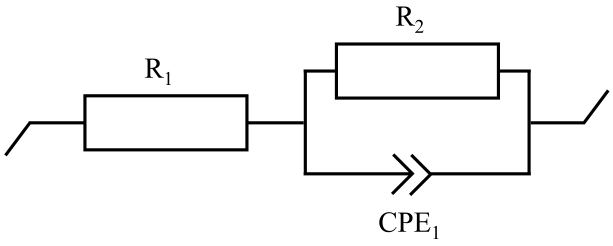

Figure 2.4: Equivalent circuit model used to represent the physical arrangements of the experimental setup in Figure 2.3.

The physical set-up of the EIS measurements included in this thesis is as shown in Figure 2.3. The SE is sandwiched between gold-blocking electrodes. The equivalent circuit

should closely mirror the physical setup. In reality, this can be quite difficult because differences between the simulated and measured Nyquist plots often reveal non-ideal behaviour which requires modelling with alternative components. CPEs are frequently used in place of capacitors to take the non-ideal behaviour into account. The equivalent circuit model used to represent the physical arrangements of the experimental setup can be found in Figure 2.4. It consists of two resistors and one constant phase elements Figure 2.4. In this circuit, R_1 corresponds to the instrument cabling or electric contact while R_2 and CPE_1 correspond to the total ionic conduction. In some cases, an additional semicircle may be present next to the first at a lower frequency. This semicircle arises from the internal interfaces such as grain boundaries, which often have higher ionic resistances. It can be incorporated into the equivalent circuit by adding an additional resistor-CPE parallel unit in series with the bulk resistor-CPE parallel unit. In this case, the overall ionic resistance of the electrolyte is equal to the sum of the two resistances. Once the ionic resistance of the SE is found, ionic conductivity, σ can be calculated using Eq. (2.22).

$$\sigma = \frac{L}{RA} \tag{2.22}$$

Where L is the separation of the two electrodes, which is equal to the thickness of the SE, R is the ionic resistance of the electrolyte, and A is the area of the current path, which in this case is equal to the area of the blocking electrode. Activation energy for ionic conduction can be obtained by performing impedance measurements at a series of temperatures. It is determined from the gradient of $\ln \sigma$ against $1/T$, also known as the Arrhenius plot.

2.4.4 Chronoamperometry

Chronoamperometry is one of the potential pulse techniques that can be employed to measure the current which arises after the capacitive current [14]. Pure ionic, electronic, and mixed ionic/ electronic materials can be easily distinguished by observing the current response. In this technique, the potential is applied in steps, from a value where the analyte is not oxidised or reduced, to a value where it is. The current is diffusion-controlled and plotted as a function of time.

The step time τ is the time during which the potential is maintained at the same value. It should be neither too short nor too long. If it is too short, the current measured includes the charging current. For a liquid system, measurement is usually in the order of seconds but for a solid system, as is studied in this thesis, it is in the order of hours [14]. In the case of a pure electronic conductor, the current will jump to a certain amount when the potential is applied and remains constant because electrons can easily transport through the material and the blocking electrode. By dividing the voltage by the current, electrode resistance can be calculated. Conversely, in the case of a mixed ionic and electronic conductor, such as antiperovskite SEs, the current will jump as potential is applied. It will then start to diminish and eventually reach a plateau because the ionic contribution to the passing current will diminish due to the blocking electrode [48, 47]. Ohm's law at the steady state current values was used to calculate the resistances, which was then used to calculate the electronic conductivities.

In this thesis, chronoamperometry was performed using the same cell setup employed for EIS measurements, Figure 2.3. This setup differs from the one employed in the Wagner-

Hebb method, where a blocking electrode is applied on one side of the SE, and an alloy (non-blocking electrode) is applied on the opposite side. Four electrodes were connected to the cell to mitigate the adverse effects of overpotential at the current-carrying electrodes. The electronic conductivity results obtained through the two ion-blocking electrodes method will differ from those achieved using the Wagner-Hebb method. Instead, it sets an upper limit for electronic conductivity [46].

2.5 Bibliography

[1] Electrons in SEM. URL https://www.thermofisher.com/uk/en/home/materials-science/learning-center/applications/sem-electrons.html#:~:text=Backscattered%20electrons%20are%20reflected%20back,electron%20beam%20and%20the%20sample.

[2] Nuclear Magnetic Resonance Spectroscopy - Theoretical Principles. URL https://teaching.shu.ac.uk/hwb/chemistry/tutorials/molspec/nmr1.htm#.

[3] XRD Principle. URL https://ywcmatsci.yale.edu/principle-0.

[4] ISO 18754:2020, 2020. URL https://www.iso.org/standard/69745.html.

[5] Basics of Electrochemical Impedance Spectroscopy, 2022. URL https://www.gamry.com/application-notes/EIS/basics-of-electrochemical-impedance-spectroscopy/.

[6] Ernest Ahiavi, James A. Dawson, Ulas Kudu, Matthieu Courty, M. Saiful Islam, Oliver Clemens, Christian Masquelier, and Theodosios Famprikis. Mechanochemical synthesis and ion transport properties of Na3OX (X = Cl, Br, I and BH4) antiperovskite solid electrolytes. *J. Power Sources*, 471:228489, 2020. ISSN 03787753. doi: 10.1016/j.jpowsour.2020.228489. URL https://doi.org/10.1016/j.jpowsour.2020.228489.

[7] Hiroaki Asakawa, Wei Shi, Mariko Murayama, and Xinwei Zhao. Structural manipulation for solid electrolyte Na3OBr by sulfur ions doping. *Japanese Journal of Applied Physics*, 61(SD), 6 2022. ISSN 13474065. doi: 10.35848/1347-4065/ac4e4b.

[8] V V Boldyrev. SOLID STATE IOMICS Mechanochemistry and mechanical activation of solids. Technical report, 1993.

[9] Bernard A Boukamp and Ross Macdonald. Alternatives to Kronig-Kramers transformation and testing, and estimation of distributions. *Solid State Ionics*, 74:85–101, 1994.

[10] W. H. Bragg and W. L. Bragg. The Reflection o f X-rays by Crystals. *Proceedings of the Royal Society A: Mathematical, Physical and Engineering Sciences*, 88:428–438, 1913. URL https://royalsocietypublishing.org/.

[11] Yet-Ming Chiang, Dunbar P. Birnie, and W. David Kingery. *Physical Ceramics: Principles for Ceramic Science and Engineering*. Wiley, 5 1996.

[12] A. A. Coelho. Topas Academic V6, 2016.

[13] Roberto D'Amato, Roberto Bondi, Intissar Moghdad, Fabio Marmottini, Matthew J.

McPherson, Houcine Naïli, Marco Taddei, and Ferdinando Costantino. "shake 'n Bake" Route to Functionalized Zr-UiO-66 Metal-Organic Frameworks. *Inorganic Chemistry*, 60(18):14294–14301, 9 2021. ISSN 1520510X. doi: 10.1021/acs.inorgchem.1c01839.

[14] Alice Delcourt-Lancon. *Electrochemical Analysis Supported by Macro and Microelectrode Array*. PhD thesis, 2011.

[15] Natasha Erdman, David C. Bell, and Rudolf Reichelt. Scanning Electron Microscopy. In *Springer Handbook of Microscopy*, pages 229–318. 2019.

[16] John S.O. Evans and Ivana Radosavljevic Evans. Structure Analysis from Powder Diffraction Data: Rietveld Refinement in Excel. *Journal of Chemical Education*, 98 (2):495–505, 2 2021. ISSN 19381328. doi: 10.1021/acs.jchemed.0c01016.

[17] G. Greczynski and L. Hultman. X-ray photoelectron spectroscopy: Towards reliable binding energy referencing, 1 2020. ISSN 00796425.

[18] Olivier Guillon, Jesus Gonzalez-Julian, Benjamin Dargatz, Tobias Kessel, Gabi Schierning, Jan Räthel, and Mathias Herrmann. Field-assisted sintering technology/spark plasma sintering: Mechanisms, materials, and technology developments. *Advanced Engineering Materials*, 16(7):830–849, 2014. ISSN 15272648. doi: 10.1002/adem.201300409.

[19] John Hanna. MS7072 - Principles & Applications of Solid State NMR, 2023.

[20] Robert House. *The Redox Chemistry of Oxygen in Cathode Materials for Rechargeable Alkali-ion Batteries*. PhD thesis, University of Oxford, Oxford, 2019.

[21] R. A. Huggins. *Advanced Batteries*. Springer, 2009.

[22] Derrick Kaseman, Sureyya Ozcan, and Siyi Du. NMR - Theory. URL https://chem.libretexts.org/Bookshelves/Physical_and_Theoretical_Chemistry_Textbook_Maps/Supplemental_Modules_(Physical_and_Theoretical_Chemistry)/Spectroscopy/Magnetic_Resonance_Spectroscopies/Nuclear_Magnetic_Resonance/NMR_-_Theory.

[23] Zsolt Kerner and Tamás Pajkossy. Measurement of adsorption rates of anions on Au(111) electrodes by impedance spectroscopy. *Journal of Electroanalytical Chemistry*, 414(2):209–220, 1996. URL www.elsevier.com/locate/electacta.

[24] J. S. Konstanty. Applications of powder metallurgy to cutting tools. In *Advances in Powder Metallurgy*, pages 555–585. Woodhead Publishing Limited, 2013.

[25] Andrzej Lasia. Electrochemical Impedance Spectroscopy and its Applications. In B. E. Conway, J. O'M. Bockris, and Ralph E. White, editors, *Modern Aspects of Electrochemistry*, pages 143–248. Kluwer Academic/ Plenum, New York, 1999.

[26] Andrzej Lasia. The Origin of the Constant Phase Element. *Journal of Physical Chemistry Letters*, 13(2):580–589, 1 2022. ISSN 19487185. doi: 10.1021/acs.jpclett.1c03782.

[27] Alexandros Ch Lazanas and Mamas I. Prodromidis. Electrochemical Impedance Spectroscopy-A Tutorial. *ACS Measurement Science Au*, 3(3):162–193, 6 2023. ISSN 2694250X. doi: 10.1021/acsmeasuresciau.2c00070.

[28] Jiangbin Luo, Shengwen Zhong, Zeya Huang, Bing Huang, and Chang An Wang. High Li+-conductive perovskite Li3/8Sr7/16Ta3/4Zr1/4O3 electrolyte prepared by hot-pressing for all-solid-state Li-ion batteries. *Solid State Ionics*, 338:1–4, 10 2019. ISSN 01672738. doi: 10.1016/j.ssi.2019.04.010.

[29] M. H. Martin and A. Lasia. Influence of experimental factors on the constant phase element behavior of Pt electrodes. *Electrochimica Acta*, 56(23):8058–8068, 9 2011. ISSN 00134686. doi: 10.1016/j.electacta.2011.02.068.

[30] Marcus H. Mendenhall, David Black, Donald Windover, and James P. Cline. Polarization effects of X-ray monochromators modeled using dynamical scattering theory. *Acta Crystallographica Section A: Foundations and Advances*, 77:262–267, 7 2021. ISSN 20532733. doi: 10.1107/S2053273321003879.

[31] Sudarshan Narayanan, Ulderico Ulissi, Joshua S. Gibson, Yvonne A. Chart, Robert S. Weatherup, and Mauro Pasta. Effect of current density on the solid electrolyte interphase formation at the lithium|Li6PS5Cl interface. *Nature Communications*, 13(1), 12 2022. ISSN 20411723. doi: 10.1038/s41467-022-34855-9.

[32] Han Nguyen, Sunny Hy, Erik Wu, Zhi Deng, Mojtaba Samiee, Thomas Yersak, Jian Luo, Shyue Ping Ong, and Ying Shirley Meng. Experimental and Computational Evaluation of a Sodium-Rich Anti-Perovskite for Solid State Electrolytes. *J. Electrochem. Soc.*, 163(10):A2165–A2171, 2016. ISSN 0013-4651. doi: 10.1149/2.0091610jes.

[33] Meisam Omidi, Atena Fatehinya, Masomeh Farahani, Zahra Akbari, Saleheh Shahmoradi, Fatemeh Yazdian, Mohammadreza Tahriri, Keyvan Moharamzadeh, Lobat

Tayebi, and Daryoosh Vashaee. Characterization of biomaterials. In *Biomaterials for Oral and Dental Tissue Engineering*, pages 97–115. 2017.

[34] Tam Pajkossy. Capacitance dispersion on solid electrodes: anion adsorption studies on gold single crystal electrodes. *Solid State Ionics*, 94(1-4):123–129, 1997.

[35] Tamas Pajkossy, Thomas Wandlowski, and Dieter M Kolb. Impedance aspects of anion adsorption on gold single crystal electrodes. *Journal of Electroanalytical Chemistry*, 414:209–220, 1996.

[36] Tatyana Polenova, Rupal Gupta, and Amir Goldbourt. Magic angle spinning NMR spectroscopy: A versatile technique for structural and dynamic analysis of solid-phase systems. *Analytical Chemistry*, 87(11):5458–5469, 6 2015. ISSN 15206882. doi: 10.1021/ac504288u.

[37] Gregory J. Rees. *Development of Solid State NMR to Understand Materials Involved in Catalytic Technology used in Fuel Cells*. PhD thesis, University of Warwick, Warwick, 2012.

[38] Bernd Reif, Sharon E. Ashbrook, Lyndon Emsley, and Mei Hong. Solid-state NMR spectroscopy. *Nature Reviews Methods Primers*, 1(1), 12 2021. ISSN 26628449. doi: 10.1038/s43586-020-00002-1.

[39] H. M. Rietveld. A Profile Refinement Method for Nuclear and Magnetic Structures. *J. Appl. Cryst*, 2:65–71, 1969.

[40] Hazime Saitô, Isao Ando, and Ayyalusamy Ramamoorthy. Chemical shift tensor - The heart of NMR: Insights into biological aspects of proteins. *Progress in Nuclear*

Magnetic Resonance Spectroscopy, 57(2):181–228, 8 2010. ISSN 00796565. doi: 10.1016/j.pnmrs.2010.04.005.

[41] Thomas Benjamin Smith, Alessandro Principi, and Bernard A Boukamp. To cite this article: Bernard A. Boukamp. *J. Electrochem. Soc*, 142:1885–1894, 1995.

[42] Scott A Speakman. Basics of X-Ray Powder Diffraction. URL `http://prism.mit.edu/xray`.

[43] L Takacs. Solid state reactions induced by ball milling. Technical report, 1998.

[44] Ping Chun Tsai, Sunil Mair, Jeffrey Smith, David M. Halat, Po Hsiu Chien, Kwangnam Kim, Duhan Zhang, Yiliang Li, Liang Yin, Jue Liu, Saul H. Lapidus, Jeffrey A. Reimer, Nitash P. Balsara, Donald J. Siegel, and Yet Ming Chiang. Double Paddle-Wheel Enhanced Sodium Ion Conduction in an Antiperovskite Solid Electrolyte. *Adv. Energy Mater.*, 13(7):2203284, 2 2023. ISSN 16146840. doi: 10.1002/aenm.202203284.

[45] Stephen J. Turrell, Hyeon Jeong Lee, Marco Siniscalchi, Sudarshan Narayanan, Mauro Pasta, Susannah C. Speller, and Chris R.M. Grovenor. Fabrication of thin solid electrolytes containing a small volume of an Li3OCl-type antiperovskite phase by RF magnetron sputtering. *Materials Advances*, 3(24):8995–9008, 10 2022. ISSN 26335409. doi: 10.1039/d2ma00971d.

[46] Michael J. Wang, Jeffrey B. Wolfenstine, and Jeff Sakamoto. Mixed Electronic and Ionic Conduction Properties of Lithium Lanthanum Titanate. *Advanced Functional Materials*, 30(10), 3 2020. ISSN 16163028. doi: 10.1002/adfm.201909140.

[47] Xinxin Wang, Jingjing Chen, Zhiyong Mao, and Dajian Wang. Effective resistance to dendrite growth of NASICON solid electrolyte with lower electronic conductivity. *Chemical Engineering Journal*, 427, 1 2022. ISSN 13858947. doi: 10.1016/j.cej.2021.130899.

[48] Xinxin Wang, Wentao Mei, Jingjing Chen, Dajian Wang, and Zhiyong Mao. Rare Earth Oxide-Assisted Sintered NASICON Electrolyte Composed of a Phosphate Grain Boundary Phase with Low Electronic Conductivity. *ACS Applied Energy Materials*, 5(1):777–783, 1 2022. ISSN 25740962. doi: 10.1021/acsaem.1c03254.

[49] Sebastian Wenzel, Stefan J. Sedlmaier, Christian Dietrich, Wolfgang G. Zeier, and Juergen Janek. Interfacial reactivity and interphase growth of argyrodite solid electrolytes at lithium metal electrodes. *Solid State Ionics*, 318:102–112, 5 2018. ISSN 01672738. doi: 10.1016/j.ssi.2017.07.005.

[50] George Youssef. Characterization of polymers. In *Applied Mechanics of Polymers*, pages 273–299. 2022.

[51] Siti Aishah Kamarul Zaman, Samayamutthirian Palaniandy, and Zuhailawati Hussain. Mechanochemical synthesis of nanostructured SiO2-SiC composite through high-energy milling. *Journal of Alloys and Compounds*, 502(1):250–256, 7 2010. ISSN 09258388. doi: 10.1016/j.jallcom.2010.04.158.

[52] Yanhua Zhang, Fei Chen, Rong Tu, Qiang Shen, and Lianmeng Zhang. Field assisted sintering of dense Al-substituted cubic phase Li 7La3Zr2O12 solid electrolytes. *Journal of Power Sources*, 268:960–964, 12 2014. ISSN 03787753. doi: 10.1016/j.jpowsour.2014.03.148.

[53] Yusheng Zhao and Luke L. Daemen. Superionic conductivity in lithium-rich anti-perovskites. *Journal of the American Chemical Society*, 134(36):15042–15047, 9 2012. ISSN 00027863. doi: 10.1021/ja305709z.

[54] Jinlong Zhu, Shuai Li, Yi Zhang, John W Howard, Xujie Lü, Yutao Li, Yonggang Wang, Ravhi S Kumar, Liping Wang, and Yusheng Zhao. Enhanced ionic conductivity with Li7O2Br3 phase in Li3OBr anti-perovskite solid electrolyte. *Appl. Phys. Lett.*, 109(10):101904, 9 2016. ISSN 0003-6951. doi: 10.1063/1.4962437. URL https://doi.org/10.1063/1.4962437.

3 | Synthesis and Characterisation of Na_3OB (B = Cl, Br, or BH_4)

3.1 Introduction

Na_2O is one of the precursors used to synthesise NaRAPs. The lack of commercially available highly pure Na_2O has been highlighted in the literature [18, 1]. NaRAPs syntheses using commercial Na_2O are as common as those using 'homemade' pure Na_2O [18, 25, 1, 34, 29, 2]. However, in the literature, there is no in-depth analysis of how the difference in a precursor's purity will affect the final products available. Through a combination of XRD and NMR, this chapter will provide evidence of both crystalline and poorly crystalline impurities that each of the precursors leads to. Multiple Na_3OX antiperovskites with Goldschmidt's tolerance factor (t) between 0.84 and 0.97 were synthesised [4, 31, 33]. Three compositions within this range, Na_3OCl, Na_3OBr, and Na_3OBH_4, were chosen as they are supposed to have stable cubic antiperovskite structures. It has been reported by Sun et al. that Na_3OBH_4 possesses much higher conductivity compared to the other two traditional NaRAPs [24]. Attempts to reproduce this result have had mixed success, with ionic conductivity ranging from 10^{-10} to $10^{-3}\,\mathrm{S\,cm^{-1}}$ at RT [1]. We show in this chapter that the ionic conductivity of Na_3OBH_4 measured via EIS at $80\,^{\circ}\mathrm{C}$ is around $10^{-7}\,\mathrm{S\,cm^{-1}}$. This finding is important because it adds another data point to the published findings on Na_3OBH_4. Our results support that the ionic conductivity of Na_3OBH_4 is not significantly different from that of other compositions with simple anions like Na_3OBr or

Na_3OCl. Therefore, it is worth including Na_3OBH_4 in this chapter. Research on NaRAPs as solid electrolytes is still at an early stage and there are some properties, like interfacial stability against sodium metal anode and electronic conductivity, which need to be verified experimentally to determine whether this family of materials is indeed suitable for solid electrolytes. The absence of (semi)metallic elements, which are at the root of reductive instability with Na metal anodes, is the primary reason why researchers expect minimal electronic conductivity and excellent electrochemical stability [1, 7, 22]. Additionally, it is scientifically interesting to determine whether Na_3OBH_4's other properties are very different from Na_3OCl and Na_3OBr due to its rotational cluster anion. Building on the simulation work on NaRAPs' and LiRAPs' bandgaps, and the experimental work that shows Li_2OHCl's good stability against lithium metal [10, 6, 32, 8, 20], we performed chronoamperometry and in-situ XPS measurements to investigate the NaRAPs' electronic conductivities and stabilities against a Na metal anode. The results show that they indeed have good stability against an Na metal anode and the electronic conductivities are in the range of 10^{-10} $\mathrm{S\,cm^{-1}}$, slightly lower than that reported for NASICON 10^{-9} - 10^{-8} $\mathrm{S\,cm^{-1}}$ using a similar method [28, 27].

3.2 Experimental

3.2.1 Na_3OB (B = Cl, Br, or BH_4) Synthesis

Two batches of Na_3OB (B = Cl, Br, or BH_4) were synthesised. The first was with commercially available Na_2O, which contained about 20% of Na_2O_2 impurity, and the second was with 'homemade' Na_2O. Details about 'homemade' Na_2O synthesis can be found in

Chapter 2. Samples from the first batch will be called 'commercial' Na_3OB (B = Cl, Br, or BH_4) while those from the second batch will be called 'homemade' Na_3OB (B = Cl, Br, or BH_4) from here on. The ratio of the precursors for the first batch and second batch can be found in Eq. (3.1) and Eq. (3.2) respectively.

$$0.8Na_2O + 0.2Na_2O_2 + NaB \rightarrow Na_3OB + 0.5O_2 \tag{3.1}$$

$$Na_2O + NaB \rightarrow Na_3OB \tag{3.2}$$

In both batches, the synthesis procedures were identical. Commercial precursors (Na_2O - Sigma Aldrich , 80% Na_2O and 20% Na_2O_2, NaBr - Sigma Aldrich, ACS reagent, $\geqslant$ 99.0%, NaCl Sigma Aldrich, ACS reagent, $\geqslant$ 99.0%, and $NaBH_4$ - Sigma Aldrich, ACS reagent, $\geqslant$ 98.0%) were dried at $120\,^{\circ}\mathrm{C}$ for 12 h in a glass vacuum oven (Buchi). They were then loaded into a 45 ml ZrO_2 milling jar containing ten 5 mm diameter and five 10 mm diameter ZrO_2 balls. A planetary ball mill (Fritsch Puverisette 7 Premium) was used at 350 rpm for a total effective milling time of 10 hours with a 5-minute pause for every 10 minutes of milling. Subsequently, the ball-milled powder was heated in a 15 ml cylindrical alumina crucible at $450\,^{\circ}\mathrm{C}$ for 24 hours and left to cool down to room temperature inside the muffle furnace. To form the sample for ionic conductivity measurement, the as-synthesised Na_3OB (B = Cl, Br, or BH_4) samples were then ground to fine powders using mortar and pestle for 10 minutes.

3.2.2 Pellet Processing

Two different types of pellets were prepared for the electrochemical characterisation: cold pressed (CP) and hot pressed (HP). To form the CP pellets, each Na_3OB composition was pressed into a 5 mm diameter cylindrical polyether ether ketone (PEEK) die at $370\,\mathrm{MPa}$ for $3\,\mathrm{min}$. For the HP pellets, each Na_3OB sample was ground and pressed into a 5 mm diameter cylindrical steel die at $370\,\mathrm{MPa}$ and $180\,^{\circ}\mathrm{C}$ using a heating jacket. The final thickness of both the CP and HP pellets was around $300\,\mu\mathrm{m}$.

3.2.3 Differential Scanning Calorimetry (DSC)

The DSC instrument was operated in air, so the sample was sealed in an aluminium hermetic pan inside the glovebox prior to the measurement to protect it from moisture. Measurements were performed between 25 and $300\,^{\circ}\mathrm{C}$ with a heating rate of $5\,^{\circ}\mathrm{C\,min^{-1}}$.

3.2.4 Electrochemical Impedance Spectroscopy (EIS)

The EIS characterisation was carried out in a custom-built PEEK solid-state cell using gold powder (Alfa Aesar, gold powder, spherical, APS 0.5 – $0.8\,\mu\mathrm{m}$) as the blocking electrodes.[5] Gold powder was added to one side of the cold pressed pellet and then pressed at 370 MPa for 3 minutes before turning the pellet over to perform the same procedure on the opposite side. Using a screw on top of the cell, a uniaxial pressure of $\approx$ 70 MPa was applied during the measurements. The cell was then heated inside a muffle furnace in a glovebox for an hour at each data point before a measurement was performed using a two-probe configuration to a BioLogic MTZ35 frequency response analyser. Potentiostatic EIS (PEIS) measurements were conducted in the frequency range

of 35 MHz to 0.1 Hz with a voltage amplitude of 10 mV. ZView software was used to simulate Nyquist plots.

3.2.5 Chronoamperometry

Chronoamperometry was performed with the same cell setup as the impedance spectroscopy. The measurements were done with BioLogic VMP3 multichannel potentiostat at $100\,^{\circ}\mathrm{C}$ at an increasing potential of $0.1\,\mathrm{V}$, $0.3\,\mathrm{V}$, and $0.5\,\mathrm{V}$ for 5 hours each.

3.2.6 Ex-situ Scanning Electron Microscopy (SEM)

SEM measurements were conducted using a Thermo-Fisher Helios G4-CXe Plasma FIB (PFIB) instrument with energy-dispersive X-ray spectroscopy (EDX) functionality (Oxford Instruments). Both cold pressed (CP) and hot pressed (HP) pellets were mounted on a transportable SEM stage with carbon tape inside an Ar-filled glovebox before sealing in a Gatan iLoad sample transfer vessel. A trench from the top surface of about $50\,\mu\mathrm{m}$ was then milled using the Xe-ion beam. Since the FIB column was at a 52° angle to the SEM column, the sample must be tilted to this angle for milling and imaging of the cross-section.

3.2.7 X-ray Diffraction (XRD)

Ex-situ X-ray powder diffraction measurements were performed on the precursors and the synthesised Na_3OB compositions using Rigaku Miniflex diffractometers (Cu Kα). Data were collected between 10 and 90° with a step size of 0.02°. To make sure that the sample alignment was correct, the powder sample surface was levelled with the top of the sample

holder by using a glass slide.

3.2.8 Nuclear Magnetic Resonance (NMR) Spectroscopy

Room temperature ^{23}Na static solid-state NMR measurements were completed at magnetic field strengths of 20 T (ν_0 ^{23}Na = 264.6 MHz) and 23.5 T (ν_0 ^{23}Na = 224.9 MHz) using Bruker Neo consoles and 3.2 mm probes. The spectra were referenced to NaCl at 7.2 ppm [15], and were recorded using a Hahnecho (π/2 - τ - π - τ) sequence with 400 kHz WURST (wideband, uniform rate, smooth truncation) excitation and refocussing pulses for broadband excitation of the $\approx$ 220 kHz wide resonances (at 20 T)[13, 12].

3.2.9 In-situ X-ray Photon Spectroscopy (XPS)

Sodium metal foil (Sigma Aldrich), $\approx 200\,\mu\mathrm{m}$, was surface cleaned mechanically by scraping and fixed to an L-shaped target holder by using double-sided adhesive tape. Pellets, with diameter of $5\,\mathrm{mm}$ and thickness of $\approx 500\,\mathrm{um}$, were cold pressed under $370\,\mathrm{MPa}$. To calibrate the thickness of the sputtered sodium, Cu mesh ($\approx 12.5\,\mu\mathrm{m}$, 99.9% purity, Advent Research Materials) was pressed on top of the pellets. Details about the calibration method can be found in Chapter 2. The samples were then mounted onto the holder with a conductive adhesive carbon tape and transferred into the XPS machine using an inert transfer system. The chamber pressure during the in-situ experiment was in the range of $10^{-7}\,\mathrm{Pa}$ to $10^{-6}\,\mathrm{Pa}$. During the measurement, the sample was flooded with slow electrons and argon ions from the built-in ion sputter and electron guns to compensate for surface charging effects.

3.3 Results and discussion

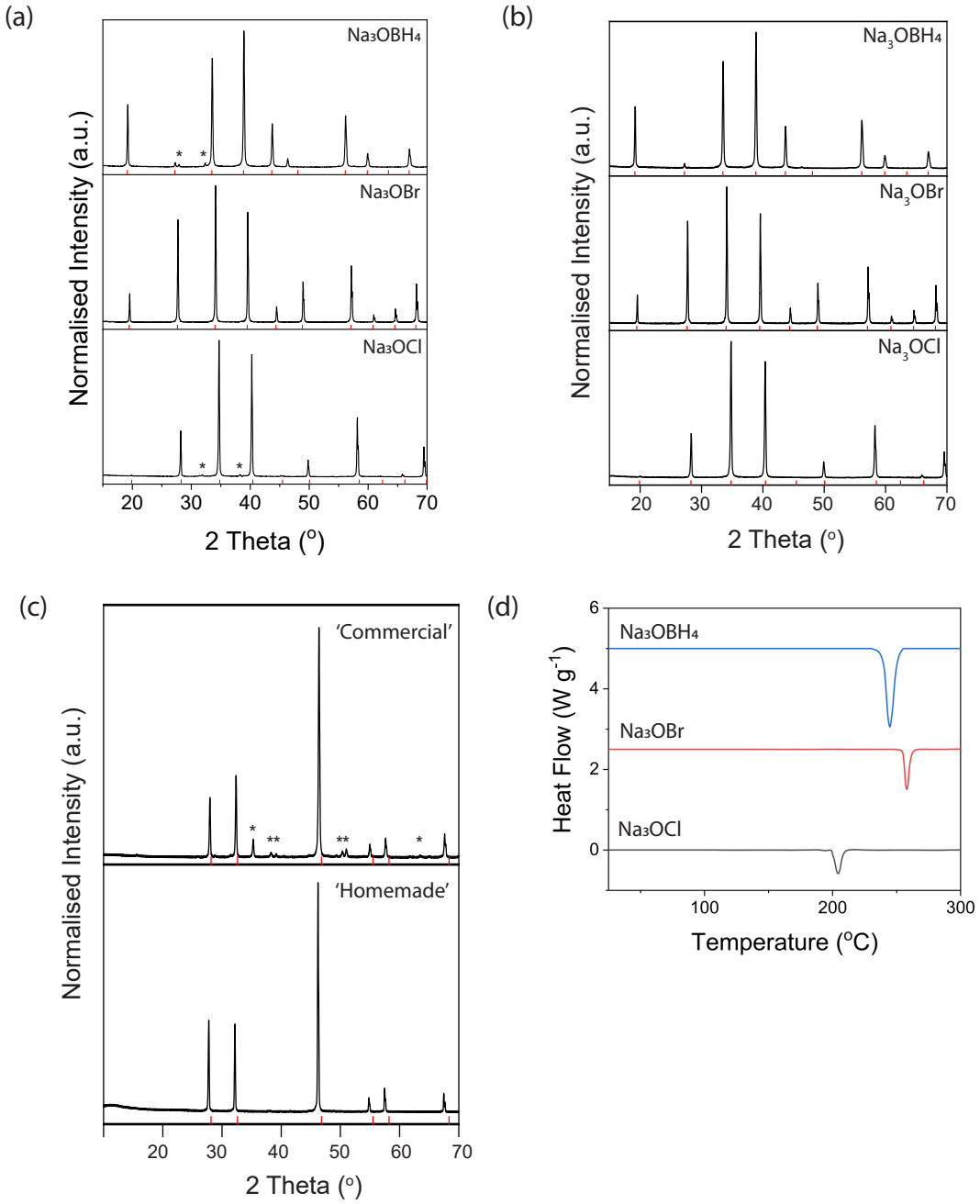

Figure 3.1: (a) XRD pattern of 'commercial' Na_3OCl, Na_3OBr, and Na_3OBH_4. The peak positions of impurities resulting from the use of 'commercial' Na_2O, which contains 20% impurities primarily of Na_2O_2, are marked with asterisks (*). (b) XRD pattern of 'homemade' Na_3OCl, Na_3OBr, and Na_3OBH_4. Impurity peaks related to the (c) XRD pattern of 'commercial' and 'homemade' Na_2O. The peak positions of impurities present in 'commercial' Na_2O are indicated with asterisks (*). (d) DSC of 'homemade' Na_3OCl, Na_3OBr, and Na_3OBH_4.

To assess the phase purity of the 'homemade' Na_2O and two batches of Na_3OX powders, XRD were performed using Cu $K\alpha$ radiation, Figure 3.1a and Figure 3.1b. The Na_2O structure matches the Fm-3m space group while the Na_3OX compositions match the Pm-3m space group, as previously reported. From Pawley refinements, the lattice parameters of the compositions from the first and second batches were found to be almost identical, as seen in Table 3.1. A small amount of NaCl and $NaBH_4$ impurities were observed in the 'commercial' Na_3OCl and Na_3OBH_4. 'Commercial' Na_2O contains 20% Na_2O_2 impurity. This significant amount of impurity was taken into account when determining the amount of precursors required to form the final product, as seen in Eq. (3.1). Moreover, a combination of high energy ball-milling and heating ($450\,^{\circ}\mathrm{C}$) is expected to turn Na_2O_2 into Na_2O and O_2. Even though the successful formation of NaRAPs has been reported in previous literature, a minor amount of impurities were sometimes reported [18, 29]. On the other hand, no crystalline impurity was observed in the 'homemade' Na_2O and the subsequent Na_3OCl, Na_3OBr, and Na_3OBH_4 which were synthesised with it. To confirm if the homemade materials are indeed pure and do not contain poorly crystalline impurities, we proceeded to perform static solid-state nuclear magnetic resonance (NMR).

Composition	Na_3OCl	Na_3OBr	Na_3OBH_4
'Commercial' (Å)	4.567	4.495	4.635
'Homemade' (Å)	4.564	4.490	4.634

Table 3.1: Lattice parameters

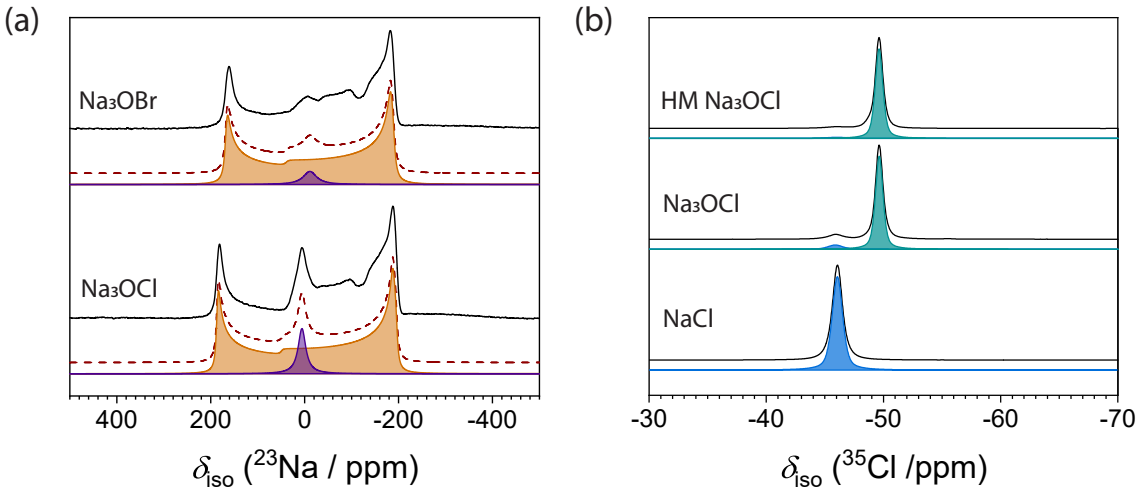

Figure 3.2: (a) Room temperature ^{23}Na static WURST-echo NMR spectra (black) of 'commercial' Na_3OBr and 'commercial' Na_3OCl at 20 T (ν_0 = 224.9 MHz). The orange dotted lines represent the sum of the simulated Na_3OBr and Na_3OCl (orange) and impurity resonances (purple). (b) Room temperature ^{35}Cl static WURST-echo NMR spectra (black) of 'homemade' Na_3OCl, 'commercial' Na_3OCl, and NaCl at 20 T (ν_0 = 224.9 MHz). NMR experiments were performed in collaboration with Dr. Gregory J. Rees (University of Oxford).

Static ^{23}Na nuclear magnetic resonance was performed on 'commercial' Na_3OCl, and 'commercial' Na_3OBr at 20 T. Previous work on Na_3OCl has shown a single distinct broad quadrupolar resonance. However, an extremely broad quadrupolar peak and a narrower component around 0 ppm (shown in purple), which was more prominent in Na_3OCl, was observed in both compositions. The wideline Na_3OBr (orange) is deconvoluted to give $\delta_{iso} = 44ppm$, χ_Q = 11.9 MHz and η_Q = 0, which is similar to the reported value for Na_3OCl [11]. The shape and isotropic shift ($\approx$ 0 ppm) of Na_3OBr's secondary resonance originates from impurities. The impurity resonances were later deconvoluted into Na_2O, Na_2O_2, and NaOH in Chapter 4. A total of 5 % impurity is observed from the deconvolution of the NMR spectra. This amount is substantial and yet no Bragg peaks, apart from those of Na_3OBr, were detected in the XRD pattern. Therefore, the impurities contained in the sample must be poorly crystalline, which could be a result of the 10 hours of ball

milling at 350 rpm carried out during the synthesis. For Na_3OCl, the shape and isotropic shift ($\approx$ 0 ppm) of its secondary resonance is a combination of the earlier impurities and NaCl, Figure 3.2. Static ^{35}Cl nuclear magnetic resonance performed on 'homemade' and 'commercial' Na_3OCl confirmed our earlier XRD findings. The amount of NaCl impurity is higher in the commercial Na_3OCl ($\approx$ 8%) than in the homemade Na_3OCl ($\approx$ 4%). Therefore, it is important to perform the synthesis with highly pure Na_2O to reach higher final product purity, which might not be easily detectable by XRD alone.

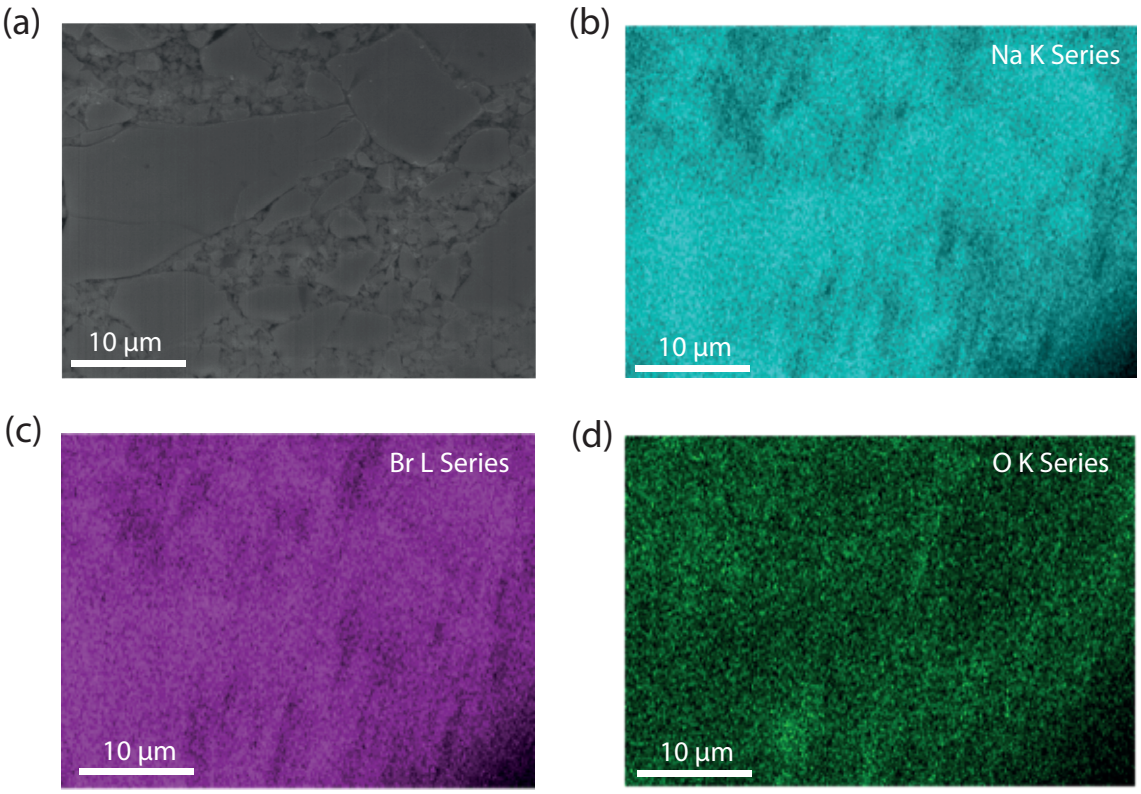

Figure 3.3: (a) Cross-sectional secondary electron image of the cold pressed 'homemade' Na_3OBr pellet before variable temperature EIS measurements. This image was taken with an accelerating voltage of 5 kV. Corresponding EDX analysis of the different elements: (b) Na (blue), (c) Br (purple), and (d) O (green). PFIB-SEM experiments were performed in collaboration with Emily Milan (University of Oxford).

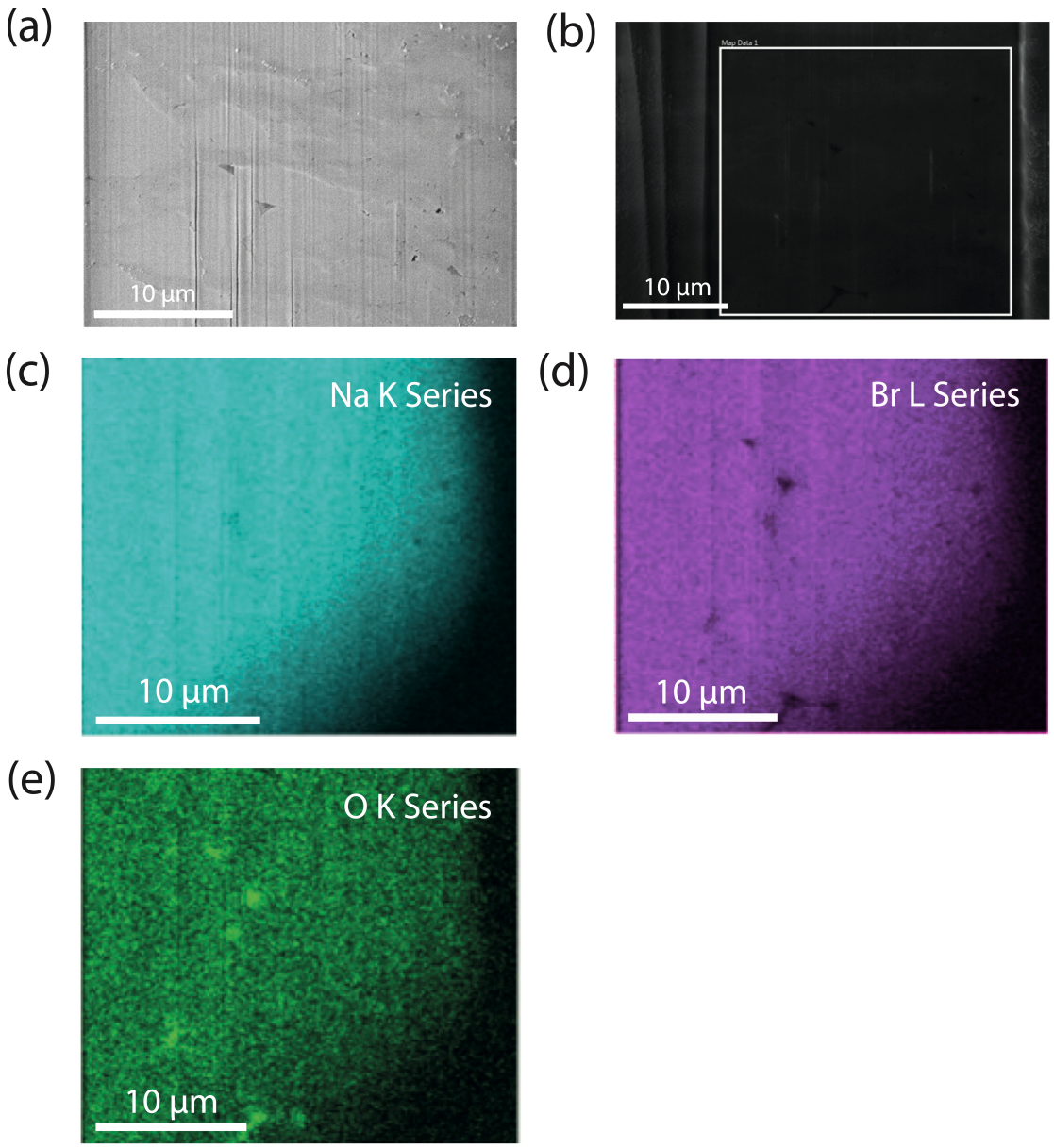

Figure 3.4: (a) and (b) Cross-sectional secondary electron images of the hot pressed 'homemade' Na_3OBr pellet before variable temperature EIS measurements. These images were taken with an accelerating voltage of 5 kV. Corresponding EDX analysis of the different elements: (c) Na (blue), (d) Br (purple), and (e) O (green). PFIB-SEM experiments were performed in collaboration with Yvonne Chart (University of Oxford).

After establishing the fact that highly pure Na_2O is necessary for NaRAPs' syntheses, further characterisations were only performed on the 'homemade' samples. DSC was carried out up to 300 °C to investigate the thermal stability of all three compositions. The choice of 300 °C as the limit was motivated by its significance, being well above the tem-

peratures (approximately $250\,^{\circ}\mathrm{C}$) at which some phase changes in NaRAPs have been reported. The DSC results presented in Figure 3.1d reveal endothermic peaks at around $250\,^{\circ}\mathrm{C}$ in all three compositions. However, these peaks do not correspond to the melting of NaRAPs, as the bulk material remains solid up to $300\,^{\circ}\mathrm{C}$. Armed with this information, it was determined that the hot pressing (HP) temperature should be maintained below approximately $250\,^{\circ}\mathrm{C}$ to observe the effect of hot pressing on the pellets without interference from the phase transition. Ionic conduction in the solid state is one of the key enablers of solid-state batteries. It is of interest to understand the effects of pellet processing on density, microstructure, and ionic conductivity. All three compositions were cold pressed (CP) and hot pressed (HP) at 370 MPa. After that, cross-section SEM was done on both the cold pressed and hot pressed pellets to examine the effect of different processing routes on the porosity and microstructure of the pellets, and a focused-ion beam (FIB) was employed to produce smooth surfaces for grain imaging. It is clear that hot pressing of Na_3OBr resulted in a significant reduction in the amount of porosity (Figure 3.3 and Figure 3.4). Although HP successfully densified the materials, some closed pores were still visible in the cross-section SEM image. No through pores were observed in both CP and HP samples. 3D sample reconstruction using PFIB-SEM will be required to confirm this. Comparing the CP and HP cross-section images, necking and grain growth were apparent in the HP sample. Necks are usually initiated at lower temperatures than densification [23]. EDS elemental mapping of the cold pressed Na_3OBr pellet reveals a uniform distribution of Na, O, and Br. Similar elemental distributions were observed in the hot pressed pellets of all three compositions, with minor oxygen-rich regions, as seen in Figure 3.4. To support the findings from the cross-section SEM, the relative density of

both the CP and HP pellets was measured based on ISO 18754 to account for the closed pores, especially in the CP pellets. ISO 18754 method was employed because the average pore size is less than $600\,\mu m$, as seen in Figure 3.3 and Figure 3.4. There were 26.3%, 26.2%, and 27.3% increases in relative densities of Na_3OCl, Na_3OBr, and Na_3OBH_4, respectively, when the pellet was hot pressed instead of cold pressed Table 3.2. These are in line with our cross-section images.

Composition	Na_3OCl	Na_3OBr	Na_3OBH_4
Cold pressed	67.1%	67.4%	68.2%
Hot pressed	93.4%	93.6%	97.2%

Table 3.2: Relative densities of cold pressed and hot pressed Na_3OCl, Na_3OBr, and Na_3OBH_4 pellets.

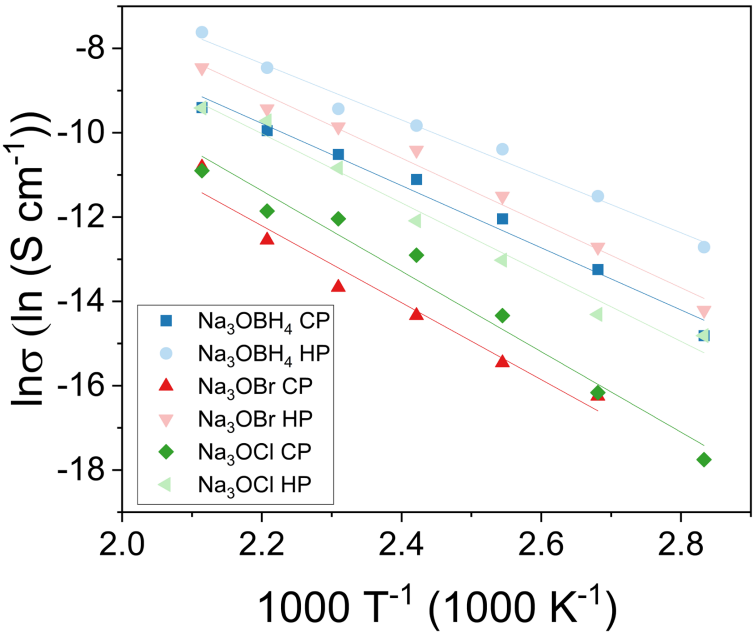

Figure 3.5: Arrhenius plots of cold pressed and hot pressed Na_3OCl, Na_3OBr, and Na_3OBH_4 pellets. Measurements were performed between $25\,^{\circ}C$ and $200\,^{\circ}C$.

Electrochemical impedance spectroscopy (EIS) was performed to analyse the Na^+ ionic conductivity of the CP and HP samples and the Arrhenius plots of 'homemade' Na_3OCl,

Na_3OBr, and Na_3OBH_4 ionic conductivities. Measurements were taken at temperatures between $25\,^{\circ}\mathrm{C}$ and $200\,^{\circ}\mathrm{C}$, as seen in Figure 3.5 For all three compositions, CP pellets have $\approx$ 1 order of magnitude lower ionic conductivities than HP pellets. Looking back into the relative density measurements and SEM images, the low ionic conductivity of CP NaRAP pellets can be attributed partially to the poor sintering and subsequently the low relative density of the pellets. As the number of open pores is reduced and necks are formed by hot pressing, the contact area between the Na_3OBr particles and between the particles and the electrodes is improved, as evident in Figure 3.4. Ionic conductivity of our Na_3OBH_4 is similar to our other NaRAP compositions and the one reported by Ahiavi et al. [1], $10^{-7}\,\mathrm{S\,cm^{-1}}$ at $100\,^{\circ}\mathrm{C}$, but is much lower than that reported by Sun et al., $10^{-3}\,\mathrm{S\,cm^{-1}}$ at room temperature [24]. This is also in line with the finding from Tsai et al. [25], where the rotations of the borohydride anions are not closely synchronised with the translation of the sodium ions during the migration events. The main difference between our sample preparation method and Sun's is the hot pressing temperature and duration. Nguyen et al. showed that the conductivity of Na_3OBr could be improved by $\approx$ 1 order of magnitude via spark-plasma sintering, thus it is unlikely that these differences could lead to more than 4 orders of magnitude difference [18]. The activation energy barrier for conduction was calculated from the linear Arrhenius plot displayed in Figure 3.5 and Table 3.3. The reduction in the Na^+ migration energy barrier of the HP samples can also be attributed to the grain growth, which reduces the total grain boundary area. Grain boundaries are known to be the bottleneck for ionic conductivity in SEs, including antiperovskites [16, 3, 21]. Therefore, the energy barrier for Na^+ is expected to decrease with less grain boundary area.

Composition	Na_3OCl (eV)	Na_3OBr (eV)	Na_3OBH_4 (eV)
Cold pressed	0.97	0.81	0.78
Hot pressed	0.87	0.75	0.70

Table 3.3: Activation energies for Na-ion conduction in cold pressed and hot pressed Na_3OCl, Na_3OBr, and Na_3OBH_4 pellets.

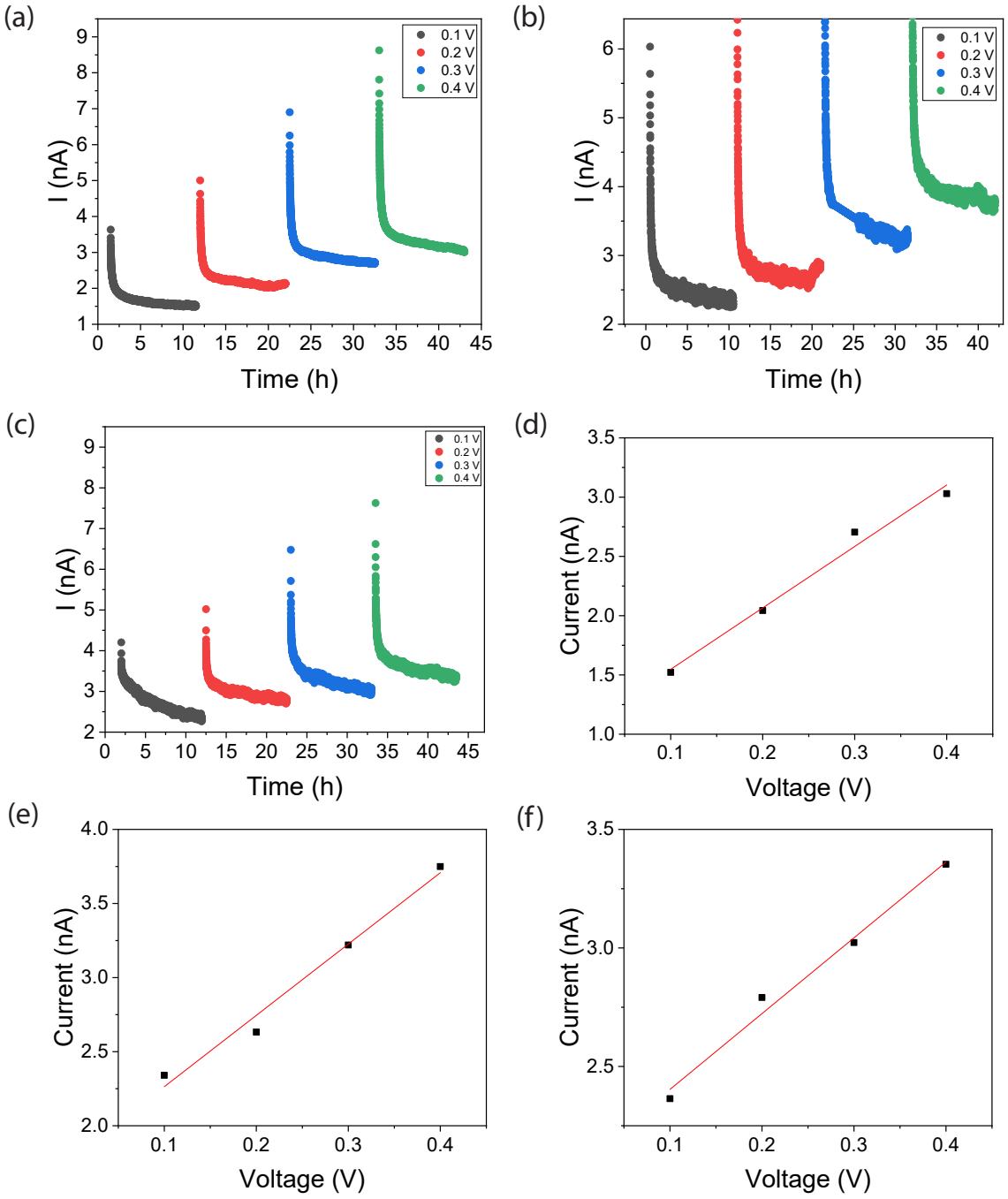

Figure 3.6: Chronoamperometries of (a) Na_3OCl, (b) Na_3OBr, and (c) Na_3OBH_4. The gradients of the current vs. voltage plots of (d) Na_3OCl, (e) Na_3OBr, and (f) Na_3OBH_4 are equal to their electronic resistances. Electronic conductivities were then calculated using these resistances.

Apart from the ionic conductivity, low electronic conductivity is also a key requirement for a suitable solid electrolyte candidate. Recent studies have found a correlation between

electronic conductivity and dendrite formation in SEs [9]. A higher electronic conductivity will result in a lower potential in the bulk electrolyte, which will increase the driving force for dendrite formation. The electronic conductivities of the cold pressed pellets were measured via chronoamperometry with gold-blocking electrodes. In this configuration, the initial current response is representative of both Na^+ and electron transport. Since there is no supply of Na^+ from the gold-blocking electrodes, the supply of mobile ions is depleted over time and the residual current becomes purely electronic. Electronic conductivities were calculated using resistances found using Ohm's law at the steady state current values (Figure 3.6). The electronic conductivities of Na_3OCl, Na_3OBr, and Na_3OBH_4 at $100\,^{\circ}\mathrm{C}$ were $7.9 \times 10^{-10}\ \mathrm{S\,cm^{-1}}$, $7.5 \times 10^{-10}\ \mathrm{S\,cm^{-1}}$, and $3.2 \times 10^{-10}\ \mathrm{S\,cm^{-1}}$, respectively. These values are lower than those reported for NASICON (10^{-9} - $10^{-8}\ \mathrm{S\,cm^{-1}}$) using similar method [28, 27]. Electronic conductivity measurement using two ion-blocking electrodes is not the same as a real Wagner-Hebb measurement using a Na electrode and an ion-blocking electrode. Instead, it provides an upper limit of the electronic conductivity [26]. Initially, we tried to measure the chronoamperometry at room temperature ($25\,^{\circ}\mathrm{C}$). However, the signal-to-noise ratio was too high due to the samples' extremely low ionic and electronic conductivities at this temperature. Therefore, the measurements were performed at $100\,^{\circ}\mathrm{C}$. Unfortunately, this temperature is above the sodium melting temperature. Due to the complications of dealing with molten sodium, the Wagner-Hebb method was not used to obtain the electronic conductivities of NaRAPs, instead ion-blocking electrodes were used on both sides of the pellets.

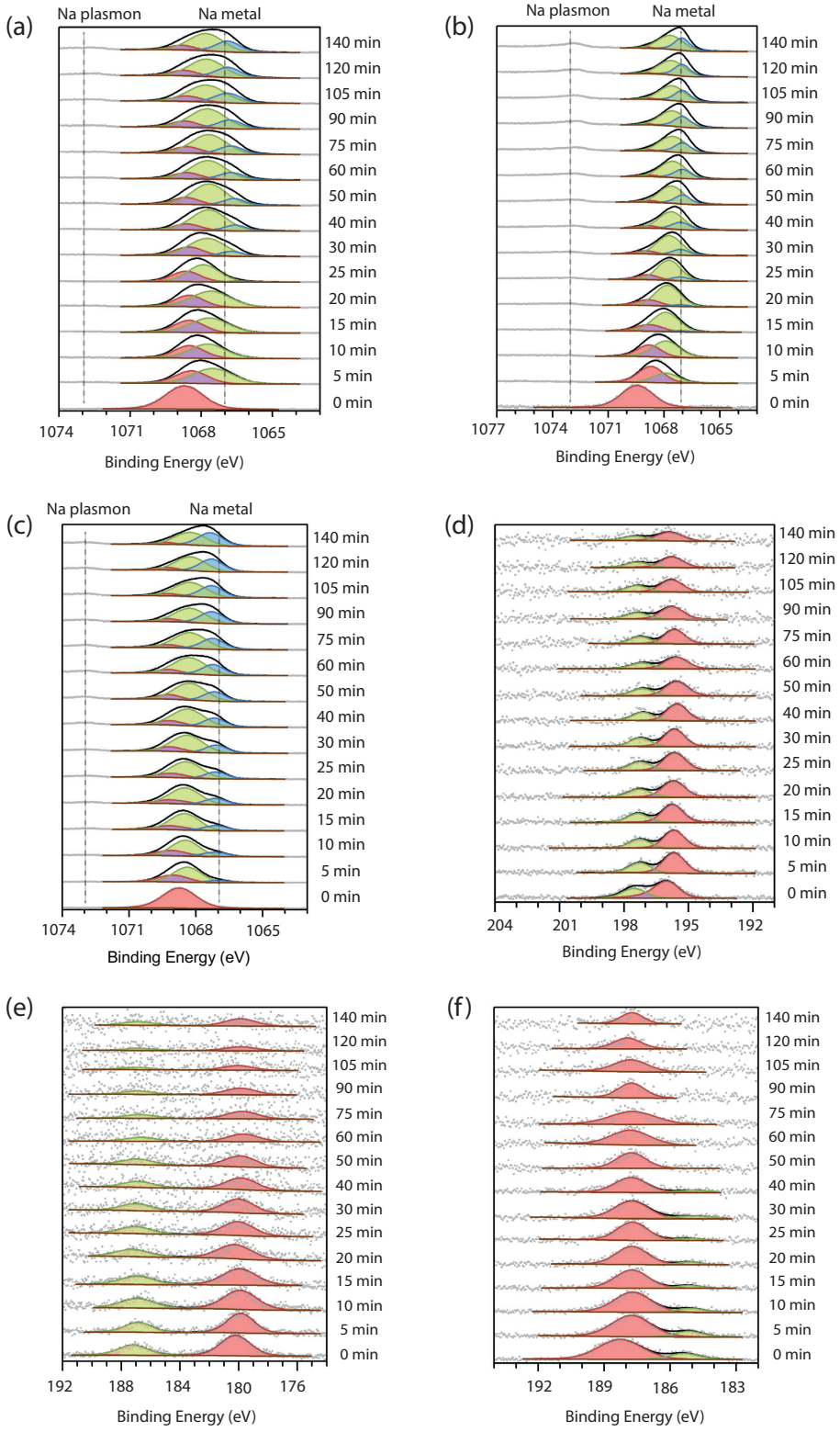

Figure 3.7: Na 1s XPS spectra of (a) Na_3OCl, (b) Na_3OBr, and (c) Na_3OBH_4. (d) Cl 2p XPS spectra of Na_3OCl. (e) Br 3p XPS spectra of Na_3OBr. (f) B 1s XPS spectra of Na_3OBH_4. All spectra were plotted as a function of increasing Na deposition time at room temperature. XPS experiments were performed in collaboration with Ben Jagger (University of Oxford).

Another great challenge for all-solid-state sodium metal batteries is finding an SE candidate which is stable against Na metal. Even the widely researched candidates, such as NASICON and sodium β-alumina, are not stable against Na metal. X-ray photoelectron spectroscopy was employed to evaluate the chemical stability of our 3 compositions against Na metal. The solid electrolyte interphase (SEI) evolution was monitored at room temperature via in-situ Na deposition and simultaneous measurement of the photoemission spectra. For all three compositions, the evolution of the Na 2p spectra initially depicts a broadening of the peak followed by a gradual shift towards lower binding energies Figure 3.7. Prior to sodium metal deposition, the peaks (red peaks in Figure 3.7a, b, and c) were assigned entirely to the pristine antiperovskites. The intensity of these antiperovskite peaks decreases with the increasing deposition time of sodium metal. Additional peaks (green peaks in Figure 3.7a, b, and c) at $\approx$ 1068 eV, assigned to SEI, were seen in all three compositions after sodium metal was deposited on top of the pellets for 5 minutes. These peaks were formed due to the reaction of Na metal with the samples, similar to what have been reported in lithium antiperovskites [14]. Additionally, in Na_3OBH_4 (blue peak), a low binding energy peak emerged at $\approx$ 1067 eV simultaneously with a Na plasmon peak at $\approx$ 1073 eV. This peak was assigned to Na metal. The same peak appeared in Na_3OBr and Na_3OCl after Na metal was deposited for 15 minutes and 25 minutes, respectively. As plating progressed, the intensity of the Na metal peaks continued to increase, while the intensity of the SEI peaks diminished. This indicates that the antiperovskites stop reacting with the Na metal, and the SEIs remain stable. As more Na metal is deposited, the SEIs become more buried, resulting in a decrease in their peak intensities. We did further analysis using the Strohmeier equation [30, 17], explained in the Experimental

section, to estimate the thickness of the sodium metal deposited. Theoretically, Na can be expected to plate out at approximate rates of 0.25 $\mathrm{nm\,min^{-1}}$, 0.27 $\mathrm{nm\,min^{-1}}$, and 0.29 $\mathrm{nm\,min^{-1}}$ for Na_3OCl, Na_3OBr, and Na_3OBH_4, respectively. These rates show slight differences, possibly due to variations in pellet positions during the measurement. To facilitate a fair comparison and determine which of the three compositions forms a stable Solid Electrolyte Interface (SEI) in the shortest time, the deposition rates were multiplied by the time required for the sodium metal peak to first appear in the spectra. This calculation resulted in the equivalent thickness of sodium metal deposited on the sample, with the most stable composition identified as the one with the lowest sodium metal thickness value. The resulting values are $6.25\,\mathrm{nm}$, $4.05\,\mathrm{nm}$, and $1.45\,\mathrm{nm}$ for Na_3OCl, Na_3OBr, and Na_3OBH_4, respectively. Comparing the three compositions, it can be concluded that Na_3OBH_4 is the most stable against Na metal followed by Na_3OBr and finally Na_3OCl. In the case of Cl 2p, Br 3p, and B 1s, all the signals of these species decrease with time. No additional peaks appeared in any of these spectra, thus there is no reaction between them and the deposited Na metal. Overall, all three sodium antiperovskite compositions form stable SEIs against Na metal and this is an important advantage of NaRAP compared to other Na-ion conductors. A further experiment using a combination of atomic force microscopy (AFM) and time-of-flight secondary ion mass spectroscopy (ToF-SIMS), as reported by Otto et al., is required to estimate the SEI thickness for each composition accurately [19].

3.4 Conclusion

Two batches of Na_3OCl, Na_3OBr, and Na_3OBH_4, one with commercially available Na_2O and another one with 'homemade' pure Na_2O were synthesised. XRD detected minor crystalline NaCl and $NaBH_4$ impurities in 'commercial' Na_3OCl and Na_3OBH_4, respectively, but no crystalline impurity peaks in 'commercial' Na_3OBr and all 'homemade' compositions. ^{23}Na static NMR revealed that 'homemade' pure Na_2O precursor significantly reduces the amount of Na_2O poorly crystalline impurity in the final product and leads to a lower amount of crystalline impurity due to a more complete reaction. In terms of processing, cross-section SEM images show no indication of through pores in both cold pressed and hot pressed pellets. hot pressing leads to fewer pores, higher interparticle contact area, and better contact between the solid electrolyte and the blocking electrodes. Therefore, $\approx$ 1 order of magnitude increase in ionic conductivity was observed when the pellets were hot pressed instead of cold pressed. The electronic conductivity of all 'homemade' compositions was found to be in the range of $10^{-10}\,\mathrm{S\,cm^{-1}}$, lower than those reported for NASICON. Finally, the in-situ XPS experiment with Na metal provided experimental evidence that Na_3OCl, Na_3OBr, and Na_3OBH_4 form stable SEIs against Na metal at room temperature, with Na_3OBH_4 being the most stable among the three compositions. Finally, Na_3OBH_4's ionic conductivity was observed to be not significantly higher than higher than Na_3OBr and Na_3OCl. However, it is more stable against Na-metal and less electronically conductive than the other two, making it a more desirable SE.

3.5 Bibliography

[1] Ernest Ahiavi, James A. Dawson, Ulas Kudu, Matthieu Courty, M. Saiful Islam, Oliver Clemens, Christian Masquelier, and Theodosios Famprikis. Mechanochemical synthesis and ion transport properties of Na3OX (X = Cl, Br, I and BH4) antiperovskite solid electrolytes. *J. Power Sources*, 471:228489, 2020. ISSN 03787753. doi: 10.1016/j.jpowsour.2020.228489. URL https://doi.org/10.1016/j.jpowsour.2020.228489.

[2] Hiroaki Asakawa, Wei Shi, Mariko Murayama, and Xinwei Zhao. Structural manipulation for solid electrolyte Na3OBr by sulfur ions doping. *Japanese Journal of Applied Physics*, 61(SD), 6 2022. ISSN 13474065. doi: 10.35848/1347-4065/ac4e4b.

[3] James A. Dawson, Pieremanuele Canepa, Theodosios Famprikis, Christian Masquelier, and M. Saiful Islam. Atomic-Scale Influence of Grain Boundaries on Li-Ion Conduction in Solid Electrolytes for All-Solid-State Batteries. *J. Am. Chem. Soc.*, 140(1):362–368, 1 2018. ISSN 15205126. doi: 10.1021/jacs.7b10593.

[4] James A. Dawson, Theodosios Famprikis, and Karen E. Johnston. Anti-perovskites for solid-state batteries: recent developments, current challenges and future prospects. *J. Mater. Chem. A*, 9(35):18746–18772, 2021. ISSN 20507496. doi: 10.1039/d1ta03680g.

[5] Christopher Doerrer, Isaac Capone, Sudarshan Narayanan, Junliang Liu, Chris R.M. Grovenor, Mauro Pasta, and Patrick S. Grant. High Energy Density Single-Crystal NMC/Li6PS5Cl Cathodes for All-Solid-State Lithium-Metal Batteries. *ACS Appl.*

Mater. Interfaces, 13(31):37809–37815, 2021. ISSN 19448252. doi: 10.1021/acsami.1c07952.

[6] Alexandra Emly, Emmanouil Kioupakis, and Anton Van Der Ven. Phase stability and transport mechanisms in antiperovskite Li 3OCl and Li3OBr superionic conductors. *Chemistry of Materials*, 25(23):4663–4670, 12 2013. ISSN 08974756. doi: 10.1021/cm4016222.

[7] Theodosios Famprikis, Pieremanuele Canepa, James A. Dawson, M. Saiful Islam, and Christian Masquelier. Fundamentals of inorganic solid-state electrolytes for batteries. *Nature Materials*, 18(12):1278–1291, 12 2019. ISSN 14764660. doi: 10.1038/s41563-019-0431-3.

[8] Hong Fang and Puru Jena. Li-rich antiperovskite superionic conductors based on cluster ions. *Proceedings of the National Academy of Sciences of the United States of America*, 114(42):11046–11051, 10 2017. ISSN 10916490. doi: 10.1073/pnas.1704086114.

[9] Fudong Han, Andrew S. Westover, Jie Yue, Xiulin Fan, Fei Wang, Miaofang Chi, Donovan N. Leonard, Nancy J. Dudney, Howard Wang, and Chunsheng Wang. High electronic conductivity as the origin of lithium dendrite formation within solid electrolytes. *Nature Energy*, 4(3):187–196, 3 2019. ISSN 20587546. doi: 10.1038/s41560-018-0312-z.

[10] Zachary D. Hood, Hui Wang, Amaresh Samuthira Pandian, Jong Kahk Keum, and Chengdu Liang. Li2OHCl Crystalline Electrolyte for Stable Metallic Lithium An-

odes. *Journal of the American Chemical Society*, 138(6):1768–1771, 2 2016. ISSN 15205126. doi: 10.1021/jacs.5b11851.

[11] G Klösters and M Jansen. Determination of the (Na+) Sternheimer antishielding factor by 23Na NMR spectroscopy on sodium oxide chloride, Na3OCl. *Solid State Nucl. Magn. Reson.*, 16(4):279–283, 7 2000. ISSN 0926-2040 (Print). doi: 10.1016/s0926-2040(00)00079-5.

[12] Eriks Kupce and Ray Freeman. Adiabatic Pulses for Wideband Inversion and Broadband Decoupling. *J. Magn. Reson., Ser. A*, 115(2):273–276, 1995. ISSN 10641858. doi: 10.1006/jmra.1995.1179.

[13] Eriks Kupce and Ray Freeman. Stretched Adiabatic Pulses for Broadband Spin Inversion. *J. Magn. Reson., Ser. A*, 117(2):246–256, 1995. ISSN 10641858. doi: 10.1006/jmra.1995.0750.

[14] Hyeon Jeong Lee, Brigita Darminto, Sudarshan Narayanan, Maria Diaz-Lopez, Albert W. Xiao, Yvonne Chart, Ji Hoon Lee, James A. Dawson, and Mauro Pasta. Li-ion conductivity in Li2OHCl1-xBrx solid electrolytes: grains, grain boundaries and interfaces. *J. Mater. Chem. A*, 10(21):11574–11586, 4 2022. ISSN 20507496. doi: 10.1039/d2ta01462a.

[15] Kenneth J.D. MacKenzie and Mark E. Smith. Multinuclear Solid-State NMR of Inorganic Materials. In *Pergamon Materials Series*, volume 6. Pergamon, 2002. ISBN 9780080537108.

[16] Emily Milan and Mauro Pasta. The role of grain boundaries in solid-state Li-metal batteries. *Mater. Futures*, 2(1):013501, 3 2023. doi: 10.1088/2752-5724/aca703.

[17] Sudarshan Narayanan, Ulderico Ulissi, Joshua S. Gibson, Yvonne A. Chart, Robert S. Weatherup, and Mauro Pasta. Effect of current density on the solid electrolyte interphase formation at the lithium|Li6PS5Cl interface. *Nature Communications*, 13(1), 12 2022. ISSN 20411723. doi: 10.1038/s41467-022-34855-9.

[18] Han Nguyen, Sunny Hy, Erik Wu, Zhi Deng, Mojtaba Samiee, Thomas Yersak, Jian Luo, Shyue Ping Ong, and Ying Shirley Meng. Experimental and Computational Evaluation of a Sodium-Rich Anti-Perovskite for Solid State Electrolytes. *J. Electrochem. Soc.*, 163(10):A2165–A2171, 2016. ISSN 0013-4651. doi: 10.1149/2.0091610jes.

[19] Svenja K. Otto, Luise M. Riegger, Till Fuchs, Sven Kayser, Pascal Schweitzer, Simon Burkhardt, Anja Henss, and Jürgen Janek. In Situ Investigation of Lithium Metal–Solid Electrolyte Anode Interfaces with ToF-SIMS. *Advanced Materials Interfaces*, 9(13), 5 2022. ISSN 21967350. doi: 10.1002/admi.202102387.

[20] Tan Lien Pham, Abdus Samad, Hye Jung Kim, and Young Han Shin. Computational predictions of stable phase for antiperovskite Na 3 OCl via tilting of Na6O octahedra. *Journal of Applied Physics*, 124(16), 10 2018. ISSN 10897550. doi: 10.1063/1.5047833.

[21] James A. Quirk and James A. Dawson. Design Principles for Grain Boundaries in Solid-State Lithium-Ion Conductors. *Adv. Energy Mater.*, 13(32):2301114, 8 2023. ISSN 1614-6832. doi: 10.1002/aenm.202301114. URL `https://onlinelibrary.wiley.com/doi/10.1002/aenm.202301114`.

[22] Tammo K. Schwietert, Violetta A. Arszelewska, Chao Wang, Chuang Yu, Alexan-

dros Vasileiadis, Niek J.J. de Klerk, Jart Hageman, Thomas Hupfer, Ingo Kerkamm, Yaolin Xu, Eveline van der Maas, Erik M. Kelder, Swapna Ganapathy, and Marnix Wagemaker. Clarifying the relationship between redox activity and electrochemical stability in solid electrolytes. *Nature Materials*, 19(4):428–435, 4 2020. ISSN 14764660. doi: 10.1038/s41563-019-0576-0.

[23] David S. Smith, Pierre Lefeuvre, Maxence Renaux, Benoit Nait-Ali, and Anne Leriche. Study of neck formation and densification in porous hydroxyapatite ceramics using thermal conductivity measurements. *Open Ceramics*, 13, 3 2023. ISSN 26665395. doi: 10.1016/j.oceram.2023.100329.

[24] Yulong Sun, Yuechao Wang, Xinmiao Liang, Yuanhua Xia, Linfeng Peng, Huanhuan Jia, Hanxiao Li, Liangfei Bai, Jiwen Feng, Hong Jiang, and Jia Xie. Rotational Cluster Anion Enabling Superionic Conductivity in Sodium-Rich Antiperovskite Na3OBH4. *J. Am. Chem. Soc.*, 141(14):5640–5644, 2019. ISSN 15205126. doi: 10.1021/jacs.9b01746.

[25] Ping Chun Tsai, Sunil Mair, Jeffrey Smith, David M. Halat, Po Hsiu Chien, Kwangnam Kim, Duhan Zhang, Yiliang Li, Liang Yin, Jue Liu, Saul H. Lapidus, Jeffrey A. Reimer, Nitash P. Balsara, Donald J. Siegel, and Yet Ming Chiang. Double Paddle-Wheel Enhanced Sodium Ion Conduction in an Antiperovskite Solid Electrolyte. *Adv. Energy Mater.*, 13(7):2203284, 2 2023. ISSN 16146840. doi: 10.1002/aenm.202203284.

[26] Michael J. Wang, Jeffrey B. Wolfenstine, and Jeff Sakamoto. Mixed Electronic and

Ionic Conduction Properties of Lithium Lanthanum Titanate. *Advanced Functional Materials*, 30(10), 3 2020. ISSN 16163028. doi: 10.1002/adfm.201909140.

[27] Xinxin Wang, Jingjing Chen, Zhiyong Mao, and Dajian Wang. Effective resistance to dendrite growth of NASICON solid electrolyte with lower electronic conductivity. *Chemical Engineering Journal*, 427, 1 2022. ISSN 13858947. doi: 10.1016/j.cej.2021.130899.

[28] Xinxin Wang, Wentao Mei, Jingjing Chen, Dajian Wang, and Zhiyong Mao. Rare Earth Oxide-Assisted Sintered NASICON Electrolyte Composed of a Phosphate Grain Boundary Phase with Low Electronic Conductivity. *ACS Applied Energy Materials*, 5(1):777–783, 1 2022. ISSN 25740962. doi: 10.1021/acsaem.1c03254.

[29] Yonggang Wang, Qingfei Wang, Zhenpu Liu, Zhengyang Zhou, Shuai Li, Jinlong Zhu, Ruqiang Zou, Yingxia Wang, Jianhua Lin, and Yusheng Zhao. Structural manipulation approaches towards enhanced sodium ionic conductivity in Na-rich antiperovskites. *J. Power Sources*, 293:735–740, 2015. ISSN 03787753. doi: 10.1016/j.jpowsour.2015.06.002. URL `http://dx.doi.org/10.1016/j.jpowsour.2015.06.002`.

[30] Sebastian Wenzel, Stefan J. Sedlmaier, Christian Dietrich, Wolfgang G. Zeier, and Juergen Janek. Interfacial reactivity and interphase growth of argyrodite solid electrolytes at lithium metal electrodes. *Solid State Ionics*, 318:102–112, 5 2018. ISSN 01672738. doi: 10.1016/j.ssi.2017.07.005.

[31] Wei Xia, Yang Zhao, Feipeng Zhao, Keegan Adair, Ruo Zhao, Shuai Li, Ruqiang Zou, Yusheng Zhao, and Xueliang Sun. Antiperovskite Electrolytes for Solid-State

Batteries. *Chemical Reviews*, 122(3):3763–3819, 2 2022. ISSN 15206890. doi: 10.1021/acs.chemrev.1c00594.

[32] Yuran Yu, Zhuo Wang, and Guosheng Shao. Theoretical tuning of Ruddlesden-Popper type anti-perovskite phases as superb ion conductors and cathodes for solid sodium ion batteries. *Journal of Materials Chemistry A*, 7(17):10483–10493, 2019. ISSN 20507496. doi: 10.1039/c9ta02166c.

[33] Jingfeng Zheng, Brian Perry, and Yiying Wu. Antiperovskite Superionic Conductors: A Critical Review. *ACS Mater. Au*, 1(2):92–106, 2021. ISSN 26942461. doi: 10.1021/acsmaterialsau.1c00026.

[34] Jinlong Zhu, Shuai Li, Yi Zhang, John W Howard, Xujie Lü, Yutao Li, Yonggang Wang, Ravhi S Kumar, Liping Wang, and Yusheng Zhao. Enhanced ionic conductivity with Li7O2Br3 phase in Li3OBr anti-perovskite solid electrolyte. *Appl. Phys. Lett.*, 109(10):101904, 9 2016. ISSN 0003-6951. doi: 10.1063/1.4962437. URL `https://doi.org/10.1063/1.4962437`.

4 | On the Origin of Non-Arrhenius Ionic Conductivity in Na_3OBr

A significant proportion of the work reported in this chapter is included in the manuscript submitted to Angewandte Chemie:

Brigita Darminto, Gregory J. Rees, John Cattermull, Kenjiro Hashi, Maria Diaz-Lopez, Naoaki Kuwata, Stephen J. Turrell, Emily Milan, Yvonne Chart, Camilla di Mino, Hyeon Jeong Lee, Andrew L. Goodwin, and Mauro Pasta. On the Origin of Non-Arrhenius Na-ion Conductivity in Na_3OBr.

4.1 Introduction

Non-Arrhenius ionic conductivity behaviour resulting in a decrease in activation energy for ion conduction above $250\,^{\circ}\mathrm{C}$ has been observed across different antiperovskites compositions (Li, K, and Na) [34, 30, 8, 17, 11, 22, 7, 32]. However, the origin of this behaviour is not yet well understood. For antiperovskite compositions with cluster anions like $Na_2(NH_2)(BH_4)$, deviation from Arrhenius behaviour is often assigned to correlated motion between the cluster anion rotations and the translating cation, also known as the paddlewheel effect. On the other hand, for the compositions with single halide anions, such behaviour is usually attributed to structural instability, which includes phase transitions, order-disorder transitions of the ion sublattice, and crystal melting. The non-Arrhenius ionic conductivity behaviour has been reported experimentally by Zhu et al. [35]. Dawson et al. performed molecular dynamics calculations on Na_3OB (B = Cl or

Br) with an alkali-halide partial Schottky defect concentration of $\delta = 0.038$ and did not observe any deviations from Arrhenius behaviour in their ionic conductivities at elevated temperatures [4]. These differences raise questions about whether this behaviour is intrinsic to Na_3OBr and why it has only been observed experimentally so far. The fact that this transition occurs at a relatively low temperature, $250\,^{\circ}\mathrm{C}$, makes it viable for us to perform in-situ structural characterisations before and after the transition. Through a combination of DSC, EIS, NMR, in-situ XRD, and PDF, this study reveals that the non-Arrhenius ionic conductivity behaviour in Na_3OBr does not originate from a melting or order-disorder transition in Na_3OBr itself as previously speculated. Instead, it originates from poorly crystalline impurities, which are not detectable by XRD alone. These findings improve understanding of the processing-structure-properties relationships pertaining to NaRAPs and highlight the need to determine these relationships in other materials systems.

4.2 Experimental

4.2.1 Synthesis of Na_3OBr

Na_3OBr was synthesised from sodium oxide (Sigma Aldrich, 80% Na_2O and 20% Na_2O_2) and sodium bromide (Sigma Aldrich, 99% NaBr) via a two-step solid-state reaction. Prior to the synthesis, both reagents used were dried at $120\,^{\circ}\mathrm{C}$ for 12 h in a glass vacuum oven (Buchi). Sodium oxide and sodium bromide were then loaded into a 45 ml ZrO_2 milling jar containing ten 5 mm diameter and five 10 mm diameter ZrO_2 balls. A planetary ball mill (Fritsch Puverisette 7 Premium) was used at 350 rpm for a total effective milling time of 10 hours with a 5-minute pause for every 10 minutes of milling. Subsequently,

the ball-milled powder was heated in a 15 ml cylindrical alumina crucible at $450\,^{\circ}\mathrm{C}$ for 24 hours and left to cool down to room temperature inside the muffle furnace. To form the sample for ionic conductivity measurement, Na_3OBr was ground to powder and pressed into a 5 mm diameter cylindrical polyether ether ketone (PEEK) cell at 370 MPa for 3 minutes. The final thickness of the pellet was around $300\,\mu\mathrm{m}$.

4.2.2 Differential Scanning Calorimetry (DSC)

The DSC instrument was operated in air, so the sample was sealed in an aluminium hermetic pan inside the glovebox prior to the measurement to protect it from moisture. Measurements were performed between 25 and $300\,^{\circ}\mathrm{C}$ with a heating rate of $5\,^{\circ}\mathrm{C\,min^{-1}}$.

4.2.3 Electrochemical Impedance Spectroscopy (EIS)

The EIS characterisation was carried out in a custom-built PEEK solid-state cell using gold powder (Alfa Aesar, gold powder, spherical, APS 0.5 – $0.8\,\mu\mathrm{m}$) as the blocking electrodes [5]. Gold powder was added to one side of the cold-pressed pellet and then pressed at 370 MPa for 3 minutes before turning the pellet over to perform the same procedure on the opposite side. Using a screw on top of the cell, a uniaxial pressure of $\approx$ 70 MPa was applied during the measurements. The cell was then heated inside a muffle furnace in a glovebox for an hour at each data point before a measurement was performed using a two-probe configuration to a BioLogic MTZ35 frequency response analyser. Potentiostatic EIS (PEIS) measurements were conducted in the frequency range of 35 MHz to 0.1 Hz with a voltage amplitude of 10 mV. ZView software was used to simulate Nyquist plots based on the equivalent circuit depicted in Figure 4.1b.

4.2.4 Ex-situ Scanning Electron Microscopy (SEM)

SEM measurements were conducted using a Thermo-Fisher Helios G4-CXe Plasma FIB (PFIB) instrument with energy dispersive X-ray spectroscopy (EDX) functionality (Oxford Instruments). Both cold pressed (CP) and hot pressed (HP) pellets were mounted on a transportable SEM stage with carbon tape inside an Ar-filled glovebox before sealing in a Gatan iLoad sample transfer vessel. A trench from the top surface of about $50\,\mu\mathrm{m}$ was milled using the Xe-ion beam. Since the FIB column was at a 52° angle to the SEM column, the sample must be tilted to this angle for milling and imaging of the cross-section.

4.2.5 X-ray Diffraction (XRD)

Ex-situ X-ray powder diffraction measurements were performed on the as-synthesised Na_3OBr powder using a Rigaku Smartlab diffractometer (Cu Kα) to assess its phase purity. Synchrotron XRD measurements were performed on the I11 beamline of the Diamond Light Source operating with an X-ray wavelength of $0.825\,318\,\text{Å}$. Diffraction patterns were collected in capillary transmission geometry using the Mythen2 Position Sensitive Detector, two data collections of 5 seconds each were taken at angles 0.25 degrees apart, and then summed to account for gaps in the detector coverage. Over the temperature range of 25 to $300\,^{\circ}\mathrm{C}$, patterns were collected at approximately $2.5\,^{\circ}\mathrm{C}$ intervals with a continuous heating rate of $6\,^{\circ}\mathrm{C min}^{-1}$ using an FMB Oxford cyberstar hot air blower. All Rietveld refinements were carried out using the TOPAS-Academic software [2]. In total, 20 parameters were refined: 11 polynomial function parameters to fit the background, the lattice parameter, b_{eq} Na, b_{eq} Br, b_{eq} O, the scale parameter, and the 4 peak shape function parameters (pku, pkv, pkw, and pky).

Total scattering data were collected at I15-1 beamline at Diamond Light Source operating with an X-ray wavelength of $0.161\,669\,\text{Å}$. Samples were put in $1\,\text{mm}$ borosilicate glass capillaries. Data for both background containers and samples were collected in a Q range 0.3 - 25 A^{-1} in a temperature range from 150 to $300\,^{\circ}\text{C}$ in $5\,^{\circ}\text{C}$ intervals. GudrunX routines were employed to subtract empty containers, Compton scattering and absorption from the data, and to normalise them via Krogh-Moe & Norman normalisation [14, 25, 29].

4.2.6 Nuclear Magnetic Resonance (NMR) Spectroscopy

NMR measurements were performed at room temperature and at variable temperatures. All the room temperature ^{23}Na static solid-state NMR measurements were completed at magnetic field strengths of 20 T (ν_0 ^{23}Na = 264.6 MHz) and 23.5 T (ν_0 ^{23}Na = 224.9 MHz) using Bruker Neo consoles and 3.2 mm probes. The spectra were referenced to NaCl at 7.2 ppm [21], and were recorded using a Hahn echo (π/2 - τ - π - τ) sequence with 400 kHz WURST (wideband, uniform rate, smooth truncation) excitation and refocussing pulses for broadband excitation of the $\approx$ 220 kHz wide resonances (at 20 T) [16, 15]. High-resolution MAS NMR (MAS, ν_R = 20 kHz) was also performed to deconvolute impurity resonances into three components: Na_2O_2, Na_2O, and NaOH. The variable temperature NMR measurements were done at the National Institute for Materials Science (NIMS) using an ECA-500 (JEOL, Japan) spectrometer and a homemade probe [10]. The sample was packed into a quartz NMR tube SP-405 (SHIGEMI, Japan) and sealed in an Ar-filled globe box. The resonance frequency of ^{23}Na was 132.32 MHz. The chemical shift was referenced to the 1.0 M NaCl solution at 0 ppm. The temperature

was controlled by a nitrogen gas flow.

4.3 Results and Discussion

We synthesised Na_3OBr with commercially available Na_2O, which contains $\approx 80\%$ Na_2O and $\approx 20\%$ Na_2O_2. The significant amount of Na_2O_2 was taken into account in the precursor ratio calculation, as seen in the equation below.

$$0.8\mathrm{Na_2O} + 0.2\mathrm{Na_2O_2} + \mathrm{NaBr} \rightarrow \mathrm{Na_3OBr} + 0.1\mathrm{O_2} \tag{4.1}$$

A combination of high-energy ball milling and subsequent heating is expected to decompose Na_2O_2 into Na_2O and O_2. This synthesis procedure has been reported multiple times in the literature and led to the successful formation of NaRAPs [24, 30]. Differential scanning calorimetry (DSC) was performed to study the thermal behaviour of the Na_3OBr, also shown in Figure 4.1a. Upon heating, an endothermic peak was observed with an onset at $247\,^{\circ}\mathrm{C}$ and maximum at $258\,^{\circ}\mathrm{C}$. Previous studies on Li, Na and K antiperovskites also showed similar endothermic peaks (K_3OI: $245\,^{\circ}\mathrm{C}$, Li_2OHBr: $254\,^{\circ}\mathrm{C}$, Na_3OBr: $255\,^{\circ}\mathrm{C}$, and Na_3OCl: $191\,^{\circ}\mathrm{C}$). Some studies attributed these peaks to the melting of the antiperovskite phases and others to anion disordering [18, 34, 30, 17]. Except for this peak, no other peaks were observed in the DSC plot during heating to $300\,^{\circ}\mathrm{C}$. Additionally, the bulk material remains solid up to $300\,^{\circ}\mathrm{C}$, which is confirmed by variable temperature synchrotron XRD, Figure 4.2b, meaning that the peak does not correspond to the melting of Na_3OBr.

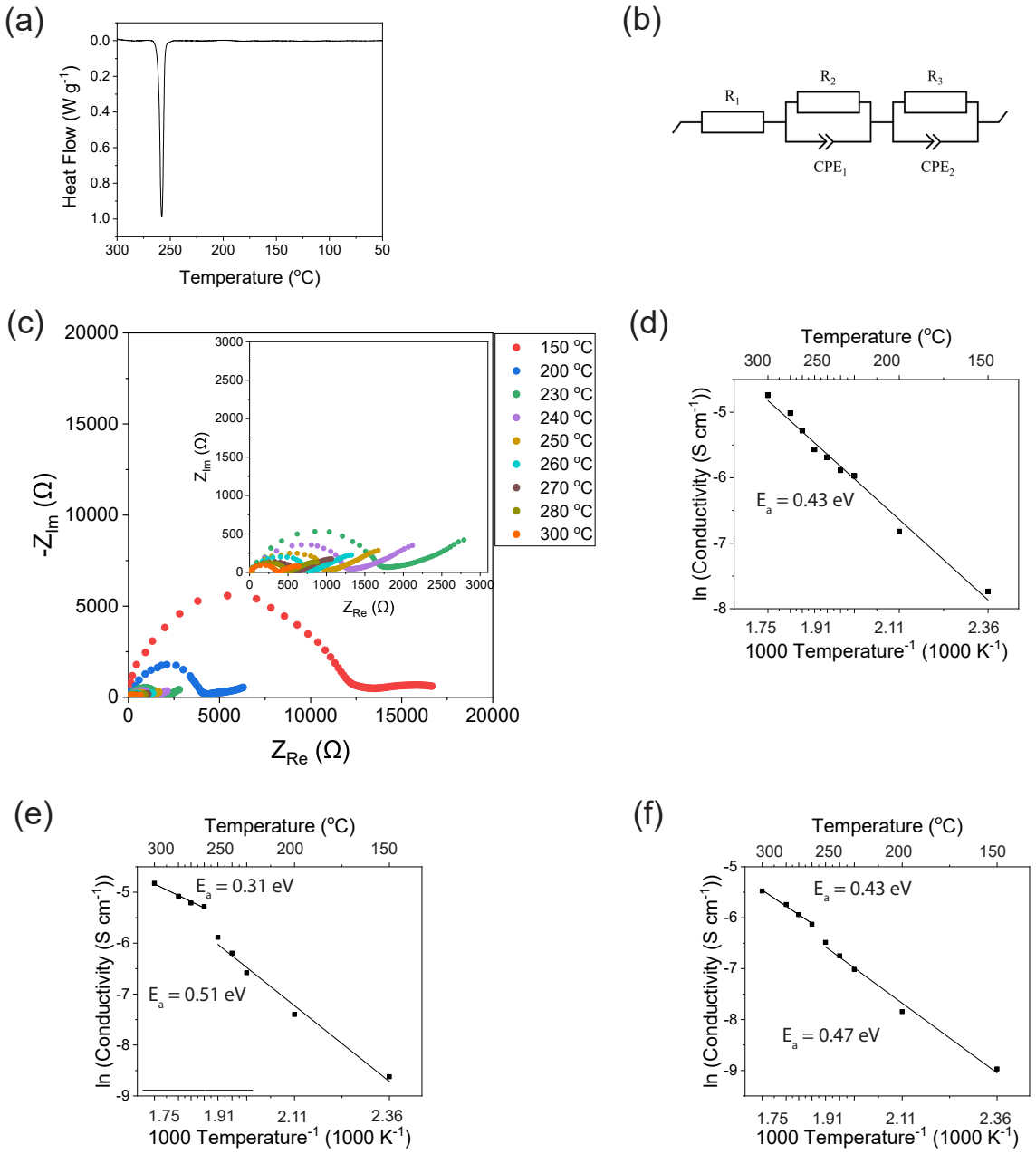

Figure 4.1: In-house characterisations of as-synthesised Na_3OBr. (a) DSC of Na_3OBr showing an endothermic peak with an onset at 247 °C. (b) An equivalent circuit was used to simulate our experimental setup. R_1 is the instrument cabling or electric contact resistance, R_2 is the bulk resistance, CPE_1 is the bulk capacitance, R_3 is boundary resistance, and CPE_2 is the boundary capacitance. (c) Nyquist plots of Na_3OBr at multiple temperatures between 25 °C and 300 °C. (d) Arrhenius plot of total ionic conductivity of Na_3OBr with a step increase observed at 250 °C. (e) Arrhenius plot of boundary ionic conductivity of Na_3OBr. (f) Arrhenius plot of bulk ionic conductivity of Na_3OBr with a step increase observed at 250 °C.

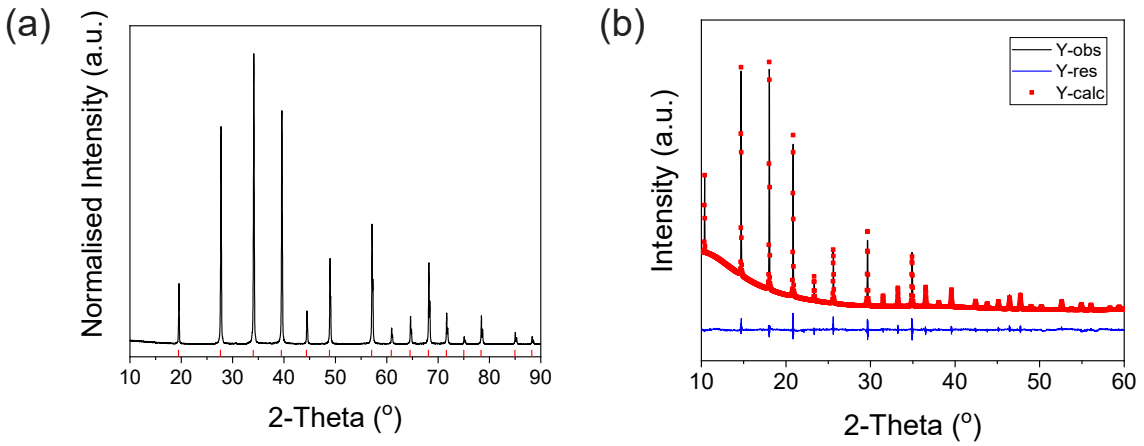

Figure 4.2: (a) Ex-situ X-ray diffractogram taken with Rigaku Smartlab diffractometer (Cu Kα). (b) Rietveld refinement of the room temperature synchrotron X-ray diffractogram of synthesised Na_3OBr with an X-ray wavelength of $0.825\,318$ Å. The black line is the experimental data, the red line is the fit, and the blue line is the difference between them. Experiments with I11 beamline were performed in collaboration with John Cattermull (University of Oxford).

Temperature-dependent potentiostatic electrochemical impedance spectroscopy (PEIS) was used to investigate the effect of temperature on ionic conductivity. A uniaxial pressure of $\approx$ 70 MPa, the maximum pressure that can be endure by the cell, was applied to maintain good contact between gold-blocking electrodes and the Na_3OBr pellet. To determine the relative contributions of the electrolyte bulk and grain boundaries to the total impedance, the setup was modelled as an equivalent circuit shown in Figure 4.1b. R_1 corresponds to instrument cabling or electric contact resistance, R_2 and CPE_1 correspond to the bulk Na^+ conduction, and R_3 and CPE_2 correspond to the conduction through the grain boundaries. The calculated total ionic conductivities are presented in Figure 4.1d. There is a step change in the total ionic conductivity at $250\,^{\circ}\mathrm{C}$, the temperature at which the endothermic peak was observed in the DSC, which corresponds to a reduction of activation energy from $0.47\,\mathrm{eV}$ to $0.43\,\mathrm{eV}$. These activation energies are slightly lower than the reported values (0.52 eV - 1.14 eV), possibly due to the higher pressure applied to

the cell during the measurements [24, 1, 11, 35, 33]. Refinements were performed over variable temperature synchrotron XRD data to elucidate the origin of this phenomenon. The refined parameters can be found in Table 4.1.

Table 4.1: Sequential Rietveld refinement results for Na_3OBr.

Temperature [°C]	R_{wp} [%]	Lattice Parameter [Å]	Lattice Parameter Error [Å]	$b_{eq\text{Na}}$ [a.u.]	$b_{eq\text{Na}}$ Error [a.u.]	$b_{eq\text{Br}}$ [a.u.]	$b_{eq\text{Br}}$ Error [a.u.]
25.5	1.022180	4.561558	0.000021	1.641498	0.054317	1.174098	0.040107
29.5	1.070940	4.562104	0.000022	1.682288	0.057362	1.187506	0.042266
30.2	1.050340	4.562022	0.000022	1.662280	0.056135	1.150041	0.041136
33.8	1.098070	4.562637	0.000023	1.694135	0.059128	1.190575	0.043534
35.8	1.114310	4.562716	0.000023	1.716716	0.060192	1.184791	0.044092
38.6	1.120320	4.563202	0.000023	1.732066	0.060764	1.221527	0.044771
38.9	1.108310	4.563253	0.000023	1.737458	0.060102	1.220345	0.044256
41.8	1.092120	4.563737	0.000023	1.750327	0.059553	1.224984	0.043878
43.4	1.067490	4.564008	0.000022	1.750455	0.058234	1.256517	0.043170
44.6	1.063110	4.563875	0.000022	1.781834	0.058125	1.216448	0.042544
47.8	1.028520	4.564485	0.000022	1.753494	0.056319	1.275530	0.041925
51.7	1.013890	4.565123	0.000021	1.795308	0.055785	1.268658	0.041247
51.9	1.016600	4.564780	0.000021	1.796136	0.055968	1.266525	0.041358
52.3	1.013310	4.564857	0.000021	1.812125	0.055961	1.298888	0.041531
58.3	1.001380	4.565673	0.000021	1.817225	0.055458	1.304760	0.041206
58.2	1.020540	4.565856	0.000022	1.839877	0.056807	1.306292	0.042068
60.2	1.023250	4.566016	0.000022	1.839279	0.056869	1.302573	0.042089
61.4	1.013820	4.566159	0.000021	1.862333	0.056659	1.335295	0.042089
64.4	1.017710	4.566436	0.000022	1.862421	0.056895	1.320784	0.042138
67.2	1.029210	4.566869	0.000022	1.907565	0.057962	1.364860	0.043025
69.8	1.050380	4.567208	0.000022	1.918637	0.059330	1.356367	0.043879
72.3	1.061780	4.567557	0.000023	1.982388	0.060402	1.381109	0.044507
74.7	1.083880	4.567831	0.000023	1.959962	0.061667	1.381132	0.045589
76.4	1.077080	4.568076	0.000023	2.018258	0.061699	1.405451	0.045495
78.0	1.063500	4.568285	0.000023	1.987839	0.060722	1.393819	0.044868
79.7	1.087430	4.568511	0.000023	1.991809	0.062223	1.410599	0.046126
81.4	1.070960	4.568735	0.000023	1.996786	0.061360	1.448284	0.045798
84.2	1.060980	4.569042	0.000023	1.985291	0.060724	1.404863	0.045033
86.8	1.030940	4.569382	0.000022	1.988088	0.059100	1.420591	0.043951
88.3	1.033140	4.569568	0.000022	2.012918	0.059441	1.431820	0.044175
90.8	0.989550	4.569885	0.000021	2.034860	0.057131	1.408760	0.042159
92.6	0.988320	4.570150	0.000021	2.001152	0.057016	1.463944	0.042779
94.4	0.998130	4.570372	0.000021	2.028245	0.057737	1.460003	0.043115
96.6	0.982790	4.570600	0.000021	2.048450	0.056889	1.479915	0.042517
98.3	0.988120	4.570851	0.000021	2.077601	0.057530	1.465690	0.042737
100.4	0.991480	4.571093	0.000021	2.073464	0.057718	1.468326	0.042911
103.1	1.032090	4.571414	0.000022	2.103607	0.060423	1.466802	0.044762
104.4	1.057630	4.571630	0.000023	2.156624	0.062278	1.496599	0.046057
106.8	1.061870	4.571963	0.000023	2.152221	0.062637	1.521886	0.046598
109.3	1.080680	4.572189	0.000023	2.159350	0.063845	1.506895	0.047305
110.9	1.077580	4.572454	0.000023	2.185579	0.063903	1.553296	0.047619
112.5	1.064620	4.572691	0.000023	2.210308	0.063456	1.570515	0.047317
115.3	1.041060	4.572978	0.000023	2.201779	0.061831	1.559007	0.046004
116.6	1.031270	4.573211	0.000022	2.219332	0.061472	1.620377	0.046207

118.6	1.007200	4.573457	0.000022	2.222875	0.060028	1.579716	0.044733
121.0	0.988990	4.573753	0.000021	2.252637	0.059204	1.641707	0.044492
122.9	0.990890	4.573971	0.000021	2.273752	0.059444	1.629130	0.044442
125.0	0.987780	4.574221	0.000021	2.254900	0.059154	1.608957	0.044163
126.8	0.993050	4.574459	0.000021	2.296747	0.059633	1.641235	0.044565
128.9	1.027150	4.574727	0.000022	2.297713	0.061918	1.665525	0.046532
131.1	1.015570	4.574989	0.000022	2.298631	0.061334	1.640609	0.045871
133.1	1.034150	4.575227	0.000022	2.329541	0.062585	1.671565	0.046918
135.2	1.022070	4.575517	0.000022	2.308294	0.061683	1.642435	0.046091
137.2	1.023730	4.575796	0.000022	2.317716	0.061950	1.676293	0.046595
139.2	1.036420	4.576055	0.000022	2.360809	0.062999	1.672897	0.047104
141.2	1.034220	4.576293	0.000022	2.361023	0.062923	1.696987	0.047271
143.1	1.022480	4.576563	0.000022	2.360733	0.062183	1.728142	0.047037
145.1	1.011270	4.576754	0.000022	2.341543	0.061352	1.721708	0.046439
146.9	1.009480	4.577040	0.000022	2.367194	0.061458	1.748641	0.046629
148.4	1.006580	4.577217	0.000022	2.370490	0.061171	1.715567	0.046076
151.8	1.003750	4.577588	0.000021	2.448178	0.061545	1.761531	0.046329
154.0	0.993770	4.577950	0.000021	2.398722	0.060709	1.785453	0.046180
154.5	0.991880	4.578001	0.000021	2.434332	0.060710	1.761441	0.045762
157.3	0.985480	4.578329	0.000021	2.478667	0.060582	1.812169	0.045855
159.6	0.986930	4.578645	0.000021	2.482958	0.060621	1.794336	0.045616
161.4	1.007770	4.578885	0.000021	2.510194	0.061953	1.795025	0.046451
163.4	1.021090	4.579125	0.000022	2.473405	0.062471	1.837628	0.047459
165.2	1.013610	4.579364	0.000021	2.539701	0.062461	1.819217	0.046861
167.3	1.039610	4.579648	0.000022	2.552492	0.064046	1.878824	0.048528
169.5	1.054850	4.579905	0.000022	2.562635	0.064998	1.880689	0.049135
171.5	1.050240	4.580157	0.000022	2.571787	0.064761	1.864617	0.048773
173.7	1.057460	4.580451	0.000022	2.584111	0.065234	1.875047	0.049143
175.7	1.042650	4.580703	0.000022	2.556035	0.064116	1.869714	0.048404
178.1	1.025750	4.580968	0.000021	2.610686	0.063316	1.885098	0.047598
179.4	1.017140	4.581205	0.000021	2.609457	0.062621	1.873848	0.046968
181.7	0.985880	4.581470	0.000020	2.613781	0.060620	1.913848	0.045783
183.7	0.995620	4.581754	0.000020	2.620119	0.061023	1.909545	0.045964
186.0	0.973780	4.581984	0.000019	2.615288	0.059686	1.911499	0.045012
188.1	0.968700	4.582286	0.000019	2.658527	0.059461	1.927788	0.044740
190.2	0.982530	4.582515	0.000019	2.588594	0.059801	1.937567	0.045424
192.2	0.985210	4.582799	0.000019	2.646039	0.060269	1.985564	0.045880
193.8	1.013680	4.582987	0.000020	2.619018	0.061787	1.965825	0.047041
196.1	1.014770	4.583288	0.000020	2.603069	0.061788	1.963376	0.047094
198.1	1.040380	4.583514	0.000020	2.693667	0.063931	2.029609	0.048776
200.1	1.038740	4.583796	0.000020	2.673244	0.063567	1.999470	0.048299
202.0	1.056670	4.584052	0.000020	2.685271	0.064611	1.989251	0.048898
204.2	1.061900	4.584290	0.000020	2.686281	0.064846	2.002083	0.049183
206.1	1.083280	4.584578	0.000021	2.740929	0.066519	2.040210	0.050439
208.2	1.090290	4.584827	0.000021	2.735744	0.066869	2.059365	0.050909
210.3	1.084280	4.585079	0.000020	2.702444	0.066143	2.057508	0.050513
212.3	1.069260	4.585349	0.000020	2.744731	0.065509	2.092230	0.050101
214.2	1.060950	4.585572	0.000020	2.743554	0.065141	2.089594	0.049796
216.0	1.045690	4.585801	0.000019	2.794755	0.064405	2.096600	0.048976
218.5	1.034440	4.586084	0.000019	2.756536	0.063582	2.138155	0.048982
220.5	1.041130	4.586398	0.000019	2.806801	0.064248	2.098070	0.048809
222.5	1.037340	4.586572	0.000019	2.789912	0.063800	2.083386	0.048403
224.6	1.040320	4.586841	0.000019	2.780892	0.063946	2.103771	0.048772
226.3	1.061310	4.587078	0.000019	2.806082	0.065435	2.141556	0.050117
228.3	1.091800	4.587373	0.000020	2.846150	0.067408	2.120600	0.051161
230.5	1.099650	4.587600	0.000020	2.815234	0.067693	2.119831	0.051526

232.5	1.141310	4.587902	0.000021	2.897480	0.070990	2.155864	0.053885
234.9	1.147290	4.588162	0.000021	2.875962	0.071099	2.150777	0.053998
236.8	1.176220	4.588433	0.000021	2.873062	0.072970	2.155952	0.055505
238.6	1.197310	4.588650	0.000021	2.903616	0.074477	2.151803	0.056377
240.6	1.206460	4.588896	0.000022	2.882066	0.075014	2.171504	0.057174
242.6	1.221840	4.589165	0.000022	2.894738	0.075894	2.166150	0.057696
244.4	1.222980	4.589366	0.000022	2.900281	0.076217	2.275002	0.059139
245.8	1.230040	4.589569	0.000022	2.876689	0.076683	2.261530	0.059513
248.6	1.230160	4.589858	0.000022	2.933898	0.077337	2.277839	0.059834
250.5	1.200720	4.590165	0.000021	2.912927	0.075510	2.352056	0.059328
252.8	1.156960	4.590476	0.000020	2.841799	0.072095	2.345049	0.056969
254.9	1.135160	4.590752	0.000020	2.821947	0.070565	2.328832	0.055701
256.9	1.098570	4.590995	0.000019	2.888071	0.069072	2.344901	0.054278
259.0	1.082420	4.591258	0.000019	3.011485	0.069507	2.350454	0.053834
261.1	1.117160	4.591526	0.000020	3.009343	0.072207	2.293061	0.055358
263.2	1.166300	4.591792	0.000021	3.046364	0.075439	2.293431	0.057570
265.3	1.211210	4.592066	0.000022	3.026213	0.078456	2.321632	0.060367
267.3	1.255630	4.592346	0.000023	3.091264	0.082218	2.351029	0.063174
269.1	1.304030	4.592608	0.000024	3.105611	0.085627	2.364193	0.065871
271.4	1.388870	4.592924	0.000025	3.058499	0.090824	2.401381	0.070793
273.3	1.386770	4.593128	0.000025	3.045875	0.090579	2.424539	0.071043
275.2	1.405770	4.593409	0.000026	3.058407	0.092279	2.363007	0.071475
277.1	1.398620	4.593680	0.000026	3.107752	0.092495	2.398858	0.071712
279.2	1.389660	4.593939	0.000026	3.082468	0.091760	2.390384	0.071265
281.3	1.369710	4.594217	0.000025	3.063352	0.090504	2.429325	0.071050
283.2	1.315440	4.594514	0.000024	3.150048	0.087579	2.478143	0.068665
285.2	1.304750	4.594806	0.000024	3.072160	0.086283	2.480365	0.068394
287.3	1.247850	4.595054	0.000022	3.032978	0.082044	2.487612	0.065414
289.3	1.211410	4.595335	0.000022	3.041706	0.079564	2.538582	0.064003
291.4	1.155430	4.595616	0.000021	3.094840	0.076691	2.595872	0.062017
293.4	1.129980	4.595879	0.000020	3.021956	0.074948	2.559139	0.060726
295.4	1.119240	4.596141	0.000020	3.010138	0.074370	2.549830	0.060205
297.4	1.139960	4.596422	0.000021	3.063871	0.076676	2.537890	0.061542
299.3	1.176820	4.596691	0.000022	3.091901	0.079723	2.486193	0.063171
300.4	1.196080	4.596833	0.000022	3.159427	0.081841	2.488018	0.064368

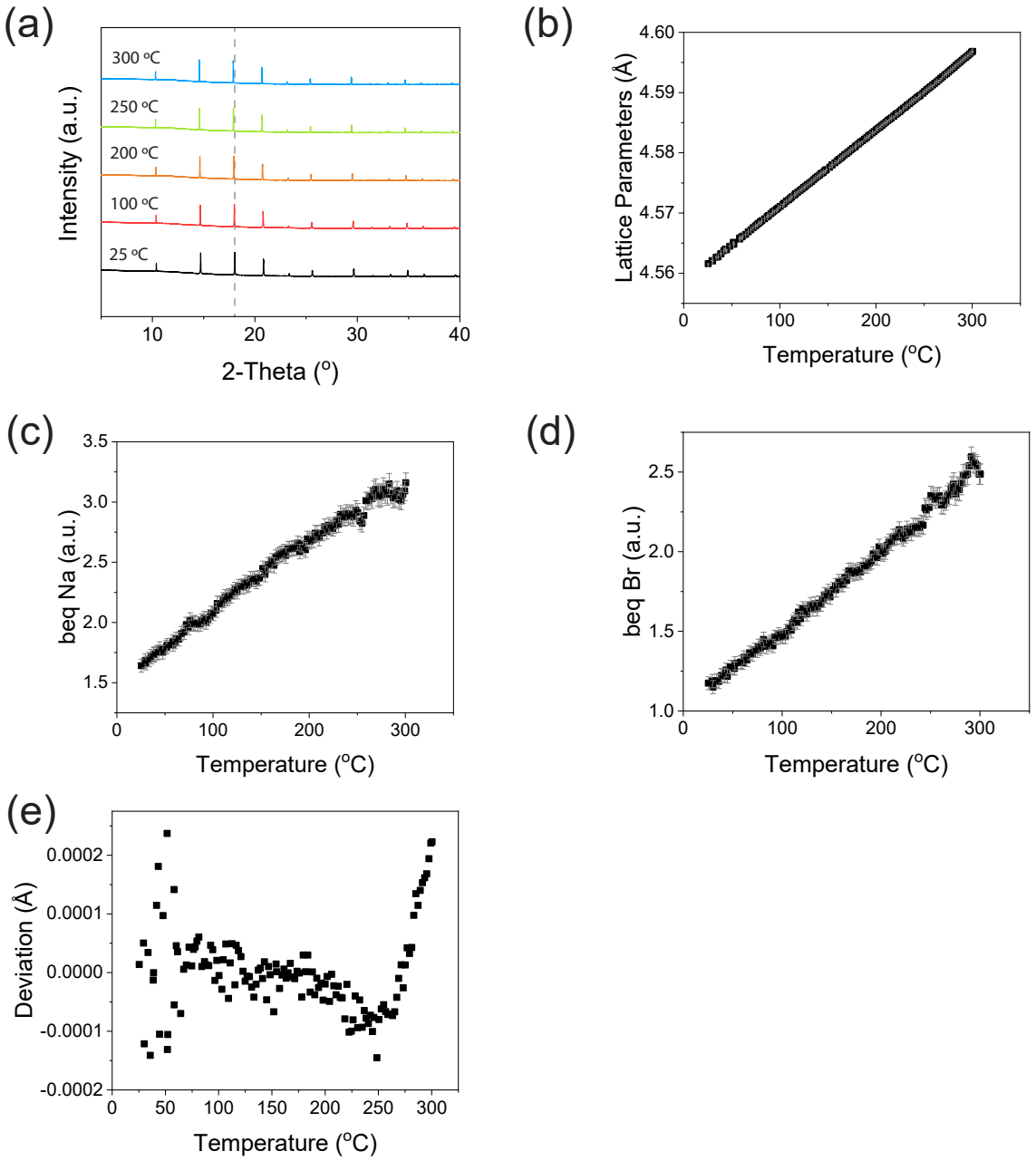

Figure 4.3: (a) Variable temperature synchrotron X-ray experiment with an X-ray wavelength of 0.825 318 Å. Sequential Rietveld refinements were performed on the variable temperature data, and the changes in (b) lattice parameter, (c) thermal parameter of Na (b_{eq} Na), and (d) thermal parameter of Br (b_{eq} Br) of Na_3OBr are plotted as a function of temperature. These show thermal expansion with no presence of crystalline deviation. (e) Deviation of the lattice parameter of Na_3OBr from a linear trendline as a function of temperature. Experiments with I11 beamline were performed in collaboration with John Cattermull (University of Oxford).

Prior to synchrotron XRD measurement, an ex-situ X-ray powder diffraction measure-

ment was performed on the as-synthesised Na_3OBr powder using a Rigaku Smartlab diffractometer (Cu Kα) to assess its phase purity. In agreement with previous reports, the room temperature (RT) synchrotron XRD pattern was fitted to the cubic space group $Pm\bar{3}m$ with a unit cell of a = $4.562(6)$ Å, using a Rietveld refinement ($R_{wp} = 1.02\,\%$). No Bragg peaks other than those which belong to the Na_3OBr are present in the diffraction pattern, thus no other crystalline species are present at significant concentrations in our sample. To understand how the crystal structure evolves with temperature, sequential Rietveld refinements were performed on the synchrotron XRD data between RT and $300\,^{\circ}\mathrm{C}$, with a step size of $2.5\,^{\circ}\mathrm{C}$. Any sign of discontinuity in the lattice parameter and elemental thermal parameters (b_{eq}) could give an indication of an order to disorder transition. The intensities of the Na_3OBr peaks do not change drastically above $247\,^{\circ}\mathrm{C}$, hence the Na_3OBr powder did not melt. The Bragg peak positions shift to lower angles due to thermal expansion of the Na_3OBr lattice, but the rate of change in lattice parameter is constant with temperature, even above $267\,^{\circ}\mathrm{C}$ where the endothermic peak ends, as seen in Figure 4.3b. When fitted with a straight line, the deviation of each point from the fit can be plotted (Figure 4.3e). A change in the deviation trend above $247\,^{\circ}\mathrm{C}$ was observed; however, the deviations are of the order of 10^{-4} Å, making them negligible compared to the size of any atom in the structure. Out of the three elements contained in our sample, we decided to focus our attention on the thermal parameters of Na and Br. This is because the thermal parameters of O have significant error bars (10 - 20 %) due to O being the weakest X-ray scatterer of the three. The thermal parameter of Na (Figure 4.3c) was found to be higher than that of Br (Figure 4.3d), but in both cases the changes are only very small ($\approx 1\%$) around $250\,^{\circ}\mathrm{C}$. So, just as there is no evidence for abrupt behaviour

in the lattice parameter variation, neither is there any sign in atomic displacements of discontinuous behaviour across the temperature range studied.

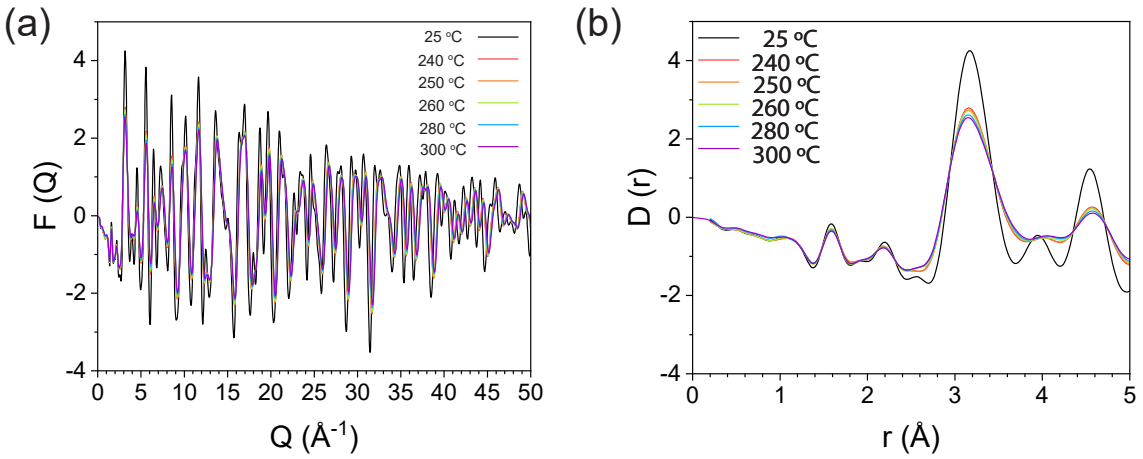

Figure 4.4: (a) X-ray total structure factor *F(Q)* of Na_3OBr. Measurement was done with an X-ray wavelength of $0.161\,669$ Å. (b) Differential correlation function *D(r)* calculated from experimental X-ray total structure factor *F(Q)*. Experiments with I15-1 beamline were performed in collaboration with Dr. Maria Diaz-Lopez (Diamond Light Source).

In order to investigate the local structure of Na_3OBr, we looked at the pair distribution function (PDF) in the range of 0 Å to 5 Å(Figure 4.4b). The majority of the peak positions shift to higher distances while the widths broaden as the temperature increases. This behaviour can be attributed to thermal expansion and the thermal population of phonons. We note that an order-disorder transition and a phase change (melting of Na_3OBr) are absent in this temperature range. From this synchrotron XRD study, we can deduce that the endothermic peak in the DSC and the non-Arrhenius behaviour of the ionic conductivity arise from neither the melting of Na_3OBr nor an order-disorder transition.

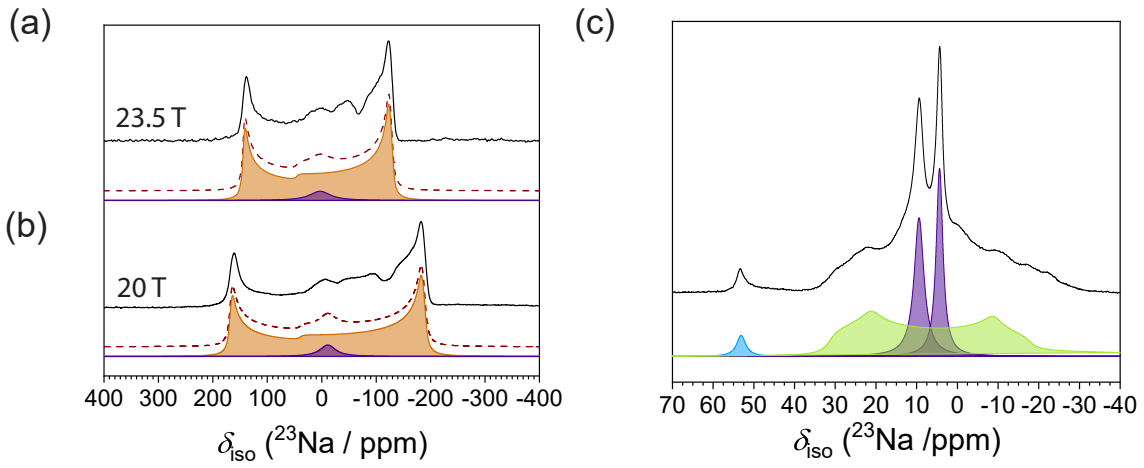

Figure 4.5: The room temperature ^{23}Na static WURST-echo NMR spectra (black) of Na_3OBr at (a) 23.5 T (ν_0 = 264.6 MHz) and (b) 20 T (ν_0 = 224.9 MHz). (c) High-resolution MAS NMR (MAS, ν_R = 20 kHz) of the sample; impurity resonances were deconvoluted into three components: Na_2O_2 (purple), Na_2O (blue), and NaOH (green). NMR experiments were performed in collaboration with Dr. Gregory J. Rees (University of Oxford).

Having excluded Na_3OBr melting and order-disorder transition as the potential origin of non-Arrhenius behaviour, we probed the local Na environment by static ^{23}Na NMR spectroscopy. The spectra in Figure 4.5a show two components, a broad (136 kHz at 11.7 T, 80 kHz at 23.5 T) quadrupolar peak and a narrower component at $\approx$ 0 ppm (shown in purple), which arises from impurities. The wideline Na_3OBr (orange) is deconvoluted to give δ_{iso} = 44 ppm, X_Q = 11.9 MHz and η_Q = 0, which are similar to the reported values for Na_3OCl [13]. The large quadrupolar peak arises from the non-symmetric octahedral coordination of Na ions with two O ions and four coplanar Br ions. Solid-state ^{23}Na magic angle spinning (MAS, ν_R = 20 kHz) NMR was performed to improve the resolution and deconvolute the narrower component shown in Figure 4.5a and Figure 4.5b. The ^{23}Na MAS spectrum shows two Na_2O_2 resonances (purple at 9.5 and 4.5 ppm), a minor Na_2O resonance (blue at 53 ppm), and a broader quadrupole resonance attributed to NaOH (green at 38.5 ppm), shown in Figure 4.5c. The isotropic shift of the attributed

NaOH resonance is at a higher frequency than previous work published on NaOH (21 ppm) [21]. However, the quadrupole coupling constant (C_Q = 3.8 MHz) is similar to that of NaOH. This discrepancy in shift could be due to the lack of periodicity, as the NaOH will be neighbouring Na_3OBr, Na_2O_2 and Na_2O in the mixture. The total percentage of impurities is 5%, with an atomic ratio between Na_2O_2, Na_2O, and NaOH of 40:3:57. This amount is substantial and yet no additional Bragg peaks were detected in the XRD patterns. Therefore, the impurities contained in the sample are likely to be poorly crystalline, which could be a result of the 10 hours of ball milling at 350 rpm carried out during the synthesis [26, 6].

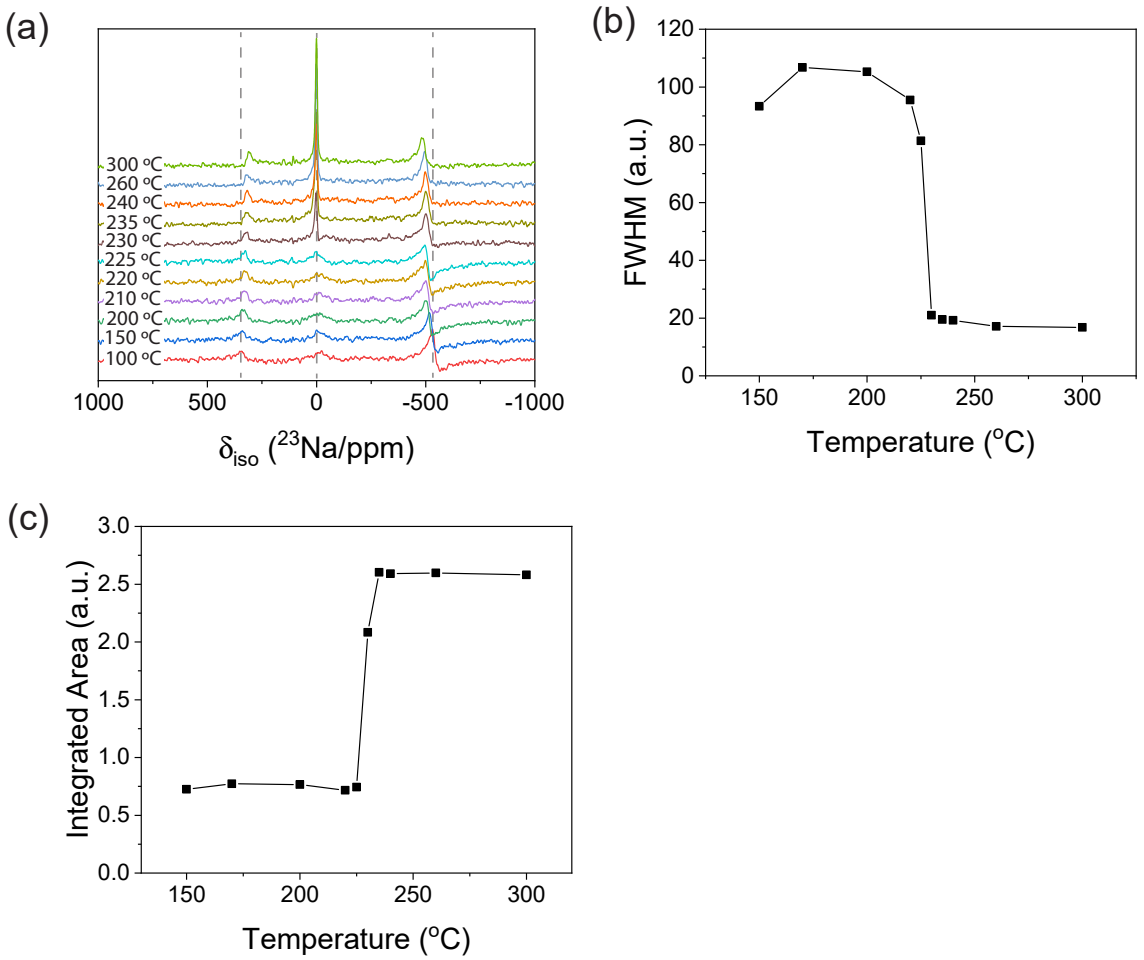

Figure 4.6: (a) The variable temperature ^{23}Na static NMR spectra of Na_3OBr (ν_0 = 132.32 MHz). (b) Full-width half maximum and (c) integrated area under the peak around 0 ppm as a function of temperature. Variable temperature NMR experiments were performed in collaboration with Dr. Kenjiro Hashi (National Institute for Materials Science).

To understand how the Na environment changes with temperature, we performed temperature-controlled static ^{23}Na NMR. As shown in Figure 4.6a, the intensity of the Na_3OBr peak remains constant over the sampled temperature range, although there is a reduction in the quadrupole coupling constant at elevated temperatures. This shows that the antiperovskite structure is maintained even after the transition, but the mobility of the sodium ions inside the structure increases slightly at these elevated temperatures. The variable temperature NMR also shows a significant intensity increase and peak width decrease in the narrower

component on heating above 230 °C [12]. These changes are typically observed for melting. Therefore, our temperature-dependent NMR results indicate that the step increase in ionic conductivity around 250 °C is likely not an intrinsic property of Na_3OBr.

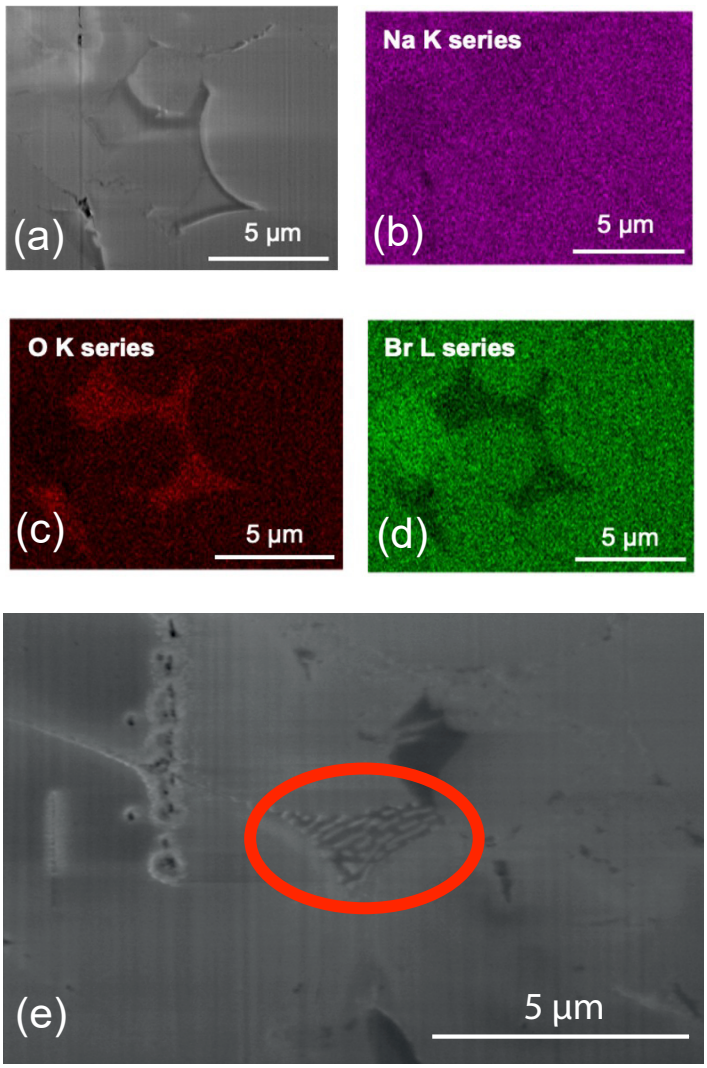

Figure 4.7: (a) Cross-sectional secondary election image of the Na_3OBr pellet taken after variable temperature EIS measurements. This image was taken with an accelerating voltage of 5 kV. Corresponding EDX analysis of the different elements: (b) Na (purple), (c) O (red), and (d) Br (green). Na is homogeneously distributed throughout the pellet but there are areas around the grain and particle boundaries which are rich in O and deficient in Br. The oxygen-rich areas are not equally distributed throughout the pellet; such a region was specifically taken on the area with this feature. (e) Cross-sectional secondary electron image of the same pellet showing eutectic-like lamellae between Na_3OBr particles. PFIB-SEM experiments were performed in collaboration with Yvonne Chart (University of Oxford).

Na_2O_2 is an impurity contained in our Na_2O precursor. It is very hygroscopic, so it could readily react with water molecules inside the glovebox to form NaOH. Each of the impurities detected by the MAS NMR is proposed to be thermodynamically stable to above $300\,^{\circ}\mathrm{C}$ [31]. However, a eutectic between Na_2O_2, Na_2O, and NaOH has been observed at $\approx 270\,^{\circ}\mathrm{C}$ [28]. Therefore, the endothermic peak seen in our DSC could correspond to the eutectic melting of a solid phase consisting of Na_2O_2, Na_2O, and NaOH. Cross-sectional EDX maps of our pellet after the variable temperature EIS (Figure 4.7) show small areas at the grain and particle boundaries that are rich in oxygen and deficient in bromine. Further, in some areas (Figure 4.7e), eutectic-like lamellae are visible, which is a strong indication that an Na_2O_2-Na_2O-NaOH eutectic mixture formed on cooling. Based on these findings, we propose that the melting of a eutectic mixture of Na_2O_2, Na_2O, and NaOH is the main factor responsible for enhanced Na^+ ionic mobility above $250\,^{\circ}\mathrm{C}$.

The importance of non-bulk factors in determining the overall ionic conductivity of solid electrolytes has been previously investigated, with the majority of work focusing on the effect of grain boundaries [23, 3, 19, 20, 35, 27]. However, the influence of impurities and their associated interphase boundaries is rarely considered. This work demonstrates how small volume fractions of impurities can have a significant impact on the macroscopic properties of a solid electrolyte. While it has been established that the presence of grain boundaries is detrimental to ionic conduction in many antiperovskite electrolytes [23, 3, 27], in this study the liquid phase that forms at the particle boundaries on heating above $250\,^{\circ}\mathrm{C}$ has been found to improve the high-temperature ionic conduction. This is supported by the Arrhenius plot of bulk and boundary ionic conductivities shown in Figure S1c and Figure S1d. The change in bulk ionic conductivity is linear with temperature,

with a constant activation energy of 0.43 eV. On the contrary, there is a step change in the boundary ionic conductivity at $250\,^{\circ}\mathrm{C}$, the temperature at which an endothermic peak was observed in the DSC. This corresponds to a reduction in activation energy from 0.51 eV to 0.31 eV. Despite improving the high-temperature ionic conduction, other properties of the liquid boundary phase such as an increased electronic conductivity may ultimately render this secondary phase undesirable [9].

4.4 Conclusion

The non-Arrhenius ionic conductivity behaviour of Na_3OBr synthesised with commercially available Na_2O does not originate from a melting or order-disorder transition. The bulk characterisation of this material did not show a detectable change in its crystal structure. Further local characterisation using variable temperature in-situ NMR revealed that the sample contained a minor fraction of poorly crystalline impurities consisting of Na_2O, Na_2O_2, and NaOH. These impurities form a eutectic mixture which melts at around $250\,^{\circ}\mathrm{C}$, promoting Na^+ mobility. While the use of the same precursors and similar synthesis methods is common in prior literature, the likelihood that these lead to the formation of poorly crystalline impurity phases which affect the electrochemical performance of the material has not been understood until now. It is therefore advisable not to use commercial Na_2O, which contains $\approx 20\%$ Na_2O_2, as a solid-state synthesis precursor. Ball-milling may reduce the crystallinity of impurity phases, which could explain why they are often overlooked in solid-state electrolyte characterisation studies. Therefore, if a mechanochemical synthesis method is employed, it is important also to check for poorly crystalline impurities. In light of these findings, the non-Arrhenius ionic con-

ductivity behaviour seen in a range of other solid electrolyte materials - particularly the Li-and K-rich antiperovskites - should be re-investigated. These findings improve understanding of the processing-structure-properties relationships pertaining to NaRAPs and highlight the need to determine these relationships in other materials systems.

4.5 Bibliography

[1] Ernest Ahiavi, James A. Dawson, Ulas Kudu, Matthieu Courty, M. Saiful Islam, Oliver Clemens, Christian Masquelier, and Theodosios Famprikis. Mechanochemical synthesis and ion transport properties of Na3OX (X = Cl, Br, I and BH4) antiperovskite solid electrolytes. *J. Power Sources*, 471:228489, 2020. ISSN 03787753. doi: 10.1016/j.jpowsour.2020.228489. URL `https://doi.org/10.1016/j.jpowsour.2020.228489`.

[2] A. A. Coelho. Topas Academic V6, 2016.

[3] James A. Dawson, Pieremanuele Canepa, Theodosios Famprikis, Christian Masquelier, and M. Saiful Islam. Atomic-Scale Influence of Grain Boundaries on Li-Ion Conduction in Solid Electrolytes for All-Solid-State Batteries. *J. Am. Chem. Soc.*, 140(1):362–368, 1 2018. ISSN 15205126. doi: 10.1021/jacs.7b10593.

[4] James A. Dawson, Hungru Chen, and M. Saiful Islam. Composition Screening of Lithium- and Sodium-Rich Anti-Perovskites for Fast-Conducting Solid Electrolytes. *J. Phys. Chem. C*, 122(42):23978–23984, 2018. ISSN 19327455. doi: 10.1021/acs.jpcc.8b08208.

[5] Christopher Doerrer, Isaac Capone, Sudarshan Narayanan, Junliang Liu, Chris R.M.

Grovenor, Mauro Pasta, and Patrick S. Grant. High Energy Density Single-Crystal NMC/Li6PS5Cl Cathodes for All-Solid-State Lithium-Metal Batteries. *ACS Appl. Mater. Interfaces*, 13(31):37809–37815, 2021. ISSN 19448252. doi: 10.1021/acsami.1c07952.

[6] Marina Enterría, Marine Reynaud, Juan Ignacio Paredes, Lidia Medinilla, Reza Younesi, and Nagore Ortiz-Vitoriano. Driving the sodium-oxygen battery chemistry towards the efficient formation of discharge products: The importance of sodium superoxide quantification. *J. Energy Chem.*, 68:709–720, 5 2022. ISSN 20954956. doi: 10.1016/j.jechem.2021.12.014.

[7] Wuliang Feng, Lei Zhu, Xiaoli Dong, Yonggang Wang, Yongyao Xia, and Fei Wang. Enhanced Moisture Stability of Lithium-Rich Antiperovskites for Sustainable All-Solid-State Lithium Batteries. *Adv. Mater.*, 35(12):2210365, 3 2023. ISSN 15214095. doi: 10.1002/adma.202210365.

[8] Lei Gao, Hao Zhang, Yuechao Wang, Shuai Li, Ruo Zhao, Yonggang Wang, Song Gao, Lunhua He, Hai Feng Song, Ruqiang Zou, and Yusheng Zhao. Mechanism of enhanced ionic conductivity by rotational nitrite group in antiperovskite Na3ONO2. *J. Mater. Chem. A*, 8(40):21265–21272, 10 2020. ISSN 20507496. doi: 10.1039/d0ta07110b.

[9] Oliver Gerbig. *Defect Chemistry in Alkali Peroxides and Superoxides*. PhD thesis, University of Stuttgart, 2014.

[10] Kenjiro Hashi, Shinobu Ohki, Yuuki Mogami, Atsushi Goto, and Tadashi Shimizu. High-Temperature Pulsed-Field-Gradient (7)Li-NMR Measurements of Li(2)CO(3)

over 700 K. *Anal Sci.*, 37(10):1477–1479, 10 2021. ISSN 1348-2246 (Electronic). doi: 10.2116/analsci.21A001.

[11] M. Jansen, C. Feldmann, and W. Müller. Über die quasi-binären Systeme NaNO2/Na2O und NaCN/Na2O. Phasendiagramme und Natrium-Ionenleitung in Na3O(NO2) und Na3O(CN). *Z. Anorg. Allg. Chem.*, 611(5):7–10, 1992. ISSN 15213749. doi: 10.1002/zaac.19926110502.

[12] Aled R Jones, Rudolf Winter, Pierre Florian, and Dominique Massiot. Tracing the Reactive Melting of Glass-Forming Silicate Batches by In Situ 23Na NMR. *J. Phys. Chem. B*, 109(10):4324–4332, 3 2005. ISSN 1520-6106. doi: 10.1021/jp045705s. URL `https://doi.org/10.1021/jp045705s`.

[13] G Klösters and M Jansen. Determination of the (Na+) Sternheimer antishielding factor by 23Na NMR spectroscopy on sodium oxide chloride, Na3OCl. *Solid State Nucl. Magn. Reson.*, 16(4):279–283, 7 2000. ISSN 0926-2040 (Print). doi: 10.1016/s0926-2040(00)00079-5.

[14] Jan Krogh-Moe. A Method for Converting Experimental X-ray Intensities to an Absolute Scale. *Acta Cryst.*, 9(11):951–953, 1956.

[15] Eriks Kupce and Ray Freeman. Adiabatic Pulses for Wideband Inversion and Broadband Decoupling. *J. Magn. Reson., Ser. A*, 115(2):273–276, 1995. ISSN 10641858. doi: 10.1006/jmra.1995.1179.

[16] Eriks Kupce and Ray Freeman. Stretched Adiabatic Pulses for Broadband Spin Inversion. *J. Magn. Reson., Ser. A*, 117(2):246–256, 1995. ISSN 10641858. doi: 10.1006/jmra.1995.0750.

[17] Yiliang Li, Ping-Chun Tsai, Fei Wang, Sunil Mair, Duhan Zhang, Liang Yin, Saul Lapidus, and Yet-Ming Chiang. Non-Arrhenius Ionic Conductivity Transitions in Sodium Antiperovskite Ionic Conductors. *ECS Meeting Abstracts*, MA2021-02(1): 43, 10 2021. doi: 10.1149/MA2021-02143mtgabs. URL `https://dx.doi.org/10.1149/MA2021-02143mtgabs`.

[18] Chengdu Liang, Wenge Yang, Ruqiang Zou, Changqing Jin, and Yusheng Zhao. Sodium Ion Transport Mechanisms in Antiperovskite Electrolytes Na3OBr and Na4OI2 : An in Situ Neutron Diffraction Study. *Inorg. Chem.*, 55(12):5993–5998, 2016. doi: 10.1021/acs.inorgchem.6b00444.

[19] Xujie Lü, Gang Wu, John W. Howard, Aiping Chen, Yusheng Zhao, Luke L. Daemen, and Quanxi Jia. Li-rich anti-perovskite Li3OCl films with enhanced ionic conductivity. *Chem. Commun.*, 50(78):11520–11522, 9 2014. ISSN 1364548X. doi: 10.1039/c4cc05372a.

[20] Xujie Lü, John W. Howard, Aiping Chen, Jinlong Zhu, Shuai Li, Gang Wu, Paul Dowden, Hongwu Xu, Yusheng Zhao, and Quanxi Jia. Antiperovskite Li3 OCl superionic conductor films for solid-state li-ion batteries. *Adv. Sci.*, 3(3):1500359, 3 2016. ISSN 21983844. doi: 10.1002/advs.201500359.

[21] Kenneth J.D. MacKenzie and Mark E. Smith. Multinuclear Solid-State NMR of Inorganic Materials. In *Pergamon Materials Series*, volume 6. Pergamon, 2002. ISBN 9780080537108.

[22] Zerina Mehmedović, Vanessa Wei, Andrew Grieder, Patrick Shea, Brandon C. Wood, and Nicole Adelstein. Impacts of vacancy-induced polarization and distor-

tion on diffusion in solid electrolyte Li3OCl. *Philos. Trans. R. Soc. A*, 379(2211): 20190459, 11 2021. ISSN 1364503X. doi: 10.1098/rsta.2019.0459.

[23] Emily Milan and Mauro Pasta. The role of grain boundaries in solid-state Li-metal batteries. *Mater. Futures*, 2(1):013501, 3 2023. doi: 10.1088/2752-5724/aca703.

[24] Han Nguyen, Sunny Hy, Erik Wu, Zhi Deng, Mojtaba Samiee, Thomas Yersak, Jian Luo, Shyue Ping Ong, and Ying Shirley Meng. Experimental and Computational Evaluation of a Sodium-Rich Anti-Perovskite for Solid State Electrolytes. *J. Electrochem. Soc.*, 163(10):A2165–A2171, 2016. ISSN 0013-4651. doi: 10.1149/2.0091610jes.

[25] N Norman. The Fourier Transform method for Normalizing Intensities. *Acta Cryst.*, 10(5):370–373, 1957.

[26] Brenden R. Ortiz, Paul M. Sarte, Alon H. Avidor, and Stephen D. Wilson. Defect control in the Heisenberg-Kitaev candidate material NaRuO2. *Phys. Rev. Materials*, 6(10):104413, 10 2022. ISSN 24759953. doi: 10.1103/PhysRevMaterials.6.104413.

[27] James A. Quirk and James A. Dawson. Design Principles for Grain Boundaries in Solid-State Lithium-Ion Conductors. *Adv. Energy Mater.*, 13(32):2301114, 8 2023. ISSN 1614-6832. doi: 10.1002/aenm.202301114. URL `https://onlinelibrary.wiley.com/doi/10.1002/aenm.202301114`.

[28] Jun-ichi Saito, Masayuki Tendo, and Kazumi Aoto. Pseudo-ternary Phase Diagram in the Na2O-Na2O2-NaOH System. Technical report, 10 1997.

[29] A K Soper. GudrunN and GudrunX: programs for correcting raw neutron and X-ray

diffraction data to differential scattering cross section. Technical report, 2011. URL http://epubs.stfc.ac.uk.

[30] Ping Chun Tsai, Sunil Mair, Jeffrey Smith, David M. Halat, Po Hsiu Chien, Kwangnam Kim, Duhan Zhang, Yiliang Li, Liang Yin, Jue Liu, Saul H. Lapidus, Jeffrey A. Reimer, Nitash P. Balsara, Donald J. Siegel, and Yet Ming Chiang. Double Paddle-Wheel Enhanced Sodium Ion Conduction in an Antiperovskite Solid Electrolyte. *Adv. Energy Mater.*, 13(7):2203284, 2 2023. ISSN 16146840. doi: 10.1002/aenm.202203284.

[31] Chun Hai Wang, Dong Yun Gui, Qingbo Xia, Maxim Avdeev, Chris D. Ling, and Brendan J. Kennedy. Structure Evolution of Na2O2from Room Temperature to 500 °C. *Inorg. Chem.*, 59(19):14439–14446, 10 2020. ISSN 1520510X. doi: 10.1021/acs.inorgchem.0c02234.

[32] Fei Wang, Ping-chun Tsai, Yiliang Li, Stephanie L Eiler, Seoung-Bum Son, and Yet-Ming Chiang. (Invited) Synthesis, Characterization, and Investigation of Non-Arrhenius Behavior in Anti-Perovskite Ion Conductors. *ECS Meeting Abstracts*, MA2019-02(2):70, 9 2019. doi: 10.1149/MA2019-02/2/70. URL https://dx.doi.org/10.1149/MA2019-02/2/70.

[33] Yonggang Wang, Qingfei Wang, Zhenpu Liu, Zhengyang Zhou, Shuai Li, Jinlong Zhu, Ruqiang Zou, Yingxia Wang, Jianhua Lin, and Yusheng Zhao. Structural manipulation approaches towards enhanced sodium ionic conductivity in Na-rich antiperovskites. *J. Power Sources*, 293:735–740, 2015. ISSN 03787753. doi:

10.1016/j.jpowsour.2015.06.002. URL http://dx.doi.org/10.1016/j.jpowsour.2015.06.002.

[34] Jingfeng Zheng, Hong Fang, Longlong Fan, Yang Ren, Puru Jena, and Yiying Wu. Antiperovskite K3OI for K-Ion Solid State Electrolyte. *J. Phys. Chem. Lett.*, 12(30): 7120–7126, 2021. ISSN 19487185. doi: 10.1021/acs.jpclett.1c01807.

[35] Jinlong Zhu, Shuai Li, Yi Zhang, John W Howard, Xujie Lü, Yutao Li, Yonggang Wang, Ravhi S Kumar, Liping Wang, and Yusheng Zhao. Enhanced ionic conductivity with Li7O2Br3 phase in Li3OBr anti-perovskite solid electrolyte. *Appl. Phys. Lett.*, 109(10):101904, 9 2016. ISSN 0003-6951. doi: 10.1063/1.4962437. URL https://doi.org/10.1063/1.4962437.

5 | On the Origin of Non-Arrhenius Ionic Conductivity in $Li_2OHCl_{0.9}Br_{0.1}$

5.1 Introduction

In Chapter 4, it was established that the origin of the non-Arrhenius ionic conductivity in Na_3OBr is not due to Na_3OBr itself. Instead, it is due to the poorly crystalline Na_2O_2 impurity from the Na_2O precursor. The non-Arrhenius ionic conductivity behaviour is also observed in the Li_2OHX (X = Cl, Br, or mix) series, but it occurs close to their melting points [13, 7, 16]. The melting points of Li_2OHX compositions are less than $300\,^{\circ}\mathrm{C}$, which is relatively low for a solid-electrolyte [13, 7, 16, 11]. $Li_2OHCl_{0.9}Br_{0.1}$ was chosen for this non-Arrhenius study for two reasons. Firstly, it is stable as cubic from RT up to its transition temperature and so it is not expected to undergo any other phase transition in the temperature range of interest. Secondly, it has the widest gap between the suspected transition temperature and the melting point ($\approx 7\,^{\circ}\mathrm{C}$) [7]. This gap allowed us to gather more data points after the transition and before it melted, to probe into the origin of non-Arrhenius behaviour in the Li_2OHX system. Investigation of two different compositions (Na_3OBr and $Li_2OHCl_{0.9}Br_{0.1}$) using similar characterisation techniques reveals that despite the initial similarities in behaviour, their origins are different.

5.2 Experimental Methods

5.2.1 Synthesis of $Li_2OHCl_{0.9}Br_{0.1}$

$Li_2OHCl_{0.9}Br_{0.1}$ was synthesised from a simple mixing and melting synthesis procedure. LiOH (98%, Sigma Aldrich) was mixed with LiCl ($\geqslant$ 99%, Sigma Aldrich) in a 1:1 ratio, and ground with a mortar and pestle for 10 min. The well-mixed powder was then placed on an alumina crucible and heated to $350\,^{\circ}\mathrm{C}$ in a muffle furnace with a ramping rate of $5\,^{\circ}\mathrm{C\,min^{-1}}$ and kept at this temperature for 30 min. The liquid $Li_2OHCl_{0.9}Br_{0.1}$ was immediately taken out of the furnace and left to cool down under the inert gas atmosphere. To produce the final $Li_2OHCl_{0.9}Br_{0.1}$ powder, the solid chunk was ground with a mortar and pestle for 10 minutes.

5.2.2 Differential Scanning Calorimetry (DSC)

In the literature, it has been argued that highly corrosive antiperovskite melt may react with aluminium and accidentally dope the antiperovskites with Al^{3+} cations, generating a high concentration of vacancies at the octahedral vertices due to the charge-balance rule [16]. To prevent this unwanted reaction, $Li_2OHCl_{0.9}Br_{0.1}$ was measured in an alumina crucible. The instrument compatible with this pan was not located inside a glovebox. Hence, the argon shower was activated during the sample transfer process into the instrument. The argon flow was kept on during the measurement to minimise the contact that the sample had with air molecules. The DSC was measured with a rate of $5\,^{\circ}\mathrm{C/min}$ between room temperature and $300\,^{\circ}\mathrm{C}$.

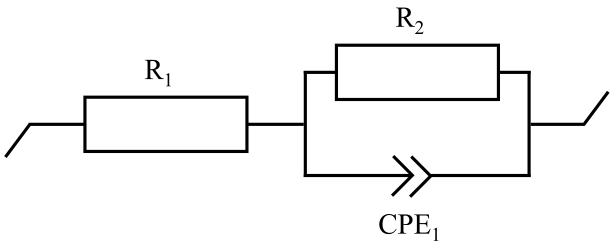

Figure 5.1: Equivalent circuit used to simulate our experimental set-up. R_1 is the bulk resistance, R_2 is the total resistance (bulk + boundaries), and CPE_1 is the total capacitance.

5.2.3 Electrochemical Impedance Spectroscopy (EIS)

The EIS characterisation was carried out in a custom-built PEEK solid-state cell using gold powder (Alfa Aesar, gold powder, spherical, APS 0.5 – $0.8\,\mu\mathrm{m}$) as the blocking electrodes.[4] Gold powder was added to one side of the cold pressed pellet and then pressed at 370 MPa for 3 minutes before turning the pellet over to perform the same procedure on the opposite side. Using a screw on top of the cell, a uniaxial pressure of $\approx$ 70 MPa was applied during the measurements. The cell was then heated inside a muffle furnace in a glovebox for an hour at each data point before a measurement was performed using a two-probe configuration to a BioLogic MTZ35 frequency response analyser. Potentiostatic EIS (PEIS) measurements were conducted in the frequency range of 35 MHz to 0.1 Hz with a voltage amplitude of 10 mV. ZView software was used to simulate Nyquist plots based on the equivalent circuit depicted in Fig Figure 5.1.

5.2.4 X-ray Diffraction (XRD)

Ex-situ X-ray powder diffraction measurements were performed using Rigaku Smartlab SE - 3kW diffractometers (Cu Kα) to preliminary check the purity of the sample. Total scattering data were collected at the I15-1 beamline at Diamond Light Source operating

with an X-ray wavelength of $0.161\,669\,\text{Å}$. Samples were put in $1\,\text{mm}$ borosilicate glass capillaries. Data for both background containers and samples were collected in a *Q* range 0.3 - 25 A^{-1} in a temperature range from 150 to $300\,^{\circ}\text{C}$ in $5\,^{\circ}\text{C}$ intervals. GudrunX routines were employed to process the PDF data. All Pawley and Rietveld refinements of the Bragg data were carried out using the TOPAS-Academic software [2]. In total, 25 parameters were refined during the Rietveld refinements: 18 polynomial function parameters to fit the background, the lattice parameter, b_{eq} halide, the scale parameter, and the 4 peak shape function parameters (pku, pkv, pkw, and pky).

5.2.5 Nuclear Magnetic Resonance (NMR) Spectroscopy

Variable temperature NMR measurements (25 - $300\,^{\circ}\text{C}$) were done at the National Institute for Materials Science (NIMS) using an ECA-500 (JEOL, Japan) spectrometer and a homemade probe [5]. The sample was packed into a quartz NMR tube SP-405 (SHIGEMI, Japan) and sealed in an Ar-filled globe box. The resonance frequency of ^{23}Na was 132.32 MHz. The chemical shift was referenced to the 1.0 M NaCl solution at 0 ppm. The temperature was controlled by a nitrogen gas flow.

5.3 Results and Discussion

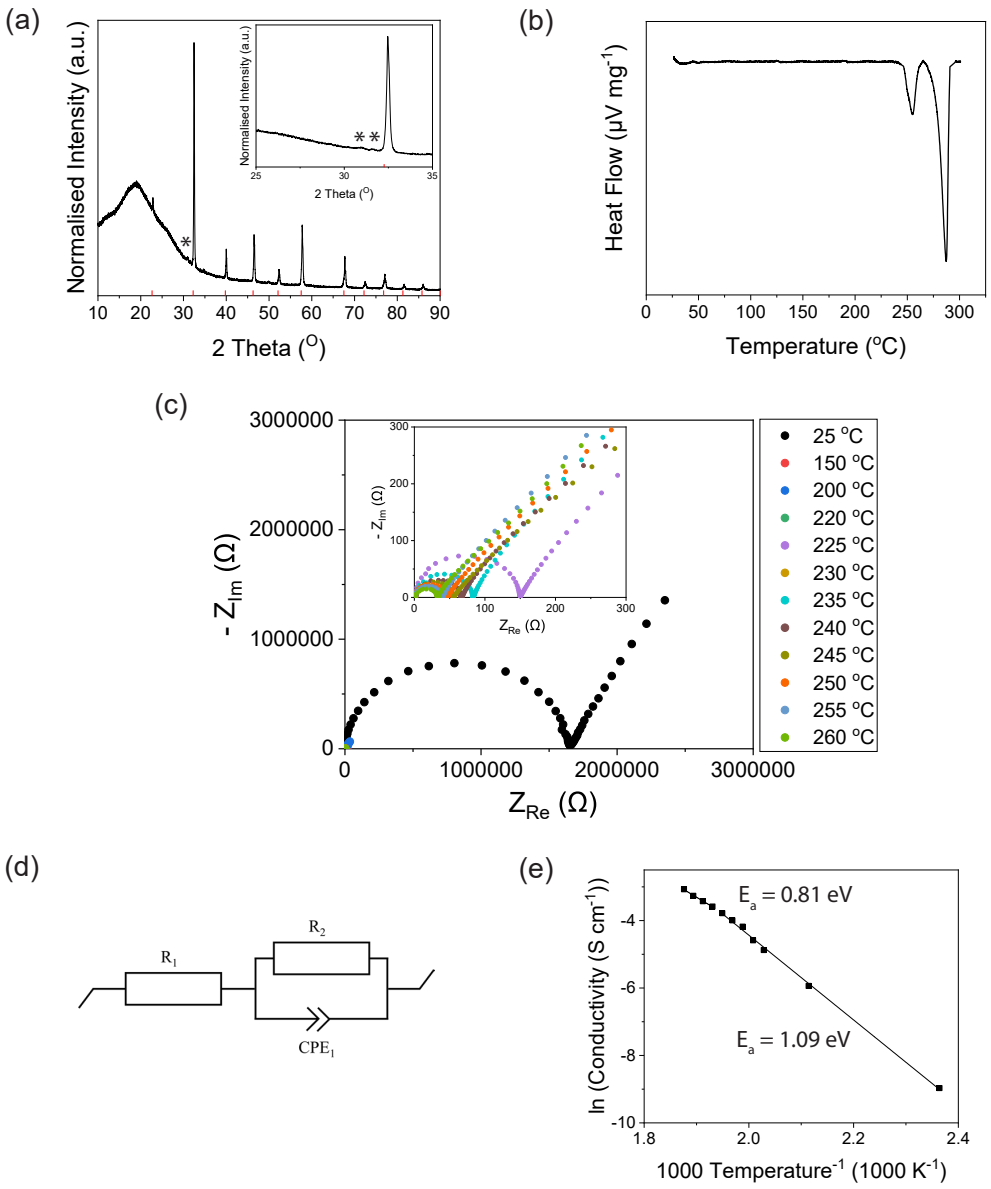

Figure 5.2: In-house characterisations of as-synthesised $Li_2OHCl_{0.9}Br_{0.1}$. (a) Ex-situ X-ray diffractogram taken with Rigaku Smartlab SE - 3kW diffractometer (Cu Kα). (b) DSC of $Li_2OHCl_{0.9}Br_{0.1}$ showing two endothermic peaks at $240\,^{\circ}C$ and $270\,^{\circ}C$. (c) Nyquist plots of $Li_2OHCl_{0.9}Br_{0.1}$ at multiple temperatures between $25\,^{\circ}C$ and $260\,^{\circ}C$. (d) An equivalent circuit was used to simulate our experimental setup. R_1 is instrument cabling or electric contact resistance, R_2 is the total resistance of the cell, and CPE_1 is the total capacitance of the cell. (e) Arrhenius plot of total ionic conductivity of $Li_2OHCl_{0.9}Br_{0.1}$ with a change in activation energy for Li^+ migration at $235\,^{\circ}C$.

Like Na_3OB, $Li_2OHCl_{0.9}Br_{0.1}$ possess the same structure as perovskites, but with inverted anion/cation. The main difference between the two is that 1/3 of the Li-ions in this structure are substituted by protons, thus forming Li vacancy sites. An in-house ex-situ XRD measurement of the sample in Figure 5.2a showed minor LiCl impurity. A Rietveld refinement (Figure 5.3b) of the synchrotron XRD pattern of $Li_2OHCl_{0.9}Br_{0.1}$ at RT reveals that it has a cubic structure with a space group of $Pm\bar{3}m$ with a unit cell of a = 3.9210(4) Å. The refinement parameters can be found in Table 5.1. The weighted profile factor, R_{wp}, of this refinement is 3.2%, indicating a good fit. In addition to the antiperovskite phase, the XRD pattern reveals peaks that belong to 2 wt% LiCl, confirming an earlier finding from in-house ex-situ measurement, while other impurities (like Li_2O or LiOH) were barely noticeable. This suggests that Li and Cl vacancies are present in the structure to satisfy charge neutrality. $Li_2OHCl_{0.9}Br_{0.1}$'s stability as cubic even at RT is similar to that of Li_2OHBr but very different from that of Li_2OHCl, which possesses orthorhombic structure with a space group of $Pmc2_1$ at RT and transitions to cubic structure at a temperature around $40\,^{\circ}\mathrm{C}$. Partial substitution of Cl^- with Br^- stabilises the $Li_2OHCl_{0.9}Br_{0.1}$ because the large Br^- ion in the lattice leads to higher symmetry. The small amount of impurities in the XRD pattern could have been eliminated by adjusting the stoichiometric ratio of the precursors [7]. However, in this experiment, stoichiometry was prioritised over purity as adjusting it will influence the vacancy concentration.

Table 5.1: Sequential Rietveld refinement results for $Li_2OHCl_{0.9}Br_{0.1}$.

Temperature [°C]	R_{wp} [%]	Lattice Parameter [Å]	Lattice Parameter Error [Å]	$b_{eq\mathrm{Hal}}$ [a.u.]	$b_{eq\mathrm{Hal}}$ Error [a.u.]
25	3.16761	3.922905	0.00003918	1.76519	0.02398253
40	3.10535	3.92608841	0.00003925	1.88290097	0.02471321
100	3.0075	3.93683361	0.00004009	2.26090551	0.02745943
150	2.95969	3.94601249	0.0000407	2.57899991	0.02989319
170	2.80754	3.95667124	0.00003953	2.95513108	0.03128937
220	2.35802	3.96556068	0.00003489	3.36528445	0.03148089

240	2.1912	3.96855797	0.00003485	3.66156374	0.03417319
250	2.10237	3.9674146	0.0000433	3.93181689	0.04732065
260	2.24165	3.96504435	0.00006718	4.37373449	0.09062249

Thermal properties of materials can serve as useful indicators of structural changes. Differential scanning calorimetry (DSC) was performed to investigate the thermal stability of $Li_2OHCl_{0.9}Br_{0.1}$. Supporting our earlier finding from RT synchrotron XRD, $Li_2OHCl_{0.9}Br_{0.1}$ did not exhibit an endothermic peak originating from the orthorhombic to cubic phase transition at around $40\,^{\circ}\mathrm{C}$, indicating that Br is an effective phase stabiliser. Upon heating, two endothermic peaks were observed: at $240\,^{\circ}\mathrm{C}$ and at $270\,^{\circ}\mathrm{C}$ (Figure 5.2b). From our physical observation, when the sample was heated in a muffle furnace, it became liquid above $270\,^{\circ}\mathrm{C}$. Therefore, the peak at the higher temperature originates from crystal melting. The ratio of the area under the peak between the one at $240\,^{\circ}\mathrm{C}$ and that at $270\,^{\circ}\mathrm{C}$ is 3:4. This suggests that the phenomenon which occurs at $240\,^{\circ}\mathrm{C}$ consumes much less energy. From physical observation, $Li_2OHCl_{0.9}Br_{0.1}$ appears to remain in the solid phase until around $270\,^{\circ}\mathrm{C}$. To our knowledge, there are reports on similar DSC results but the origin of of the DSC peak at $240\,^{\circ}\mathrm{C}$ is not yet well understood [13, 7, 16].

Temperature-dependent potentiostatic electrochemical impedance (PEIS) was used to investigate whether the endothermic peak at $240\,^{\circ}\mathrm{C}$ has any effect on the ionic conductivity of the sample. A pressure of $\approx 70\,\mathrm{MPa}$ was applied to the cell during the measurements to maintain good contact between gold-blocking electrodes and the $Li_2OHCl_{0.9}Br_{0.1}$. The Nyquist plots from the measurements between $25\,^{\circ}\mathrm{C}$ and $300\,^{\circ}\mathrm{C}$ are shown in Figure 5.2d. Each of them shows one nearly perfect semi-circle, thus the setup was modelled as an equivalent circuit shown in Figure 5.2c. R_2 and PE_1 correspond to the total ionic conduction (bulk and boundaries) of $Li_2OHCl_{0.9}Br_{0.1}$. It was not possible to deconvolute the bulk

and boundaries contribution reliably because there is no clear dip that could separate the two contributions in the Nyquist plots. However, it is expected that the boundary contributions are the bottleneck of the total transport, as it is well-known in the SE community that cation conduction through boundaries requires higher activation energies than that through bulk. Schwering et al. attempted to do the convolution for mixed halide Li_2OHB where B is Cl and/or Br. The activation energies they obtained were 0.62 – 0.73 and 0.31 – 0.38 eV for grain boundary and bulk, respectively [11]. As the temperature increases, the diameter of the semi-circle decreases due to an increase in ionic conductivity of Li-ion inside the $Li_2OHCl_{0.9}Br_{0.1}$. The values of ionic conductivities measured between $25\,^{\circ}\mathrm{C}$ and $300\,^{\circ}\mathrm{C}$ are shown in Figure 5.2e. There is a step change in the total ionic conductivity at $235\,^{\circ}\mathrm{C}$, which corresponds to a reduction of activation energy from 1.09 eV to 0.81 eV. These values are higher than the reported experimental and simulation values (0.24 - 0.42), possibly due to the differences in cooling regime [3, 12]. During the synthesis, the melted precursors were taken out of the furnace at $350\,^{\circ}\mathrm{C}$ immediately and left to cool down to room temperature under the inert glovebox atmosphere. This likely results in a high concentration of grain boundaries that severely hinders the Li^+ ionic conduction. The non-Arrhenius ionic conductivity behaviour observed in this material is similar to the one observed in Na_3OBr. Despite this initial similarity, it is not clear whether this behaviour also originates from impurities or an order-to-disorder transition in the crystal structure.

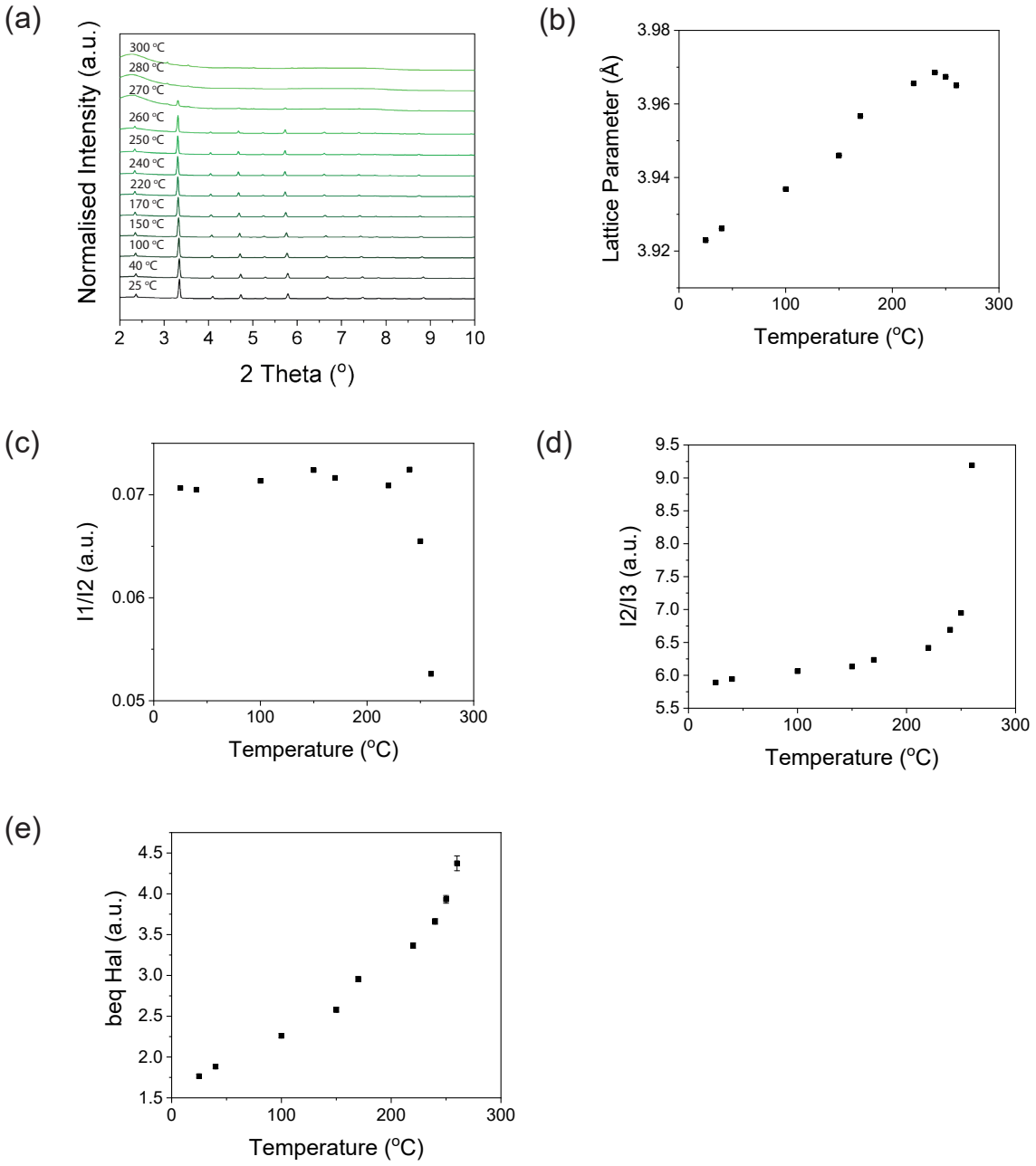

Figure 5.3: (a) In-situ variable temperature XRD patterns of $Li_2OHCl_{0.9}Br_{0.1}$ with an X-ray wavelength of $0.161\,669$ Å. Sequential Pawley and Rietveld refinements were performed on the data, and the changes in (b) lattice parameter, (c) ratio between the intensity of (100) and (110) peaks, (d) ratio between the intensity of (110) and (111) peaks, and (e) thermal parameter of halide ions (b_{eq} Hal) of $Li_2OHCl_{0.9}Br_{0.1}$ are plotted as a function of temperature. Experiments with I15-1 were performed in collaboration with Dr. Maria Diaz-Lopez (Diamond Light Source).

To understand how the $Li_2OHCl_{0.9}Br_{0.1}$ crystal structure evolves with temperature and probe into the origin of its non-Arrhenius ionic conductivity behaviour, sequential Paw-

ley and Rietveld refinements were performed on the synchrotron XRD data between $25\,^{\circ}\mathrm{C}$ and $300\,^{\circ}\mathrm{C}$. Any sign of discontinuity, like in the lattice parameter and elemental thermal parameters (b_{eq}), could give an indication of a phase transition or an order to disorder transition. Supporting our earlier DSC finding, the intensities of the $Li_2OHCl_{0.9}Br_{0.1}$ peaks do not change drastically around $40\,^{\circ}\mathrm{C}$, confirming that the structure is stable as cubic unlike that of Li_2OHCl. The Bragg peak positions shift to lower angles due to the thermal expansion of the $Li_2OHCl_{0.9}Br_{0.1}$ lattice. From the sequential Pawley refinements, we found that the change in lattice parameter is constant with temperature until around $240\,^{\circ}\mathrm{C}$ (Figure 5.3b). Above this temperature, the lattice parameter decreases until all the crystalline peaks in the XRD pattern disappear and the sample finally melts at $260\,^{\circ}\mathrm{C}$. Hence, between $240\,^{\circ}\mathrm{C}$ and $260\,^{\circ}\mathrm{C}$, the sample stays in the solid phase while the lattice volume decreases and the ions get closer to one another. In addition, we calculated the ratio between the intensity of (100) and (110) peaks and that of (110) and (111) peaks. Initially, both ratios did not change with temperature. However, at $240\,^{\circ}\mathrm{C}$ the former ratio starts decreasing while the latter one starts increasing (Figure 5.3c and d). From this, we can learn that the absolute value of (110) peak intensity decreases after $240\,^{\circ}\mathrm{C}$. Peak intensity is related to the number of atoms in the crystal that are capable of scattering X-rays. In $Li_2OHCl_{0.9}Br_{0.1}$, the oxygen, halide, and lithium ions can all be found in the (110) plane. However, it is likely that the intensity is dominated by the halide ions as they are the strongest X-ray scatterers in the structure. This means that above $240\,^{\circ}\mathrm{C}$, there are fewer halide ions in the (110) plane, which can happen if they migrate from their original positions to neighbouring vacant sites. The weighted profile factor, R_{wp}, of all Rietveld refinements were less than 3.2 %, indicating good matches between the models and the

experimental data. Most of the elements contained in our sample (Li, H, and O) are weak X-ray scatterers [14, 1], thus during the Rietveld refinements the thermal parameter analysis was only done on the halide ions (Figure 5.3e). The Cl^- and Br^- ions are treated as hybrid ions because their positions in the crystal structure are interchangeable. The thermal parameter of the halide ions initially changed linearly with temperature but above $240\,^{\circ}\mathrm{C}$ the value increases at a higher rate, indicating a step increase in the vibration of the halide ions. This finding is in line with the findings from the PDF calculation done on K_3OI by Zheng et al. [17]. At room temperature, they did not observe local disordering in the anion sub-lattice and so the K-ions migrate via the vacancy sites. At high simulation temperatures, above the non-Arrhenius transition temperature, local anion disorder is activated with the I-ion migrating to the neighbouring vacant site and the O-ion migrating toward the vacated I-site. As a result, K-ion can migrate via both the K-vacancies and the vacancies created by the O-I disordering. Experimentally, the change in the peak intensity ratios and the step increase that we observed in the thermal vibration of the halide ions at $240\,^{\circ}\mathrm{C}$ are signs of halide ion migration and subsequently the anion disordering.

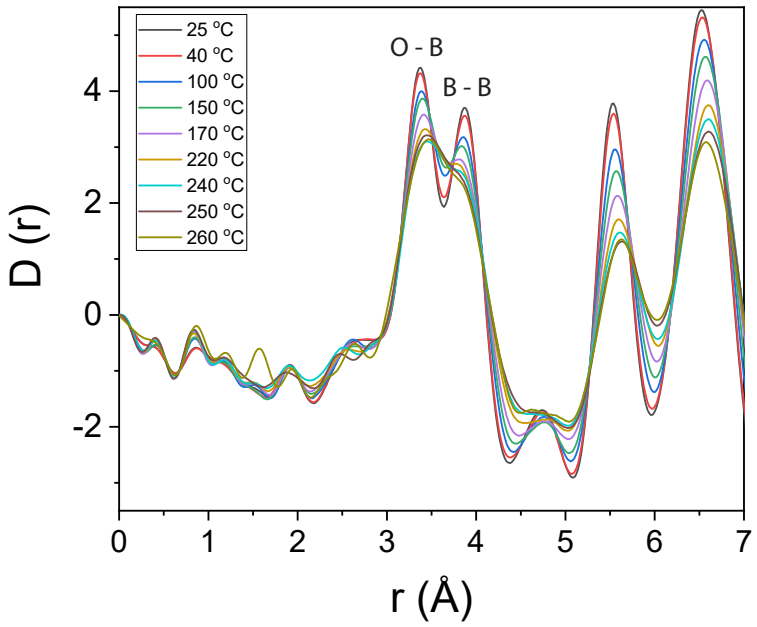

Figure 5.4: Differential correlation function *D(r)* calculated from experimental X-ray total structure factor *F(Q)*. Measurement was done with an X-ray wavelength of $0.161\,669$ Å. Experiments with the I15-1 beamline were performed in collaboration with Dr. Maria Diaz-Lopez (Diamond Light Source).

The pair distribution function (PDF) was measured at the same beamline as the Bragg measurement. In order to investigate the local structure of $Li_2OHCl_{0.9}Br_{0.1}$, we looked at the pair distribution function (PDF) in the range of 0 Å to 5 Å. The majority of the peak positions shift to higher distances while the widths broaden as the temperature increases. This behaviour can be attributed to thermal expansion and the thermal population of phonons. In addition, we observed a change in the intensity and broadness of the O-B peak (3.4 Å) and B-B peak (3.8 Å) [9, 10], where B is either Cl or Br. The change between $220\,^{\circ}$C and $240\,^{\circ}$C is more drastic than the that between $240\,^{\circ}$C and $260\,^{\circ}$C, suggesting that a transition is happening at around $240\,^{\circ}$C. The two peaks merged above $240\,^{\circ}$C, showing that the O-B and B-B distances are getting similar. This supports our earlier anion disordering findings from sequential Pawley and Rietveld refinements. Evidence of anion disordering is found at both bulk and local levels.

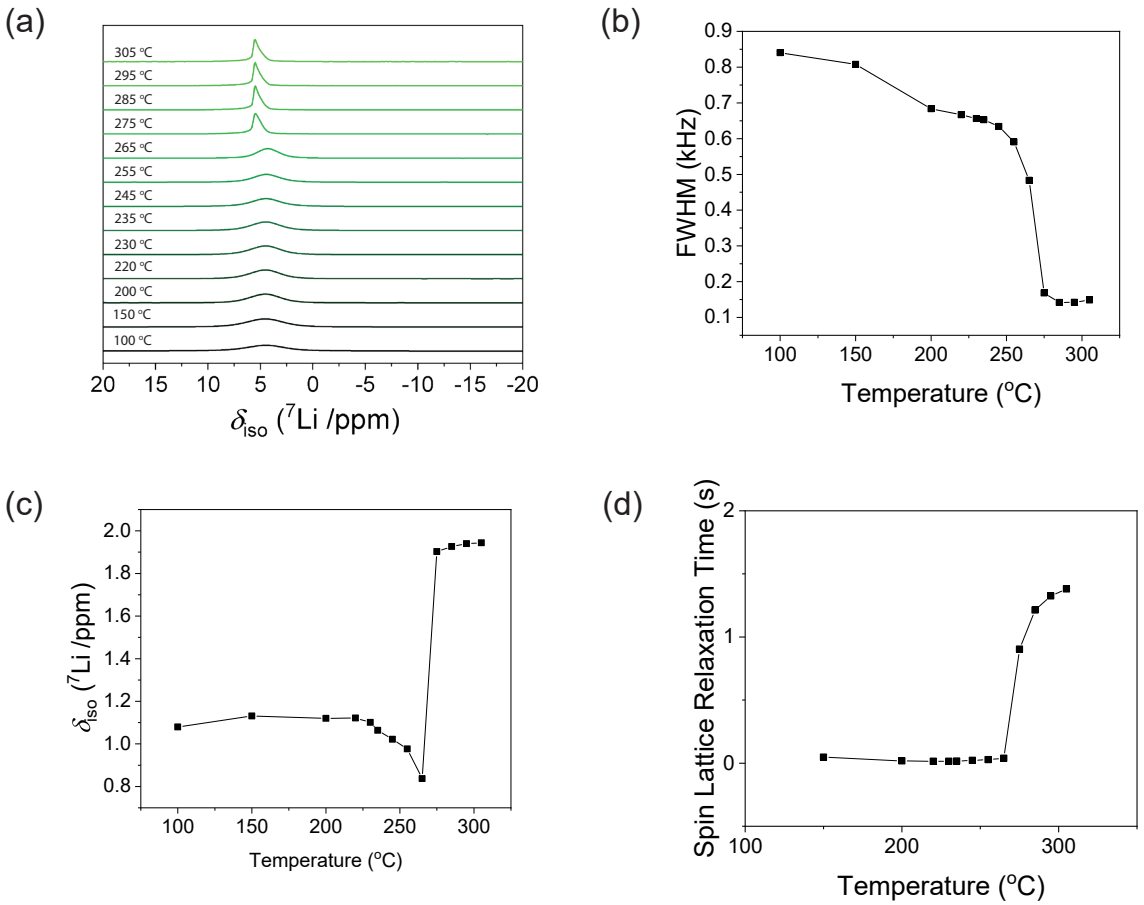

Figure 5.5: (a) The variable temperature ^{7}Li static NMR spectra of $Li_2OHCl_{0.9}Br_{0.1}$. Plots of (b) Full-width half maximum, (c) integrated area under the central peak, and (d) spin-lattice relaxation time (T_1) as a function of temperature. Variable temperature NMR experiments were performed in collaboration with Dr. Kenjiro Hashi (National Institute for Materials Science).

Another technique employed to study how the local Li environment changes with temperature was static ^{17}Li NMR spectroscopy, as shown in Figure 5.5. The spectrum consists of a central peak at $\approx$ 1 ppm, which originates from the $m = +1/2$ to $m = -1/2$ transition (central transition) of the $I = 3/2$ ^{7}Li quadrupolar nucleus. This is similar to the Li_2OHBr spectra reported by Schwering et al. [11]. Since the local symmetry at the site of the ^{7}Li is cubic, quadrupolar interaction was small and no obvious quadrupolar peak shape was observed. As the temperature increases, the peak width decreases, and this becomes more significant above $235\,^{\circ}\mathrm{C}$. The peak sharpening is due to the increase of Li^{+}

mobility. This supports our findings from EIS, where a step increase in Li^+ mobility was observed at around $235\,^{\circ}\mathrm{C}$. In the case of the ^{7}Li chemical shifts, initially, the values stay almost constant with temperature, which is a sign that there is not much change in the Li environment. However, the chemical shift value decreases between $230\,^{\circ}\mathrm{C}$ and $265\,^{\circ}\mathrm{C}$. This could have happened because the local structure surrounding the ^{7}Li changes, which is in line with our earlier findings from the sequential Pawley refinements, where the lattice parameter of the $Li_2OHCl_{0.9}Br_{0.1}$ decreases above $240\,^{\circ}\mathrm{C}$. At $260\,^{\circ}\mathrm{C}$, the ^{7}Li peak shifts to around 2 ppm, the peak width decreases significantly, and the spin-lattice relaxation time also changes significantly. All parameters stay almost constant above this temperature. These changes are typically observed for melting [6], which was also confirmed by our DSC and variable temperature XRD measurements. Looking back at all our findings, we propose that the anion disordering is the main factor responsible for the endothermic peak observed in the DSC at $240\,^{\circ}\mathrm{C}$ and subsequently the enhanced Li^+ ionic mobility in $Li_2OHCl_{0.9}Br_{0.1}$ between this temperature and the melting point. However, it is still not clear why the origins of the non-Arrhenius ionic conductivity behaviour in $Li_2OHCl_{0.9}Br_{0.1}$ and Na_3OBr are different, despite the initial similarities in behaviour and temperature at which this behaviour starts. The main differences between the two compositions lie in the vacancy contents and the fact that $Li_2OHCl_{0.9}Br_{0.1}$ has some degree of disordering to start with because of the anion mixing (Cl with Br). To elucidate the role of any of these factors in determining the origin of the non-Arrhenius behaviour in antiperovskites, comparison studies should be done on compositions with variable vacancy content and both mixed and single-halide anions. Additionally, molecular dynamics (MD) or reverse Monte Carlo (RMC) simulations are required to fit the experimental data with

an appropriate model structure to visualise and probe into the anion disordering mechanisms [17, 8, 15]. To confirm the absence of eutectic mixture of impurities, like the one observed in Chapter 4, cross-section SEM and energy dispersive X-ray spectroscopy (EDX) need to be perform on the pellet after the EIS measurements.

5.4 Conclusion

The origin of non-Arrhenius ionic conductivity behaviour in $Li_2OHCl_{0.9}Br_{0.1}$ is different from that in Na_3OBr. Both bulk and local characterisations of $Li_2OHCl_{0.9}Br_{0.1}$ showed a detectable change in its crystal structure. From Pawley and Rietveld refinements of the variable temperature Bragg data, discontinuity was observed in the lattice parameter, peak intensity ratios, and halide ions thermal parameter. The lattice parameter decreases above $240\,^{\circ}\mathrm{C}$ and the rate of increase of the halide ions thermal parameter increases above the same point. These findings show that there is a bulk change in the crystal structure where the ions are getting closer to one another. Supporting these findings, the PDF data from the same beamline (DLS I15-1) showed significant changes in the O-B and B-B, where B is a halide ion, peaks. They merge above the temperature at which the first endothermic peak was observed in the DSC of $Li_2OHCl_{0.9}Br_{0.1}$, at around $240\,^{\circ}\mathrm{C}$. This means that the O^{2-}, Cl^{-}, and Br^{-} ions migrate from their original positions in the cubic structure and maintain this new structure until the structure finally melts. Further local characterisation using variable temperature in-situ NMR revealed that both the chemical shifts and the peak width decrease significantly at around $230\,^{\circ}\mathrm{C}$. This peak width behaviour can be explained by a significant increase in Li^{+} mobility, which is in line with our finding from EIS, where we saw a step increase in ionic conductivity and a decrease in activation

energy from 1.09 eV to 0.81 eV at a similar temperature. The decrease in chemical shift value between $230\,^{\circ}\mathrm{C}$ and $265\,^{\circ}\mathrm{C}$ could have happened because the local structure surrounding the ^{7}Li changes. This supports our earlier findings from the sequential Pawley refinements, where the lattice parameter of the $Li_2OHCl_{0.9}Br_{0.1}$ decreases above $240\,^{\circ}\mathrm{C}$. In light of these findings, we propose that the anion disordering is the main factor responsible for the endothermic peak observed in the DSC at $240\,^{\circ}\mathrm{C}$ and subsequently the enhanced Li^{+} ionic mobility in $Li_2OHCl_{0.9}Br_{0.1}$ between this temperature and the melting point. These findings improve understanding of how $Li_2OHCl_{0.9}Br_{0.1}$'s structure changes with temperature and how this change affects its ionic conductivity. We hope this finding will help accelerate the development of high-performance solid electrolytes.

5.5 Bibliography

[1] Chuntian Cao, Michael F. Toney, Tsun Kong Sham, Ross Harder, Paul R. Shearing, Xianghui Xiao, and Jiajun Wang. Emerging X-ray imaging technologies for energy materials. *Materials Today*, 34:132–147, 4 2020. ISSN 18734103. doi: 10.1016/j.mattod.2019.08.011.

[2] A. A. Coelho. Topas Academic V6, 2016.

[3] James A. Dawson, Tavleen S. Attari, Hungru Chen, Steffen P. Emge, Karen E. Johnston, and M. Saiful Islam. Elucidating lithium-ion and proton dynamics in anti-perovskite solid electrolytes. *Energy and Environmental Science*, 11(10):2993–3002, 10 2018. ISSN 17545706. doi: 10.1039/c8ee00779a.

[4] Christopher Doerrer, Isaac Capone, Sudarshan Narayanan, Junliang Liu, Chris R.M.

Grovenor, Mauro Pasta, and Patrick S. Grant. High Energy Density Single-Crystal NMC/Li6PS5Cl Cathodes for All-Solid-State Lithium-Metal Batteries. *ACS Appl. Mater. Interfaces*, 13(31):37809–37815, 2021. ISSN 19448252. doi: 10.1021/acsami.1c07952.

[5] Kenjiro Hashi, Shinobu Ohki, Yuuki Mogami, Atsushi Goto, and Tadashi Shimizu. High-Temperature Pulsed-Field-Gradient (7)Li-NMR Measurements of Li(2)CO(3) over 700 K. *Anal Sci.*, 37(10):1477–1479, 10 2021. ISSN 1348-2246 (Electronic). doi: 10.2116/analsci.21A001.

[6] Koji Kanehashi and Jonathan F. Stebbins. In situ high temperature 27Al NMR study of structure and dynamics in a calcium aluminosilicate glass and melt. *Journal of Non-Crystalline Solids*, 353(44-46):4001–4010, 11 2007. ISSN 00223093. doi: 10.1016/j.jnoncrysol.2007.06.030.

[7] Hyeon Jeong Lee, Brigita Darminto, Sudarshan Narayanan, Maria Diaz-Lopez, Albert W. Xiao, Yvonne Chart, Ji Hoon Lee, James A. Dawson, and Mauro Pasta. Li-ion conductivity in Li2OHCl1-xBrx solid electrolytes: grains, grain boundaries and interfaces. *J. Mater. Chem. A*, 10(21):11574–11586, 4 2022. ISSN 20507496. doi: 10.1039/d2ta01462a.

[8] Y. Onodera, K. Mori, T. Otomo, A. C. Hannon, M. Sugiyama, and T. Fukunaga. Reverse Monte Carlo modeling of Li2S-P2S5 superionic conductors. In *Journal of Physics: Conference Series*, volume 340. Institute of Physics Publishing, 2012. doi: 10.1088/1742-6596/340/1/012058.

[9] Shuching Ou and Sandeep Patel. Temperature dependence and energetics of single

ions at the aqueous liquid-vapor interface. *Journal of Physical Chemistry B*, 117 (21):6512–6523, 5 2013. ISSN 15205207. doi: 10.1021/jp401243m.

[10] Richard C. Remsing and Michael L. Klein. Halogen Bond Structure and Dynamics from Molecular Simulations. *Journal of Physical Chemistry B*, 123(29):6266–6273, 7 2019. ISSN 15205207. doi: 10.1021/acs.jpcb.9b04820.

[11] Georg Schwering, Andreas Hönnerscheid, Leo Van Wüllen, and Martin Jansen. High lithium ionic conductivity in the lithium halide hydrates Li3-n(OHn)Cl (0.83 $\leqslant$ n $\leqslant$ 2) and Li3-n(OHn)Br (1 $\leqslant$ n $\leqslant$ 2) at ambient temperatures. *ChemPhysChem*, 4(4):343–348, 4 2003. ISSN 14394235. doi: 10.1002/cphc.200390060.

[12] Ah Young Song, Yiran Xiao, Kostiantyn Turcheniuk, Punith Upadhya, Anirudh Ramanujapuram, Jim Benson, Alexandre Magasinski, Marco Olguin, Lamartine Meda, Oleg Borodin, and Gleb Yushin. Protons Enhance Conductivities in Lithium Halide Hydroxide/Lithium Oxyhalide Solid Electrolytes by Forming Rotating Hydroxy Groups. *Advanced Energy Materials*, 8(3), 1 2018. ISSN 16146840. doi: 10.1002/aenm.201700971.

[13] Manoj Krishna Sugumar, Takayuki Yamamoto, Munekazu Motoyama, and Yasutoshi Iriyama. Room temperature synthesis of anti-perovskite structured Li 2 OHBr. *Solid State Ionics*, 349(March):115298, 2020. ISSN 0167-2738. doi: 10.1016/j.ssi.2020.115298. URL `https://doi.org/10.1016/j.ssi.2020.115298`.

[14] S. Uthayakumar, M. S. Pandiyan, D. G. Porter, M. J. Gutmann, R. Fan, and J. P. Goff. Crystal growth and neutron diffraction studies of LixCoO2bulk single crystals.

Journal of Crystal Growth, 401:169–172, 9 2014. ISSN 00220248. doi: 10.1016/j.jcrysgro.2013.11.043.

[15] X Wang, Xuelong Wang, Sha Tan, Xiao-Qing Yang, and Enyuan Hu. Pair distribution function analysis: Fundamentals and application to battery materials DISCLAIMER Pair distribution function analysis: Fundamentals and application to battery materials. Technical Report 2, 2020. URL `http://cpb.iphy.ac.cn`.

[16] Yusheng Zhao and Luke L. Daemen. Superionic conductivity in lithium-rich anti-perovskites. *Journal of the American Chemical Society*, 134(36):15042–15047, 9 2012. ISSN 00027863. doi: 10.1021/ja305709z.

[17] Jingfeng Zheng, Hong Fang, Longlong Fan, Yang Ren, Puru Jena, and Yiying Wu. Antiperovskite K3OI for K-Ion Solid State Electrolyte. *J. Phys. Chem. Lett.*, 12(30): 7120–7126, 2021. ISSN 19487185. doi: 10.1021/acs.jpclett.1c01807.

6 | Conclusion and Future Work

SSBs with metal anodes are believed to be the way forward in the development of batteries with higher energy density and improved safety. Suitable SEs would be key to realise SSBs' potentials. The interest in the antiperovskite family as SEs for battery applications arises from several factors, including:

1. A simple structure that can be iso- and aliovalently substituted to achieve the desired properties.

2. The absence of (semi)metallic elements, which reduces the stability of the SEs against metal anodes and leads to low electrochemical stability in batteries.

3. Their relatively soft mechanical properties, which are key to maximum densification and integration in SSBs.

Despite these reasons, research on antiperovskite SEs is still in an early stage when compared to other SEs. From the effects of different synthesis precursors and routes on the final products to the antiperovskite SEs's behaviour at elevated temperatures, much remains to be studied. This thesis provides significant practical value to researchers attempting to optimise the synthesis of NaRAPs, make more informed decisions on the suitability of NaRAPs as SEs for SSMBs, and understand the origins of the non-Arrhenius ionic conductivity behaviour in NaRAPs and LiRAPs.

NaRAPs syntheses using commercial Na_2O are as common as those using 'homemade' pure Na_2O. However, there is no in-depth analysis of how the difference in precursor purity will affect the final products available in the literature. In Chapter 3, two batches of

Na_3OCl, Na_3OBr, and Na_3OBH_4, one with commercially available Na_2O and another one with 'homemade' pure Na_2O were synthesised. XRD detected minor crystalline NaCl and $NaBH_4$ impurities in 'commercial' Na_3OCl and Na_3OBH_4, respectively, but no crystalline impurity peaks in 'commercial' Na_3OBr and all 'homemade' compositions. ^{23}Na static NMR revealed that 'homemade' pure Na_2O precursor significantly reduces the amount of Na_2O poorly crystalline impurity in the final product and leads to a lower amount of crystalline impurity due to a more complete reaction. In terms of processing, cross-section SEM images show no indication of through pores in both cold pressed and hot pressed pellets. 3D sample reconstruction using PFIB-SEM will be required to confirm this. hot pressing leads to fewer pores, higher interparticle contact area, and better contact between the solid electrolyte and the blocking electrodes. As a result, an ≈ 1 order of magnitude increase in ionic conductivity was observed when the pellets were hot pressed instead of cold pressed. To our knowledge, there are no experimental reports on the electronic conductivity of NaRAPs. The electronic conductivity of all 'homemade' composition measurements using chronoamperometry with gold blocking electrodes on both sides of the pellets revealed that the electronic conductivities of the three compositions we synthesised were in the range of $10^{-10}\,\mathrm{S\,cm^{-1}}$, lower than those reported for NASICON. Using two ion-blocking electrodes is not the same as a real Wagner-Hebb measurement using a Na electrode and an ion-blocking electrode. Instead, it provides an upper limit of the electronic conductivity. Hence, it is possible for the values to be lower if the measurements were repeated using the Wagner-Hebb method. Finally, the in-situ XPS experiment with Na metal provided experimental evidence that Na_3OCl, Na_3OBr, and Na_3OBH_4 are stable against Na metal at room temperature, with Na_3OBH_4 being the most stable among the

three compositions. Further experiment using a combination of atomic force microscopy (AFM) and time-of-flight secondary ion mass spectroscopy (ToF-SIMS) is required to estimate the SEI thickness for each composition accurately. Finally, Na_3OBH_4's ionic conductivity is not that much higher than the other two compositions, but it is more stable against Na-metal and less electronically conductive than the other two, making it a more desirable SE.

In light of understanding more of the NaRAPs properties, it is clear that among the previously researched compositions, none of them has ionic conductivity that is comparable to that of NASICON and sodium beta alumina. This along with their poor stability in the air will be the main obstacle for their practical applications. Higher ionic conductivity could be achieved through a combination of computational and experimental efforts. Through their $Na_{3-x}O_{1-x}(NH_2)_x(BH_4)$, Tsai et al. have demonstrated that ion transport via double paddlewheel mechanism can lead to a Na-ion conductivity of up to 10^2 times higher at $x = 1$ than via a vacancy-mediated mechanism. Alternatively, if comparable ionic conductivity to NASICON and sodium beta alumina cannot be achieved, further research can be done on utilising NaRAPs as a protective layer for other SEs with higher ionic conductivity in SSMBs. Taking advantage of antiperovskites' great stability against metal anodes, this strategy could improve the cycling stability and prolong the cycle life of the SSMBs.

Non-Arrhenius ionic conductivity behaviour has been reported in Na_3OBr and other antiperovskite compositions. However, the origin of this behaviour is not yet well understood. The non-Arrhenius ionic conductivity behaviour of Na_3OBr synthesised with commercially available Na_2O does not originate from a melting or order-disorder transition.

The bulk characterisation of this material did not show a detectable change in its crystal structure. Further local characterisation using variable temperature in-situ NMR revealed that the sample contained a minor fraction of poorly crystalline impurities which form an eutectic mixture which melts at around $250\,^{\circ}\mathrm{C}$, promoting Na^{+} mobility. While the use of the same precursors and similar synthesis methods is common in prior literature, the likelihood that these lead to the formation of poorly crystalline impurity phases which affect the electrochemical performance of the material has not been understood until now. It is therefore advisable not to use commercial Na_2O, which contains $\approx 20\%$ Na_2O_2, as a solid-state synthesis precursor. Ball-milling may reduce the crystallinity of impurity phases, which could explain why they are often overlooked in solid-state electrolyte characterisation studies. Therefore, if a mechanochemical synthesis method is employed, it is important also to check for poorly crystalline impurities. These findings improve understanding of the processing-structure-properties relationships pertaining to NaRAPs and highlight the need to determine these relationships in other materials systems, which will accelerate the development of high-performance solid electrolytes.

In light of the findings above, we also investigate the non-Arrhenius ionic conductivity behaviour seen in $Li_2OHCl_{0.9}Br_{0.1}$. The results reveal that despite the initial similarities, the origins of this behaviour in Na_3OBr and $Li_2OHCl_{0.9}Br_{0.1}$ are different. Both bulk and local characterisations of this material showed a detectable change in its crystal structure. From Pawley and Rietveld refinements of the variable temperature Bragg data, discontinuity was observed in the lattice parameter, peak intensity ratios, and halide ions thermal parameter. The lattice parameter decreases above $240\,^{\circ}\mathrm{C}$ and the rate of increase of the halide ions thermal parameter increases above the same point. These findings show that

there is a bulk change in the crystal structure where the ions are getting closer to one another. Supporting these findings, the PDF data from the same beamline (DLS I15-1), showed significant changes in the O-B and B-B, where B is a halide ion, peaks. They merge above the temperature at which the first endothermic peak was observed in the DSC of $Li_2OHCl_{0.9}Br_{0.1}$, at around $240\,^{\circ}\mathrm{C}$. This means that the O^{2-}, Cl^{-}, and Br^{-} ions migrate from their original positions in the cubic structure and maintain this new structure until the structure finally melts. Further local characterisation using variable temperature in-situ NMR revealed that the chemical shifts jump and the peak width decreases significantly at around $230\,^{\circ}\mathrm{C}$. This peak width behaviour can be explained by the significant increase in Li^{+} mobility, which is in line with our finding from EIS, where we saw a step increase in ionic conductivity and a decrease in activation energy from 1.09 eV to 0.81 eV at a similar temperature. The significant change in chemical shifts could have happened because ^{7}Li is more shielded as they become closer to Cl^{-}, Br^{-}, or O^{2-}. This supports our earlier findings from the sequential Pawley refinements, where the lattice parameter of the $Li_2OHCl_{0.9}Br_{0.1}$ decreases above $240\,^{\circ}\mathrm{C}$. We propose that the anion disordering is the main factor responsible for the endothermic peak observed in the DSC at $240\,^{\circ}\mathrm{C}$ and subsequently the enhanced Li^{+} ionic mobility in $Li_2OHCl_{0.9}Br_{0.1}$ between this temperature and the melting point. These findings improve understanding of how $Li_2OHCl_{0.9}Br_{0.1}$'s structure changes with temperature and how this change affects its ionic conductivity. However, it is still not clear why the origins of the non-Arrhenius ionic conductivity behaviour in $Li_2OHCl_{0.9}Br_{0.1}$ and Na_3OBr are different, which can be due to the difference in vacancy contents and the fact that $Li_2OHCl_{0.9}Br_{0.1}$ has some degree of disordering to start with because of the anion mixing (Cl with Br). To confirm this, comparison studies

should be done on compositions with variable vacancy content and both mixed and single-halide anions. Furthermore, MD or RMC simulations are required to fit the experimental data with an appropriate model structure to visualise and elucidate the anion disordering mechanisms.

Overall, the insights provided by this thesis offer significant practical value to researchers attempting to optimise the synthesis of NaRAPs and make more informed decisions on the suitability of NaRAPS as SEs for SSMBs. While the materials studied are far from being suitable for practical applications, studying their processing-structure-properties relationships and the behaviours at elevated temperatures in depth has established a valuable understanding of the origins of their non-Arrhenius ionic conductivity behaviour. The techniques used in this thesis can be easily applied to re-investigate similar behaviour in other SE materials, particularly other antipeorvskite compositions including K-rich antiperovskites.